

THE *HUBBLE SPACE TELESCOPE*\* CLUSTER SUPERNOVA SURVEY:  
III. CORRELATED PROPERTIES OF TYPE IA SUPERNOVAE AND THEIR HOSTS AT  $0.9 < z < 1.46$

J. MEYERS<sup>1,2</sup>, G. ALDERING<sup>2</sup>, K. BARBARY<sup>1,2</sup>, L. F. BARRIENTOS<sup>3</sup>, M. BRODWIN<sup>4,21</sup>, K. S. DAWSON<sup>5</sup>, S. DEUSTUA<sup>6</sup>, M. DOI<sup>7</sup>,  
P. EISENHARDT<sup>8</sup>, L. FACCIOLI<sup>2</sup>, H. K. FAKHOURI<sup>1,2</sup>, A. S. FRUCHTER<sup>6</sup>, D. G. GILBANK<sup>9</sup>, M. D. GLADDERS<sup>10</sup>, G. GOLDBABER<sup>1,2,23</sup>,  
A. H. GONZALEZ<sup>11</sup>, T. HATTORI<sup>12</sup>, E. HSIAO<sup>2</sup>, Y. IHARA<sup>7,22</sup>, N. KASHIKAWA<sup>13</sup>, B. KOESTER<sup>10,14</sup>, K. KONISHI<sup>15</sup>, C. LIDMAN<sup>16</sup>,  
L. LUBIN<sup>17</sup>, T. MOROKUMA<sup>7,13,22</sup>, T. ODA<sup>18</sup>, S. PERLMUTTER<sup>1,2</sup>, M. POSTMAN<sup>6</sup>, P. RIPOCHE<sup>2</sup>, P. ROSATI<sup>19</sup>, D. RUBIN<sup>1,2</sup>, E. RYKOFF<sup>2</sup>,  
A. SPADAFORA<sup>2</sup>, S. A. STANFORD<sup>17,20</sup>, N. SUZUKI<sup>2</sup>, N. TAKANASHI<sup>13</sup>, K. TOKITA<sup>7</sup>, N. YASUDA<sup>15</sup>  
(THE SUPERNOVA COSMOLOGY PROJECT)

Draft version August 14, 2019

ABSTRACT

Using the sample of Type Ia supernovae (SNe Ia) discovered by the *Hubble Space Telescope* (*HST*) Cluster Supernova Survey and augmented with *HST*-observed SNe Ia in the GOODS fields, we search for correlations between the properties of SNe and their host galaxies at high redshift. We use galaxy color and quantitative morphology to determine the red sequence in 25 clusters and develop a model to distinguish passively evolving early-type galaxies from star-forming galaxies in both clusters and the field. With this approach, we identify six SN Ia hosts that are early-type cluster members and eleven SN Ia hosts that are early-type field galaxies. We confirm for the first time at  $z > 0.9$  that SNe Ia hosted by early-type galaxies brighten and fade more quickly than SNe Ia hosted by late-type galaxies. We also show that the two samples of hosts produce SNe Ia with similar color distributions. The relatively simple spectral energy distributions (SEDs) expected for passive galaxies enable us to measure stellar masses of early-type SN hosts. In combination with stellar mass estimates of late-type GOODS SN hosts from Thomson & Chary (2011), we investigate the correlation of host mass with Hubble residual observed at lower redshifts. Although the sample is small and the uncertainties are large, a hint of this relation is found at  $z > 0.9$ . By simultaneously fitting the average cluster galaxy formation history and dust content to the red-sequence scatters, we show that the reddening of early-type cluster SN hosts is likely  $E(B - V) \lesssim 0.06$ . The similarity of the field and cluster early-type host samples suggests that field early-type galaxies that lie on the red sequence may also be minimally affected by dust. Hence, the early-type hosted SNe Ia studied here occupy a more favorable environment to use as well-characterized high-redshift standard candles than other SNe Ia.

*Subject headings:* Cosmology:General, Supernovae:General, Galaxies:Clusters

jmeyers314@berkeley.edu

\* Based on observations made with the NASA/ESA Hubble Space Telescope and obtained from the data archive at the Space Telescope Institute. STScI is operated by the Association of Universities for Research in Astronomy, Inc. under the NASA contract NAS 5-26555. The observations are associated with program 10496.

<sup>1</sup> Department of Physics, University of California Berkeley, Berkeley, CA 94720, USA

<sup>2</sup> E.O. Lawrence Berkeley National Lab, 1 Cyclotron Rd., Berkeley CA, 94720, USA

<sup>3</sup> Departamento de Astronomía, Pontificia Universidad Católica de Chile, Santiago, Chile

<sup>4</sup> Harvard-Smithsonian Center for Astrophysics, 60 Garden Street, Cambridge, MA 02138, USA

<sup>5</sup> Department of Physics and Astronomy, University of Utah, Salt Lake City, UT 84112, USA

<sup>6</sup> Space Telescope Science Institute, 3700 San Martin Drive, Baltimore, MD 21218, USA

<sup>7</sup> Institute of Astronomy, Graduate School of Science, University of Tokyo 2-21-1 Osawa, Mitaka, Tokyo 181-0015, Japan

<sup>8</sup> Jet Propulsion Laboratory, California Institute of Technology, Pasadena, CA 91109, USA

<sup>9</sup> Department of Physics and Astronomy, University Of Waterloo, Waterloo, Ontario, N2L 3G1 Canada

<sup>10</sup> Department of Astronomy and Astrophysics, University of Chicago, Chicago, IL 60637, USA

<sup>11</sup> Department of Astronomy, University of Florida, Gainesville, FL 32611, USA

<sup>12</sup> Subaru Telescope, National Astronomical Observatory of Japan, 650 North Aohaku Place, Hilo, HI 96720, USA

<sup>13</sup> National Astronomical Observatory of Japan, 2-21-1 Osawa, Mitaka, Tokyo, 181-8588, Japan

<sup>14</sup> Kavli Institute for Cosmological Physics, The University of Chicago,

Chicago, IL 60637, USA

<sup>15</sup> Institute for Cosmic Ray Research, University of Tokyo, 5-1-5, Kashiwanoha, Kashiwa, Chiba, 277-8582, Japan

<sup>16</sup> Australian Astronomical Observatory, PO Box 296, Epping, NSW 1710, Australia

<sup>17</sup> University of California, Davis, CA 95618, USA

<sup>18</sup> Department of Astronomy, Kyoto University, Sakyo-ku, Kyoto 606-8502, Japan

<sup>19</sup> ESO, Karl-Schwarzschild-Strasse 2, D-85748 Garching, Germany

<sup>20</sup> Institute of Geophysics and Planetary Physics, Lawrence Livermore National Laboratory, Livermore, CA 94550, USA

<sup>21</sup> W. M. Keck Postdoctoral Fellow at the Harvard-Smithsonian Center for Astrophysics

<sup>22</sup> JSPS Fellow

<sup>23</sup> Deceased

## 1. INTRODUCTION

The use of Type Ia supernovae (SNe Ia) as standard candles in estimating astronomical distances has proven indispensable for modern cosmology, leading to the remarkable discovery that the expansion of the Universe is accelerating (Riess et al. 1998; Perlmutter et al. 1999). Together with measurements of the cosmic microwave background (Dunkley et al. 2009; Komatsu et al. 2011) and baryon acoustic oscillations (Eisenstein et al. 2005; Percival et al. 2010), our recent compilation of the myriad SN surveys that led to and followed the initial discovery has now constrained the dark energy equation of state to be  $w = -0.974_{-0.058}^{+0.054}(\text{stat})_{-0.080}^{+0.075}(\text{stat}+\text{sys})$  (Amanullah et al. 2010). The constraints from the 557 SNe Ia in this compilation are now limited by systematic uncertainties. Additional SN Ia observations will not greatly improve dark energy constraints until the systematic errors are reduced.

Improvements in SN Ia distance estimates have historically followed two paths. The first path is to identify subsets of SNe with smaller intrinsic brightness dispersion (e.g. the Type Ia subset or “Branch-normal” SNe Ia). The second path is to make corrections exploiting empirical correlations between SN brightness and other observables (e.g. light curve shape and color). The properties of SN Ia host galaxies offer additional variables with which to search for smaller dispersion subsets or correlated observables. In fact, such a correlation has recently been reported: SNe Ia in more massive hosts are brighter after light curve shape and color corrections (Kelly et al. 2010; Sullivan et al. 2010; Lampeitl et al. 2010).

The brightnesses of SNe Ia are correlated with their colors at maximum light: bluer SNe Ia are brighter. This trend is broadly consistent with extinction due to dust as commonly described by  $R_B = A(B)/E(B - V)$  (Cardelli et al. 1989). When relating SN Ia colors to peak magnitudes, the parameter  $\beta = \Delta M_B / \Delta c$  is used, where  $c = (B - V)_{max} - \langle B - V \rangle_{max}$ ; e.g.  $c$  is the excess color at maximum brightness with respect to the average. Direct fits of SN Ia observations have found that  $\beta$  is considerably smaller than the value of  $R_B$  observed in the Milky Way diffuse interstellar medium, suggesting that an intrinsic component to the bluer–brighter relation is also important (Tripp 1998; Astier et al. 2006; Conley et al. 2007; Nobili & Goobar 2008). The systematic errors associated with the interpretation of  $\beta$ , i.e., what fraction is attributable to dust and how might that evolve with redshift, are now comparable to the statistical errors of SN Ia surveys (Kowalski et al. 2008; Wood-Vasey et al. 2007). However, if one were to identify SN Ia hosts with small extinction, then a single component of the SN Ia color-magnitude relation, the intrinsic component, could be isolated.

In this paper we analyze the host galaxies of  $z > 0.9$  SNe Ia drawn from the *HST* Cluster SN Survey (Dawson et al. 2009, PI-Perlmutter: GO-10496) and surveys of the GOODS fields (Blakeslee et al. 2003b; Riess et al. 2004, 2007). We investigate how host properties correlate with SN Ia properties and identify hosts minimally affected by dust. Particularly interesting host properties such as age and metallicity are usually difficult to obtain, but are correlated with the position of a galaxy on its cluster’s red sequence (Gallazzi et al. 2006). The environment of the *HST* Cluster SN Survey thus lends itself to a particular analysis strategy: how does the location of a host galaxy on its cluster’s red sequence correlate with its SN, what does it imply about the SN type, and how does it begin to parse the origin of the SN reddening law?

This paper is organized as follows: In §2 we describe

progress to date of SN host galaxy studies at lower redshifts. In §3 we describe the *HST* Cluster SN Survey and the *HST* SN surveys of the GOODS fields, the data taken, and the various photometric, morphological, and spectroscopic quantities that we derive from them. In §4 we describe how, by using the color-magnitude locations of spectroscopically confirmed red-sequence cluster members, we predict the location of the red sequence for each cluster, including those without extensive spectroscopic coverage. Additionally, we demonstrate how quantitative morphology parameters can be used to enhance the contrast of the red sequence to more easily fit a color-magnitude relation (CMR) for each cluster. In §5 we describe criteria to classify the observed SN hosts, and in §6 we use expected rates of SNe Ia and core collapse SNe (SNe CC) in their individual galaxies to help type the SNe. In §7 we investigate limits on extinction for SNe hosted by early-type galaxies. In §8 we investigate correlations between SN properties and properties of their host galaxies. Finally, in §9 we summarize our conclusions and discuss their implications.

This paper is one of a series of ten papers that report supernova results from the *HST* Cluster Supernova Survey (PI: Perlmutter, GO-10496), a survey to discover and follow SNe Ia of very distant clusters. Paper I (Dawson et al. 2009) describes the survey strategy and discoveries. Paper II (Barbary et al. 2010) reports on the SN Ia rate in clusters. The current work, Paper III, addresses the properties of the galaxies that host SNe Ia. Paper IV Ripoche et al. (2011) introduces a new technique to calibrate the “zeropoint” of the NICMOS camera at low count rates, which is critical for placing NICMOS-observed SNe Ia on the Hubble diagram. Paper V (Suzuki et al. 2011) reports the SN Ia light curves and cosmology from the *HST* Cluster SN Survey. Paper VI (Barbary et al. 2011) reports on the volumetric field SN Ia rate. Melbourne et al. (2007), one of several unnumbered papers in this series, present a Keck Adaptive Optics observation of a  $z = 1.31$  SN Ia in *H*-band. Barbary et al. (2009) report the discovery of the extraordinary luminous supernova, SN SCP06F6. Morokuma et al. (2010) present the spectroscopic follow-up observations for SN candidates. Hsiao et al. (2011) develop techniques to remove problematic artifacts remaining after the standard STScI pipeline. A separate series of papers, ten to date, reports on cluster studies from the *HST* Cluster SN Survey: Brodwin et al. (2011); Eisenhardt et al. (2008); Jee et al. (2009); Hilton et al. (2007, 2009); Huang et al. (2009); Santos et al. (2009); Strazzullo et al. (2010); Rosati et al. (2009); and Jee et al. (2011).

## 2. SN IA HOSTS

In this section we briefly discuss the relationships between SNe and their host galaxies with particular emphasis on early-type host galaxies of SNe Ia. We also introduce the *HST* Cluster SN Survey, which targets massive galaxy clusters to increase the yield of SN Ia discoveries, particularly those in low-dust early-type hosts.

### 2.1. SN typing by host

Early-type galaxies have almost never been observed to host Type Ib/c or Type II SNe (hereafter SNe CC), which are generally thought to originate from the collapse of the cores of massive (and hence young) stars. In an extensive literature search of hundreds of SNe CC, Hakobyan et al. (2008) uncovered 22 examples reported as being hosted by early-type galaxies, but ultimately reclassified 19 of these galax-

ies as late-type. The SN associated with one of the remaining three galaxies has since been reclassified as a cataclysmic variable star within the Milky Way (Leonard 2010). The SNe hosted by the remaining two early-type hosts, SN2000ds and SN2005cz, are both members of the SN2005E-like subset of faint “Ca-rich” SNe Ib. The origins of SNe in this subset are still under debate, though it is clear that they are readily distinguishable from SNe Ia by their faint peak magnitudes ( $M_B \sim -15$  compared to  $M_B \sim -18$  for even a very faint SN Ia) (Perets et al. 2010; Kawabata et al. 2010). In a separate analysis of the near ultraviolet and optical colors of early-type SN hosts (including two which were reclassified by Hakobyan et al.), Suh et al. (2011) find that the early-type hosts of SNe CC have had more recent star formation and occupy a different part of the UV-optical color-magnitude diagram than identically selected early-type hosts of SNe Ia.

Despite these rare possible exceptions, SNe hosted by early-type galaxies are overwhelmingly Type Ia. Typing high-redshift ( $z > 0.9$ ) SNe spectroscopically can be done from space with *HST* (Riess et al. 2004) but requires a significant investment of orbits (4-8 per SN at  $z \sim 1.2$ ). Not only are SNe increasingly faint at higher redshift, but the rest-frame features used to identify a Type Ia become shifted out of the optical wavelengths. Ground-based spectroscopy faces the additional difficulty that the night sky becomes increasingly bright at redder wavelengths. With ideal conditions and by targeting the SN near the peak of its light curve, Morokuma et al. (2010) have shown it is possible to spectroscopically type SNe Ia as high as  $z = 1.34$  from the ground, but this is by no means typical. In fact, many of the lower redshift targets in this paper (of which many also had higher signal-to-noise ratio spectra) yielded inconclusive types. Classifying SNe in elliptical galaxies as Type Ia can therefore provide an efficient and robust alternative to potentially expensive spectroscopic typing at high redshift.

## 2.2. Dust in early-type SN Ia hosts

Early-type SN Ia hosts offer an additional advantage to typing: they generally contain only small amounts of dust. Although *HST* images of the cores of nearby early-type galaxies indicate that  $\sim 50\%$  exhibit optical absorption due to dust in small disks or filaments, these are usually confined to the central few hundred parsecs (van Dokkum & Franx 1995; Tomita et al. 2000; Rest et al. 2001; Tran et al. 2001; Lauer et al. 2005; Ferrarese et al. 2006). In contrast, SNe Ia hosted by early-type galaxies are spatially distributed following the optical light of their host galaxies (Förster & Schawinski 2008). Observations of emission from dust at far-infrared (FIR) wavelengths suggest that additional dust is diffusely distributed throughout at least some nearby early-type galaxies (Goudfrooij & de Jong 1995; Temi et al. 2004, 2007). The inferred dust mass relative to the stellar mass of these galaxies varies greatly; at fixed optical luminosity, Temi et al. (2007) measure FIR luminosities that span two orders of magnitude. At the low dust-mass end, at least several early-type galaxies (3 elliptical and 3 S0) with  $M_B \sim -18$  to  $-20$ , are undetected in the Herschel Space Observatory survey of the Virgo cluster. Upper limits constrain the associate dust mass of these galaxies to be  $< 10^4 M_\odot$  (Clemens et al. 2010). For comparison, the Virgo cluster spiral galaxies in the same  $B$ -band luminosity range also observed by Herschel have dust masses of  $\sim 10^7 - 10^8 M_\odot$  (Davies et al. 2011). Early-type galaxy dust masses derived from Spitzer tend to fall in the range  $10^4 - 10^6$  (Kaneda et al. 2007). To estimate the extinction associated with a certain

mass of dust, we use  $\langle A_V \rangle = M_d \Gamma / \Sigma$ , with  $\Sigma$  the area of the dust feature,  $\langle A_V \rangle$  the average  $V$ -band absorption in that area, and  $\Gamma \sim 6 \times 10^{-6} \text{ mag kpc}^2 M_\odot^{-1}$  the visual mass absorption coefficient (van Dokkum & Franx 1995). For dust uniformly distributed throughout a disc with radius 3 kpc, which is representative of the half-light radii of the galaxies considered in this paper, the absorption ranges from  $A_V < 0.002$  to  $\sim 0.2$ . Since dust is not actually distributed in a uniform foreground screen, but rather is embedded within the galaxy, these values only provide a rough guide to the expected extinction along the lines of sight toward early-type hosted SNe Ia.

At high redshift, FIR observations of SN Ia hosts are impractical. However, optical observations of the integrated colors of galaxies can also place constraints on the extinction expected from diffuse dust. For example, consider the case where galaxy colors are the combined result of stellar population age, metallicity, and dust. The contributions of age and metallicity to the integrated color can be removed by using an auxiliary correlated variable. At low redshift, the spectral absorption feature  $Mg_2$  is such a variable. The equivalent width of  $Mg_2$  is expected to correlate with the rest-frame intrinsic (i.e. unextinguished)  $B - V$  color of elliptical galaxies (Faber et al. 1989). The line strength increases with increasing galaxy age and metallicity, and consequently color, but because the wavelength interval of the line is relatively narrow it should not correlate significantly with dust. Schlegel et al. (1998) measured the scatter about the  $Mg_2$ -color relation for nearby elliptical galaxies to be just  $\sigma_{BV} = 0.0257 \text{ mag}$ . If at least some elliptical galaxies are effectively dust-free ( $A_V < 0.01$ ), which seems likely given the range of dust masses discussed above, then this scatter measurement implies an absolute limit on dust reddening at the  $E(B - V) \sim 0.03$  level. While spectroscopy of the  $Mg_2$  feature may not be feasible at high redshift, the red sequence may provide a readily available alternative calibrator.

Two mechanisms have been proposed to explain the origin of the dust found in elliptical galaxies. Elliptical galaxies may accrete dust and gas during (minor) mergers with dusty late-type galaxies. This scenario is supported by observations that the motions of dust and gas in some nearby early-type galaxies seem unrelated to the motions of their stars (Goudfrooij et al. 1994; van Dokkum & Franx 1995; Caon et al. 2000). As part of the Galaxy-Zoo project, Kaviraj et al. (2011) find that early-type galaxies with prominent dust lanes are likely associated with mergers due to the frequency with which they present disturbed morphologies compared to a control sample without dust lanes. Prominent dust lane early-type galaxies are relatively rare, however, constituting just 4% of the early-type Galaxy-Zoo sample, and are even rarer in cluster environments..

Noting that the dynamical freefall time for a merging galaxy (several  $\sim 10^8 \text{ yr}$ ) is comparable to the sputtering lifetime of dust grains in the hot interstellar medium of early-type galaxies ( $\sim 10^7 - 10^8 \text{ yr}$ ), Temi et al. (2007) argue that dust originating from mergers must be resupplied at least every  $\sim 10^8 \text{ yr}$ . Such a high rate of early-type – late-type mergers is not observed, however. As an alternative, they propose an internal origin for diffuse dust in early-type galaxies: dust is generated in the atmospheres of evolved red giant stars (Knapp et al. 1989; Athey et al. 2002) and may accumulate in the concentrated disks of dust commonly observed in the centers of early-type galaxies (Mathews & Brighenti 2003). Intermittent AGN activity can then buoyantly transport this dust out

to large radii where it will be destroyed by sputtering in the hot interstellar medium.

One possible caveat to the expectation of low extinction SNe Ia in early-type galaxies is small amounts of recent star-formation seen in some early-type galaxies, especially lenticular galaxies, and associated dust (Yi et al. 2005; Donati et al. 2007; Schawinski et al. 2007; Kaviraj et al. 2007, 2008; Temi et al. 2009a,b). Together with the expected increase in the SN Ia rate with star-formation rate (see §2.3 below), it is possible that an SN Ia in a mostly dust-free galaxy could, nevertheless, suffer from extinction. Fortunately, recent star-formation in early-type galaxies is usually confined to their inner regions (Kuntschner et al. 2006; Sarzi et al. 2006), whereas, as mentioned above, the spatial distribution of SNe Ia follows the optical light distribution. Furthermore, we have directly constrained star-formation using spectroscopy of our host galaxies and its possible effect in increasing the galactic SN Ia rate (see §6). We expect that most of our early-type hosted SNe Ia are not associated with recent star-formation.

### 2.3. SN Ia properties by host

Several lines of evidence suggest that the demographics of SNe Ia hosted by early-type galaxies are different than those of SNe Ia hosted by late-type galaxies. Using infrared magnitudes of low-redshift SN Ia host galaxies in the 2MASS survey, Mannucci et al. (2005) measured the SN Ia rate per unit stellar mass for different host types. They found a rate  $\sim 20$  times larger in late-type galaxies than in E/S0 galaxies. Splitting the galaxies by color (as a proxy for star formation) they found a rate  $\sim 30$  times larger in blue galaxies than in red galaxies. Sullivan et al. (2006) fit SED models to five-band galaxy photometry to directly constrain the star formation rate and mass of intermediate redshift SN Ia host galaxies in the Supernova Legacy Survey (SNLS). This analysis showed that the SN Ia rate is  $\sim 10$  times larger per unit stellar mass in actively star-forming galaxies than in passive galaxies. For a given episode of star formation, the SN Ia rate quickly peaks and declines as the progenitor population ages.

Perhaps not surprisingly, the properties of SNe themselves are also correlated with the properties of their hosts. At low redshift, SNe Ia hosted by late-type, spiral galaxies tend to have broader (slower) light curves on average (Hamuy et al. 1996; Gallagher et al. 2005), although interestingly, Hicken et al. (2009) find that the broadest SN light curves are found in SNe hosted by Sb-Sc galaxies and not younger Sd-Irr galaxies. Sullivan et al. (2006) showed that this distinction extends to intermediate redshift hosts with actively star-forming galaxies (generally late-type) hosting SNe Ia with broader light curves. Several analyses suggest that SNe Ia hosted by early-type galaxies may have a smaller intrinsic peak brightness dispersion after light curve and color corrections are applied (Sullivan et al. 2003; Jha et al. 2007; Sullivan et al. 2010; Lampeitl et al. 2010), though at least one analysis finds the opposite result (Hicken et al. 2009).

Since SN Ia properties are correlated with the properties of their host galaxies, and the demographics of galaxies change with redshift, the demographics of SNe Ia will also change with redshift. This shift can bias inferred cosmological parameters if not handled carefully. Tests for bias in cosmology constructed by segregating SNe Ia by host-type were discussed in Perlmutter et al. (1997) and carried out with a small sample of SNe Ia (17) in Perlmutter et al. (1999), and a larger sample (39) in Sullivan et al. (2003) without any differences in

fitted cosmological parameters apparent within the statistical uncertainties. However, with a much larger sample from the SNLS (Sullivan et al. 2010), it becomes possible to see subtle differences in  $\beta$  dependent on the host. SNe Ia hosted by lower specific star-formation rate galaxies obey a shallower relation than SNe Ia hosted by higher specific star-formation rate galaxies ( $\beta \sim 2.8$  compared to  $\beta \sim 3.5$ ; the exact value depends on the choice of specific star-formation rate delineating the low and high star-forming samples). Similarly, using SNe drawn from the Sloan Digital Sky Survey (SDSS), Lampeitl et al. (2010) find  $\beta \sim 2.5$  for passive hosts and  $\beta \sim 3$  for star-forming hosts. Since  $\beta$  reflects the combined effect of host galaxy dust extinction and an intrinsic SN color-luminosity relation, it is not surprising that  $\beta$  should be closer to the Milky Way dust total-to-selective extinction coefficient of  $R_B = 4.1$  in dusty star-forming galaxies than in passive galaxies. This result also suggests that as the fraction of low star-forming early-type galaxies decreases with redshift and the fraction of high star-forming galaxies increases, the average value of the relation  $\langle \beta(z) \rangle$  will increase and introduce a bias on measurements of  $w$  if the subpopulations are not treated separately.

Perhaps a more important consideration, however, is the recently reported evidence for a correlation between host galaxy mass and Hubble residual after applying corrections for light curve shape and color. By fitting SEDs derived from the PEGASE2 (Fioc & Rocca-Volmerange 1997, 1999) stellar population synthesis models to SDSS photometry of host galaxies, Kelly et al. (2010) measured the host masses of the low- $z$  SNe in the Hicken et al. (2009) analysis and compared these to their Hubble residuals obtained with a variety of light curve fitters. They found that SNe Ia in more massive galaxies are brighter (after stretch and color corrections) by about  $\sim 0.1$  mag. Sullivan et al. (2010) found a similar relation in SNLS SNe and host galaxy photometry using PEGASE2 SEDs and the SiFTO light curve fitter (Conley et al. 2008). Finally, Lampeitl et al. (2010) found a similar relationship in the SDSS-II SN survey by segregating SNe by host type, with passive galaxies hosting brighter post-correction SNe. However, because the passive galaxies in this dataset are on average more massive than the star-forming galaxies, this relation can also be framed in terms of host galaxy mass. These results are particularly important for targeted surveys, such as those that target massive galaxies at low redshift or the HST Cluster SN Survey which targets clusters of massive galaxies at high redshift. The demographics of hosts from these surveys are substantially different than for untargeted surveys. The SNe they discover should be on average brighter (after color and light curve shape corrections) than those in other surveys, a property which needs to be corrected for in cosmological analyses.

### 2.4. The HST Cluster SN Survey

By targeting massive galaxy clusters, the *HST* Cluster SN Survey was designed to efficiently discover well-characterized SNe Ia at high redshift. Clusters are rich in elliptical galaxies, which constitute a linear red sequence in a color-magnitude diagram. The observed evolution of the red-sequence slope indicates that ellipticals in the cores of clusters have passively evolved since forming at high-redshift ( $z > 2$ ) and that the redder colors of more massive galaxies is due to increased metallicity (Kodama 1997; Kodama & Arimoto 1997; Kauffmann & Charlot 1998; Gladders et al. 1998). With filters straddling the 4000Å break, the red sequence can

be readily isolated from foreground and background galaxies, a technique also used to find clusters (e.g. Gladders & Yee 2000).

Clusters also provide a convenient mechanism for probing the dust contents of cluster early-type galaxies. Just as the  $Mg_2$  absorption feature traces age and metallicity at low redshift, the magnitude axis of the red sequence traces metallicity at high redshift. A dispersion in the residuals from the color-magnitude relation of roughly 3% is found in clusters ranging from Coma to high redshift ( $z \sim 1.5$ ) (Bower et al. 1992; Ellis et al. 1997; Stanford et al. 1998; Blakeslee et al. 2003a; Mei et al. 2006b,a; Lidman et al. 2008; Mei et al. 2009). Some of this dispersion can be attributed to differences in galaxy ages, and what remains sets a limit on dust. Finally, we also note that the uniform old stellar populations of elliptical galaxies imply simpler SEDs and hence better mass estimates with which to address the trends of §2.3.

The completed *HST* Cluster SN Survey produced 19  $z > 0.9$  SNe, eight of which were found in the clusters themselves. Deep two-color images of the cluster galaxies (including SN hosts) were also produced by stacking together SN search and follow-up epochs. Similar data exist from the SN surveys of the GOODS fields, which have discovered 26  $z > 0.9$  SNe Ia, all in the field. We analyze the host galaxies of these two sets of SNe in this paper.

### 3. DATA

To identify a set of SNe Ia hosted by a uniform stellar population and minimally affected by dust, we compare the photometry of SN host galaxies to the photometry of red-sequence galaxies and look for star-formation indicators in SN host spectroscopy. Identifying the red sequence requires careful measurement of galaxy magnitudes and colors, which we describe in this section. We also measure quantitative morphology parameters which we use to enhance the contrast of the red sequence in color-magnitude diagrams by exploiting the early-type galaxy population dominance along the red sequence.

#### 3.1. Image reduction and photometry

Twenty-five massive high-redshift ( $0.9 < z < 1.46$ ) galaxy clusters selected from X-ray, optical, and IR surveys were chosen for the *HST* Cluster SN Survey (Dawson et al. 2009). Clusters were each visited by *HST* four to nine times between July 2005 and December 2006. Each visit typically consisted of four  $\sim 500$  second exposures in the F850LP filter (hereafter  $z_{850}$ ) of the Advanced Camera for Surveys (ACS) wide field camera (WFC) and one  $\sim 500$  second exposure in the F775W filter (hereafter  $i_{775}$ ) of the ACS WFC. The  $i_{775}$  filter roughly matches rest-frame  $U$ -band for clusters with  $0.9 < z < 1.25$ , with the best match occurring at  $z = 1.1$ . The  $z_{850}$  filter roughly matches the rest-frame  $B$ -band in this redshift range with its closest match occurring at  $z = 1.05$ . For more distant clusters with  $1.25 < z < 1.46$ , the  $z_{850}$  filter more closely matches rest-frame  $U$ -band, with the best overlap at  $z = 1.45$ . In this paper we look principally at the deep coadditions of exposures from all observation epochs. Due to gyroscopic constraints, *HST* visits to individual clusters necessarily occurred at different position angles, resulting in coadditions in which pixels near the edges have smaller effective exposure time than pixels near the center (Figure 1). Each exposure specifically targeted the cluster core, so total integration time is nearly constant in the central

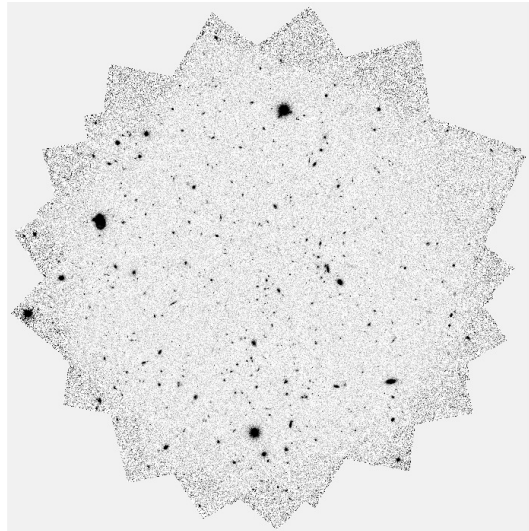


FIG. 1.— Final  $z_{850}$  mosaic for cluster ICS J1432.4+3332. The differences in background noise as a function of position are apparent towards the edges of the mosaic.

region of each coaddition. Four clusters, RDCS J0910+54 (Mei et al. 2006a), RDCS J0848+44 (Postman et al. 2005), RDCS J1252-29 (Blakeslee et al. 2003a) and XMMU 2235.3-2557 (Jee et al. 2009), had been previously targeted by ACS in  $i_{775}$  and  $z_{850}$  (PID9290 and PID9919), and we have included these additional exposures in our coadded images. Cluster CL 1604+4304 (Postman et al. 2005) had also been observed with ACS, but not in  $i_{775}$  and  $z_{850}$ . The individually sky subtracted exposures were stacked using MULTIDRIZZLE (Fruchter & Hook 2002; Koekemoer et al. 2002) with a square kernel,  $\text{pixfrac} = 0.8$  and the native output pixel scale of  $0.05''$ .

We similarly processed images obtained by *HST* ACS as part of the *HST* Great Observatories Origins Deep Survey (GOODS) Treasury program (Giavalisco et al. 2004). The *HST* GOODS program targeted two high galactic latitude fields to obtain deep multiband images for studies of galaxy evolution and included a ‘‘piggy-back’’ SN program to follow suspected  $z > 1$  SNe with ACS and the Near Infrared Camera and Multi-object Spectrograph (NICMOS). The original search consisted of five epochs over 15 ACS pointings for each of the two GOODS fields. A subsequent extension contributed an additional 14 epochs. The survey used nearly identical exposures in  $i_{775}$  and  $z_{850}$  for SN discovery and follow-up as our program. The initial GOODS SN survey yielded 11  $z > 0.9$  SNe Ia and its extension yielded an additional 13  $z > 0.9$  SNe Ia (Riess et al. 2004, 2007). We also add the host of one  $z > 0.9$  SN Ia discovered in a previous search of these fields – SN2002dd (Blakeslee et al. 2003b). One other  $z > 0.9$  SN has been discovered in these fields – SN1997ff, but its most likely redshift,  $z = 1.76$  is tentative and far beyond that of the clusters studied here. Lacking a comparison cluster red-sequence we do not analyze this SN host.

Galaxies that hosted SNe required special attention to prevent the SN light from biasing photometric and morphological statistics of the galaxies themselves. For each SN we created postage stamp images of each epoch in both bands. From these images, we subtracted a PSF model (described below) scaled to the flux of the light curve fit (details in Suzuki et al. (2011)) of the SN in each epoch. The postage stamp

images are then stacked and processed in the same manner as the full mosaics. When the final catalogs are created, the values derived from the SN-subtracted postage stamp images of SN hosts are substituted for the values derived from the full mosaics. To test the accuracy of the PSF subtractions, we also generated postage-stamp images of SN hosts by stacking only the subset of epochs in which the SN was far from its peak. Except for a few cases in which only one or two such epochs were available, we obtained consistent photometric and morphological results to those obtained from the PSF-subtracted images.

### 3.1.1. Object detection

To form initial object catalogs we used SExtractor version 2.8.6 (Bertin & Arnouts 1996) in dual image mode, relying on the  $z_{850}$  images for object detection. Determining appropriate parameters for the extraction proved challenging due to galaxy crowding near cluster cores. One needs to simultaneously be able to deblend neighboring galaxies while avoiding the dissection of single complexly structured galaxies into multiple catalog entries. We found that the two-pass Cold/Hot method (Rix et al. 2004) produced the best catalogs, particularly near cluster cores. This method works by aggressively deblending relatively bright objects (such as cluster core galaxies) in an initial pass of SExtractor, and subsequently filling in the object catalog with fainter objects in a second pass with the deblending parameters set less aggressively. The specific parameters for the two steps were optimized by trial and error judged by the successful identification and segmentation of galaxies near cluster cores.

### 3.1.2. PSF construction

In order to accurately measure the colors of galaxies we require PSF estimates for both the  $i_{775}$  and  $z_{850}$  bands. To identify stars in each field with which to construct a PSF we used the SExtractor FLUX\_RADIUS statistic. Objects with FLUX\_RADIUS in the range [1.4, 1.72] pixels are likely to be stars. For fields with many stars, we selected all stars within  $1.3'$  of the cluster center and  $z_{850}$  MAG\_AUTO between 18 and 24. For more sparsely populated fields, we selected the 10 stars closest to the cluster center falling in the same magnitude range. For each band of each field, an initial PSF was constructed by subtracting a local background (described below) from each star, oversampling each pixel  $9 \times 9$  times with the IDL procedure CONGRID, renormalizing each oversampled image by the flux near the stellar core, aligning the oversampled images to the nearest subpixel and taking the subpixel by subpixel median image. This PSF model was then refined by iteratively fitting it to the original stars and adding the oversampled median residual back into the model. The final PSF was trimmed to  $31 \times 31$  pixels, which contains more than 92% of the encircled energy in both  $i_{775}$  and  $z_{850}$  bands (Sirianni et al. 2005).

For more shallowly exposed fields, the wings of the PSF derived this way are relatively noisy and tend to be biased high when compared with PSFs from more deeply exposed fields. To reduce this bias, we match the radial profile of each PSF to the radial profile of the PSF derived from a reference field, that of cluster RDCS J1252.9-2927, which was both exposed more deeply than other fields and contained many stars. To measure the radial profiles of each PSF, we fit a 1D B-spline to the subpixel values as a function of radius. We then scale the PSF subpixel values by the ratio of the target field B-spline

and the reference field B-spline. This procedure produces PSF grids that are consistent with the encircled energy functions of Sirianni et al. (2005) to  $\sim 1\%$ . They also individually retain the correct azimuthal structure for coadditions of exposures which occurred at many different position angles. Finally, we note that while a more precise PSF model would vary across the field of each exposure, ours is sufficient for correcting the effects of differential blurring between the  $i_{775}$  and  $z_{850}$  filters when computing a galaxy color.

### 3.1.3. Galaxy magnitudes and colors

Nonstellar objects with  $19 < z_{850} < 26$  (measured with MAG\_AUTO) and  $-1 < i_{775} - z_{850} < 2$  (measured with MAG\_APER with a 10 pixel radius), were then selected as galaxies of interest for further processing. For each of these galaxies, postage stamp images were cut out of the main  $z_{850}$  mosaic for processing with GALFIT version 3.0 (Peng et al. 2010). We used GALFIT to obtain two key statistics: the  $z_{850}$  magnitude, and the half-light radius  $R_e$ . We also used GALFIT to produce an interloper-subtracted image used later when measuring quantitative morphology parameters.

Initial parameters for GALFIT were chosen using a variant of the GALAPAGOS algorithm (Häussler et al. 2007). Galaxies were modeled as Sérsic (1968) profiles with their Sérsic indices constrained between one and four. Interloper galaxies near each target galaxy were either masked out or simultaneously fit depending on the degree of overlap. For each galaxy, an adaptively sized elliptical annulus (typically with  $6''$  semi-major axis and  $\sim 3''$  width) with all galaxies and stars aggressively masked out was used to find the local sky background level, which was held fixed during the fit. We provided GALFIT with our estimated  $z_{850}$  PSF to internally convolve with its model before fitting to the actual image. The Sérsic profile magnitudes (and magnitude uncertainties) from the GALFIT fits, corrected for Milky Way extinction with the dust maps of (Schlegel et al. 1998), are the  $z_{850}$  magnitudes and uncertainties reported throughout the rest of this paper.

Measurements of galaxy color are complicated by the fact that the  $z_{850}$  PSF is  $\sim 10\%$  broader than the  $i_{775}$  PSF. To account for this difference we implemented a PSF matching scheme where, when measuring color, the  $z_{850}$  image is convolved with the  $i_{775}$  PSF and vice-versa. To fairly treat any color gradients in galaxies of different angular sizes, we measure color within a circular aperture with radius equal to the *apparent* (as opposed to *intrinsic*) half-light radius  $R_e$  of the cross-convolved  $z_{850}$  image. Measuring this radius requires us to run GALFIT a second time on each galaxy, this time using the cross-convolved  $z_{850}$  image and *not* providing a PSF for GALFIT to internally convolve with its model. A minimum color aperture radius of 3 pixels, corresponding to 1.2 kpc at  $z \sim 1$ , was enforced.

We modeled the errors for each band's flux as the sum in quadrature of the Poisson error from the object flux and the error in the background (e.g. sky, CCD readout noise). Because some of the clusters are not evenly exposed over the analysis region, we estimated the background contribution to the error for each galaxy using  $\sigma_{\text{bkg}}$ , the local pixel-by-pixel standard deviation within the same elliptical annulus previously defined in order to measure the local background level. If the pixels in the coadded images were uncorrelated, then the aperture uncertainty  $\sigma_{\text{aperture}}$  would be related to the pixel-by-pixel uncertainty  $\sigma_{\text{bkg}}$  by a factor of the square-root of the number of pixels in the aperture. However, since both MULTIDRIZZLE and cross-convolution introduce correlations be-

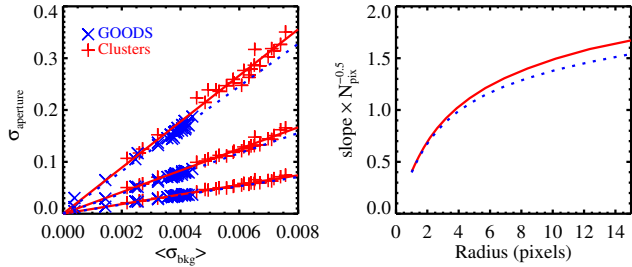


FIG. 2.— **Left:** Empirically measured photometric error contribution from background fluctuations in the  $i_{775}$  filter, including sky level, readout noise, and MULTIDRIZZLE artifacts. The x-axis is the average of  $\sigma_{\text{bkg}}$  for galaxies in the central region of each GOODS tile or cluster field, where  $\sigma_{\text{bkg}}$ , as described in the text, is the standard deviation of background pixels (in the pre – cross-convolved images) surrounding an individual galaxy. The y-axis is the standard deviation of circular sky apertures (in the cross-convolved images) of fixed radius in the central region of each GOODS tile or cluster field. The different curves from bottom to top are computed for aperture radii of 4.7, 8.4, and 15.0 pixels; solid red for cluster fields and dashed blue for GOODS tiles. The empirical relation is slightly different for the GOODS tiles compared to the cluster fields, presumably due to a different mosaic pattern and subsequent MULTIDRIZZLE artifacts. **Right:** The slope of the relation in the left-hand panel scaled by  $1/\sqrt{N_{\text{pix}}}$  as a function of aperture radius. The solid red curve indicates cluster fields and dashed blue curve indicates GOODS tiles. For uncorrelated pixels, this relation should be horizontal. The deviation from horizontal confirms that the pixels are correlated, justifying our empirical calibration.

tween nearby pixels, we need to empirically calibrate the relation between  $\sigma_{\text{aperture}}$  and  $\sigma_{\text{bkg}}$ . We measured  $\sigma_{\text{bkg}}$  (in the unconvolved coadded images) and the local background subtracted flux (in the cross-convolved coadded images) of 1000 sky apertures (selected to avoid galaxies and stars) in each cluster field and GOODS tile. For each aperture center we measured the flux at 15 different radii logarithmically spaced from 1 pixel to 15 pixels. For a given radius, the average value of  $\sigma_{\text{bkg}}$  for each field is tightly correlated with the standard deviation of the 1000 aperture fluxes for that field (Figures 2, 3). The correlation is slightly different between the cluster fields and the GOODS tiles, presumably due to different average exposure times, different mosaic patterns and subsequent MULTIDRIZZLE artifacts. The right-hand panels of Figures 2 and 3 show the deviations from the scalings expected for uncorrelated noise, which would show up as horizontal lines.

To apply these data to galaxies we interpolate the slope of the  $\sigma_{\text{aperture}} - \sigma_{\text{bkg}}$  relation from the data plotted in the right-hand panels of Figures 2 and 3 at the measured galaxy half-light radius  $R_e$ . In cases where  $R_e$  is larger than 15 pixels, we extrapolate using a linear fit to the data with radius between 8 and 15 pixels. This leads to an over-estimate of the background uncertainties for very bright galaxies. Fortunately, less than 6% of the red-sequence galaxies in our sample have  $R_e > 15$  pixels, and only 1% have  $R_e > 25$  pixels. In this way the background error is dependent on each individual object’s exposure depth (quantified by  $\sigma_{\text{bkg}}$ ), even when the exposure depth varies across the image. Errors in flux are then converted to errors in magnitude, and the cataloged color error is the sum in quadrature of the  $i_{775}$  magnitude error and the  $z_{850}$  magnitude error. Exposure depth varies from field to field, but typical uncertainties in  $i_{775} - z_{850}$  (for red galaxies) are 0.01 mag at  $z_{850} = 21$  mag and 0.05 mag at  $z_{850} = 24$  mag.

### 3.2. Quantitative morphology

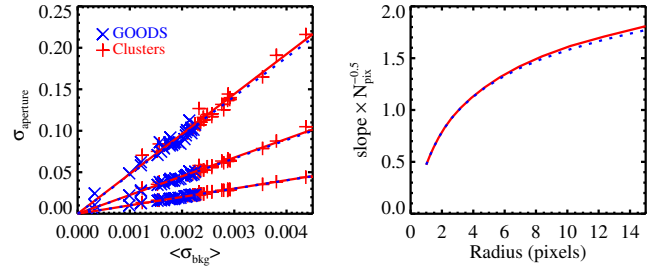


FIG. 3.— Same as Figure 2 but for the  $z_{850}$  filter.

We rely on quantitative morphology measurements to identify likely red-sequence members. The two parameters we use are the Gini coefficient (Abraham et al. 2003) and asymmetry (Abraham et al. 1996). The Gini coefficient is a measure of the inequality in the distribution of pixel fluxes belonging to a galaxy, independent of their positions. The minimum Gini coefficient of zero indicates perfect equality; i.e. the flux in each pixel is identical. The maximum Gini coefficient of one indicates maximum inequality, in which the total flux of all pixels within the chosen aperture is actually contained in just one pixel (and all other pixels contain zero flux). The concentrated cores of elliptical galaxies typically generate higher Gini coefficients for these galaxies than in later-type galaxies.

The asymmetry measures how poorly a galaxy image matches itself when rotated 180 degrees about its center. It is defined as half the sum of the absolute values of the 180 degree subtraction residual pixels divided by the sum of the unsubtracted pixels in a given aperture. Elliptical galaxies typically have smaller asymmetry than later-type galaxies.

Just as the crowding in cluster cores is an issue when forming SExtractor catalogs, it is also an issue when selecting apertures for morphology measurements. To overcome this difficulty, we construct interloper-subtracted images by using GALFIT to subtract models of nearby interfering galaxies for each target galaxy. For each interloper-subtracted image, a preliminary aperture is created by collecting all pixels exceeding  $1.5\sigma_{\text{bkg}}$  contiguous to the pixel at the target galaxy’s center. Using this aperture, we then compute the galaxy’s quasi-Petrosian flux (Abraham et al. 2007). If the calculation converges, then a new isophotal aperture is created by selecting pixels from the preliminary aperture which exceed the quasi-Petrosian flux. The quasi-Petrosian flux fails to converge for a small number of galaxies which are then excluded from the subsequent analysis. These galaxies are usually quite faint and would have had large uncertainties had the fits converged.

The Gini coefficient is measured within the isophotal aperture. Since the Gini coefficient calculation does not depend on the relative geometry of the aperture pixels but only on the pixel values, the error can be estimated from bootstrap resampling (Abraham et al. 2003) (i.e. by repeatedly resampling from the original pixel values, with replacement, and recomputing the Gini coefficient on these resamplings. We recompute the Gini coefficient this way 1000 times to determine the Gini coefficient probability distribution function for each galaxy and record the standard deviation of this distribution as the Gini coefficient error).

We measure the asymmetry within a symmetrized aperture consisting of the intersection of the isophotal aperture with its 180 degree rotation. The center of the rotation is fit iteratively to minimize the asymmetry (so the symmetrized

aperture changes with each iteration, depending on the current candidate center). Since the random fluctuations present in the background contribute some asymmetry (positive by definition), a correction must be applied. To estimate this correction, we generate 1000 Gaussian background images with standard deviation  $\sigma_{\text{bkg}}$  and measure their asymmetry (but without normalization) in the same symmetrized aperture as the galaxy. We can then subtract this background contribution to the galaxy’s asymmetry. The standard deviation of these background measurements is our estimated error for each galaxy’s asymmetry (note that galaxy photon noise is much smaller than the background noise).

### 3.3. Spectroscopy

As the *HST* Cluster SN Survey produced SN candidates, they were spectroscopically targeted using prescheduled observing time on DEIMOS on Keck II (Faber et al. 2003) and FOCAS on Subaru (Kashikawa et al. 2002) and with ToO requests on FORS1 and FORS2 on Kueyen and Antu at the VLT (Appenzeller et al. 1998). The FORS1, FORS2 and DEIMOS observations are described in Dawson et al. (2009); the FOCAS observations are described in Morokuma et al. (2010). By observing SN candidates through slitmasks we were able to simultaneously target likely cluster members and form spectroscopic catalogs of many galaxies in the cluster fields. Galaxy redshifts were found through cross-correlation with template eigenspectra derived from SDSS spectra (Agol et al. 2011).

The flux and equivalent width of the [O II] 3727Å emission line doublet was measured by fitting the simple stellar population (SSP) templates from Bruzual & Charlot (2003, hereafter BC03) assuming a Chabrier (2003) initial mass function to data on both sides of the feature to define the continuum. The flux and equivalent width were computed by integrating from 500 km/s blueward of the line centered at 3726.032Å to 500 km/s redward of the line centered at 3728.815Å. To mitigate slit losses in the spectroscopy, we normalized the spectra to the observed  $i_{775}$  photometric magnitude.

Additional literature redshifts and [O II] equivalent width measurements were used as available (Andreon et al. 2008; Bremer et al. 2006; Brodwin et al. 2006; Demarco et al. 2007; Eisenhardt et al. 2008; Hilton et al. 2007, 2009; Postman et al. 1998; Rosati et al. 1999; Stanford et al. 2002, 2005). Spectra of  $z > 0.9$  SN hosts from the *HST* Cluster SN Survey are presented in Figure 4. A few of these spectra merit individual discussion. The redshift of SN SCP06T1 is determined from a single well-detected emission line, which we assume to be [O II]. Likewise, the redshift of SN SCP06X26 is determined from a single [O II] emission line, however the detection of this line is much more tentative than for SN SCP06T1 and is only barely visible in the 2D spectrum. Finally, we have not identified any features in the spectrum of SN SCP06E12 that would allow us to determine a redshift. The color of this galaxy is consistent with the color of the red sequence of the targeted cluster in the same field of view, so it may be a cluster member. However, we note that the colors of the four early-type field SN hosts from the *HST* Cluster SN Survey identified later are also roughly consistent with the colors of the red sequences of the targeted clusters in their fields of view. Though there is considerable uncertainty in the redshift of SN SCP06E12 and its host, we follow through with our analysis of this galaxy assuming it is a cluster member. We note that it is not used for cosmological analyses or analyses of SN correlations with their hosts. All of the remaining SN

hosts have secure redshifts.

## 4. ANALYSIS

In this section we describe our determination of the red sequence in clusters and in the field, which we later use to characterize SN host galaxies. To consistently identify cluster red-sequence galaxies, especially in poorer clusters where the contrast between bluer foreground or late-type galaxies and the cluster red sequence is less distinct, we generate a composite red sequence using spectroscopically confirmed members of multiple clusters with colors loosely consistent with the red sequence. When there is no cluster red sequence with which to compare SN host galaxies, as is the case for the field hosted SNe in the *HST* Cluster SN Survey and for all the GOODS fields SNe, this composite red sequence will serve as the reference red sequence. We use an evolving SED model to  $K$ -correct and evolution correct red-sequence members from their original redshifts to a target redshift. In this way we predict the location of the red sequence across the redshift range of the clusters in the survey.

### 4.1. Quantitative morphology calibration

Cluster red sequences are dominated by early-type galaxies. To enhance the contrast of the red sequence against the background color magnitude diagram, we use the Gini coefficient and asymmetry from §3.2 to select these galaxies. We calibrate our selection against visually derived morphology catalogs (by co-author MP) for three clusters: ISCS J1432.4+3332, RDCS1252.9-2927, and ISCS J1438.1+3414 at redshifts 1.10, 1.24, and 1.41 respectively. Figure 5 shows the locus of  $red(i_{775} - z_{850} > 0.75)$  visually classified elliptical galaxies compared to other visually classified morphological types in the Gini coefficient – asymmetry plane. The color cut eliminates many of the bluer galaxies (which we are not interested in here) but is not so red (for these clusters) that red-sequence members are cut. To select visually classified ellipticals we can evidently choose galaxies with Gini coefficient greater than 0.45 and asymmetry less than 0.08, cuts which we refer to as our *narrower* morphological cuts. With these cuts,  $\sim 90\%$  of all red visually classified elliptical galaxies are selected. S0 galaxies make up about 40% of the objects selected. The contamination from late-type galaxies is  $\lesssim 5\%$ . Later, when we fit the CMRs of clusters we choose to use somewhat more lenient cuts of Gini  $> 0.4$  and asymmetry  $< 0.1$ , which we refer to as our *broader* morphological cuts. This increases the number of red-sequence early-type galaxies included by  $\sim 50\%$  but only increases the late-type contamination to  $\sim 10\%$ . The *broader* cuts further increase the contrast of the red sequence but, critically, we find they only marginally increase the scatter of the red sequence (from  $0.045 \pm 0.003$  to  $0.048 \pm 0.003$  when clusters are stacked; §6).

As an independent test of the reliability of our cuts, we also investigate the strength of [O II] line emission in the Gini coefficient – asymmetry plane. Figure 6 shows the locus of red galaxies with weak or no [O II] emission (equivalent width greater than  $-5\text{\AA}$ ). Our broader cuts select  $\sim 90\%$  of [O II] quiet galaxies, though the contamination of [O II] emitting galaxies is higher ( $\sim 35\%$ ) than the contamination of late-type galaxies in the visual morphology case. This is partly a selection effect: redshifts are easier to obtain from emission lines than from absorption lines so [O II] emitting galaxies are more likely to be spectroscopically confirmed as cluster



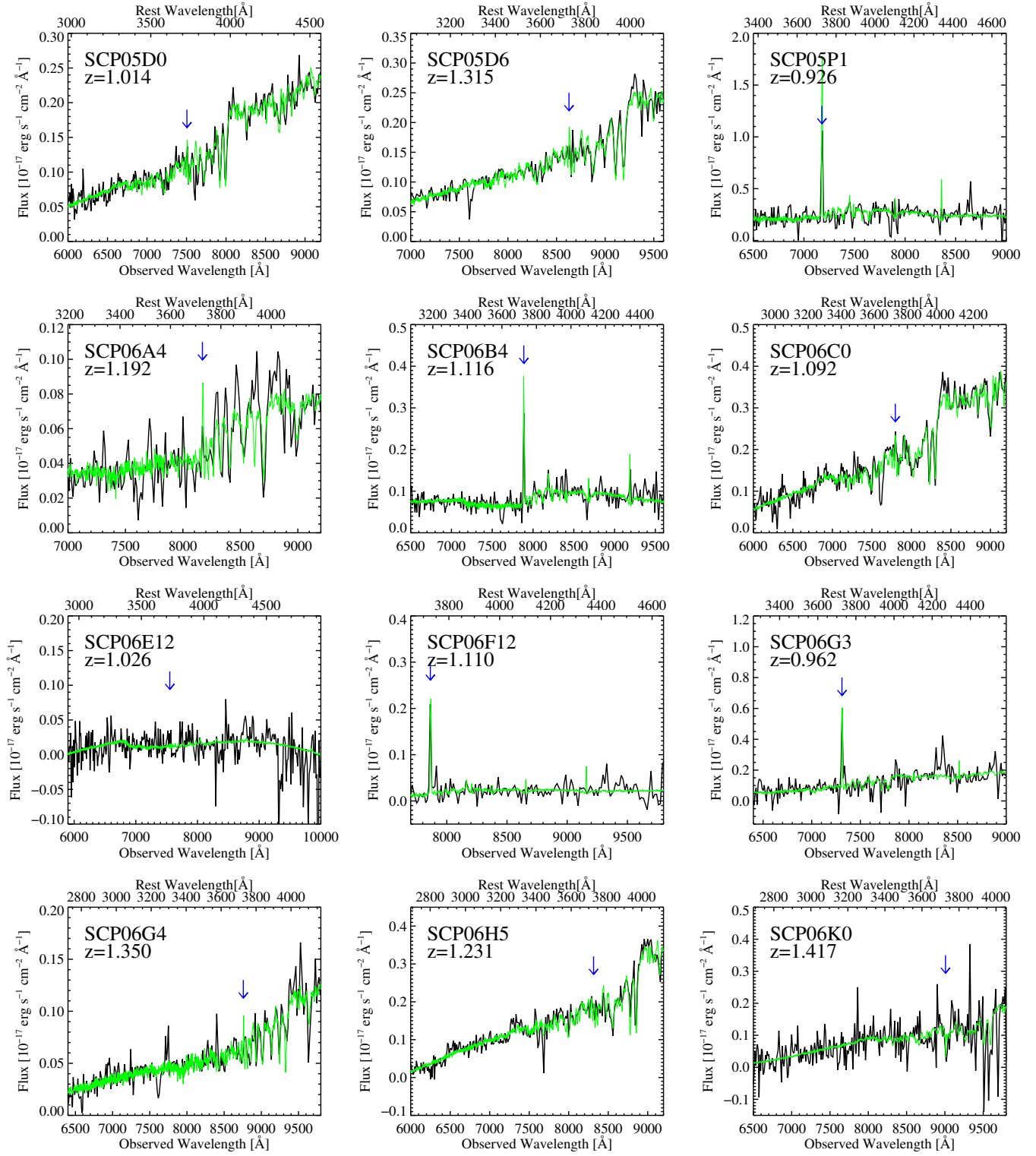


FIG. 4.— SCP supernovae host spectroscopy. For each host, data are in black, and the best fitting linear combination of eigenspectra at the fitted redshift is in green. The blue arrow indicates the wavelength of the [O II] 3727 emission line doublet. Note that the green line, used here for determining the redshift, is not the same as the BC03 template (which does not contain [O II] emission) used in fitting the [O II] equivalent width.

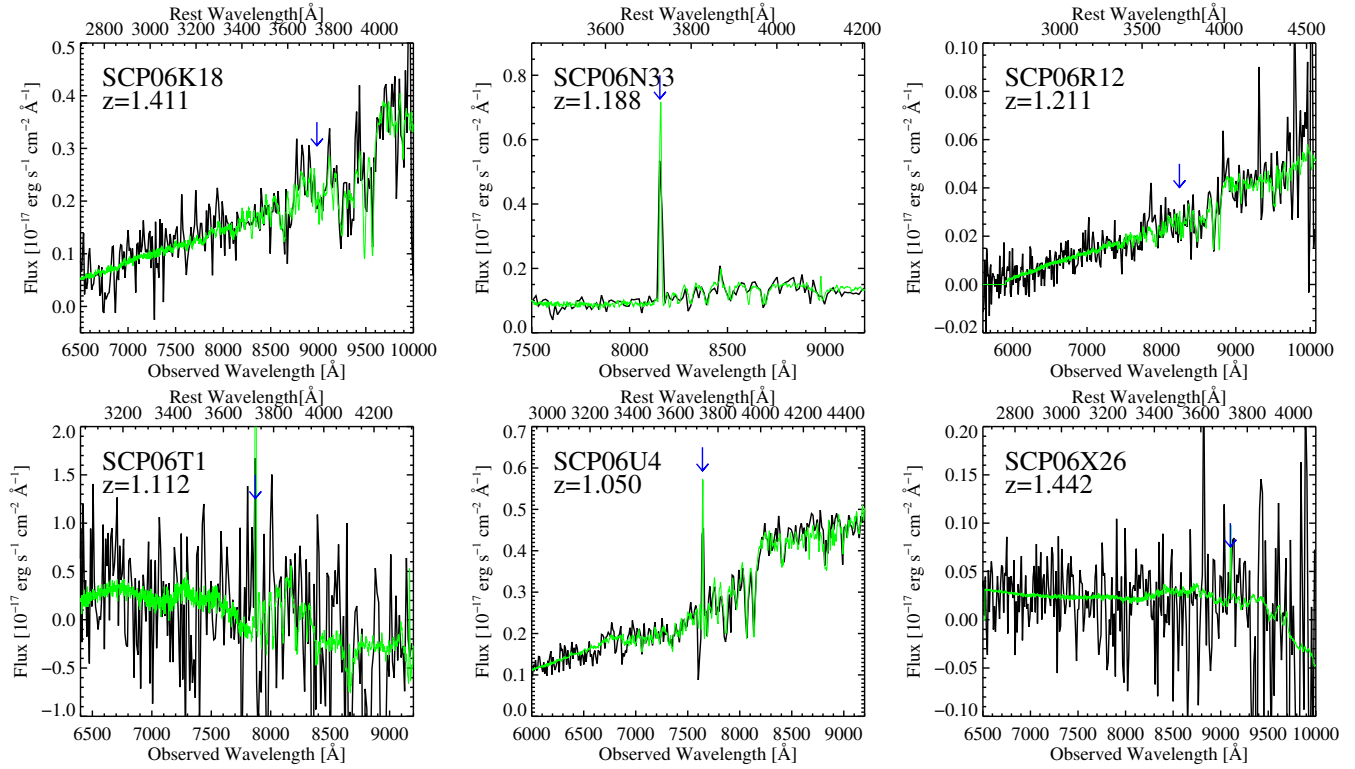


FIG. 4.— SCP supernovae host spectroscopy (continued)

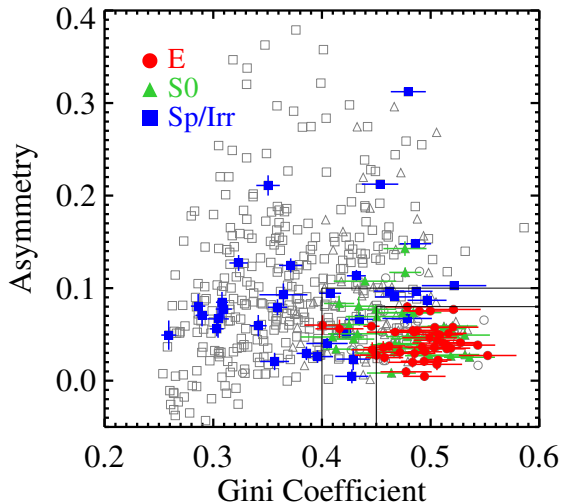


FIG. 5.— Comparison of visually derived morphologies to quantitative morphology measurements for three clusters. Blue boxes represent visually classified late-type galaxies with T-type from 0 to 6. Green triangles represent S0 galaxies with visual T-type from  $-2$  to  $-1$ . Red circles represent elliptical galaxies with visual T-type from  $-6$  to  $-3$ . Colored filled symbols represent galaxies with  $i_{775} - z_{850} > 0.75$ , consistent with the red sequence, light grey open symbols represent galaxies bluer than the red sequence. The two boxes in the lower-right show the position of our *broader* and *narrower* morphology cuts. The horizontal and vertical lines extending from plotting symbols indicate  $1\sigma$  uncertainties.

members and hence appear in the plot. The observed fraction of [O II] emitting galaxies is compatible with results reported in Postman et al. (2001), in which 45% of galaxies within the central  $1.0h_{65}^{-1}$  Mpc were observed to have [O II] equivalent width less than  $-15\text{\AA}$ . Also, Yan et al. (2006) have analyzed  $\sim 55000$  SDSS low-redshift spectra and determined that while nearly 38% of red galaxies show [O II] emission, only 9% of these show the emission line ratios characteristic of star formation. The remaining [O II]-emitting galaxies show line ratios indicative of LINERS or AGN. Lemaux et al. (2010) have recently extended this analysis to high-redshift by obtaining near-infrared spectroscopy of  $z > 0.8$  cluster galaxies. Of the five [O II]-emitting red-sequence early-type galaxies in their sample, four were found to be consistent with AGN/LINERS, with some evidence that the fifth might contain AGN/LINER activity as well. We are unable to directly check for AGN/LINER-like line ratios in our spectra because at high redshift the necessary comparison lines are shifted out of the wavelength range of our spectroscopic coverage. However, we suspect that most of the [O II]-emitting morphologically early-type red galaxies in our sample are not actively forming stars.

#### 4.2. The composite red sequence

The identification of red-sequence galaxies in clusters with incomplete spectroscopy can be challenging, especially for poorer clusters where it is difficult to distinguish red-sequence members from interloping galaxies in the foreground or background of the cluster. We therefore use the spectroscopically confirmed red-sequence members from all of our clusters to construct a composite red sequence which serves as both a guide for fitting the CMR of individual cluster red sequences and also as a reference red sequence for field elliptical SN

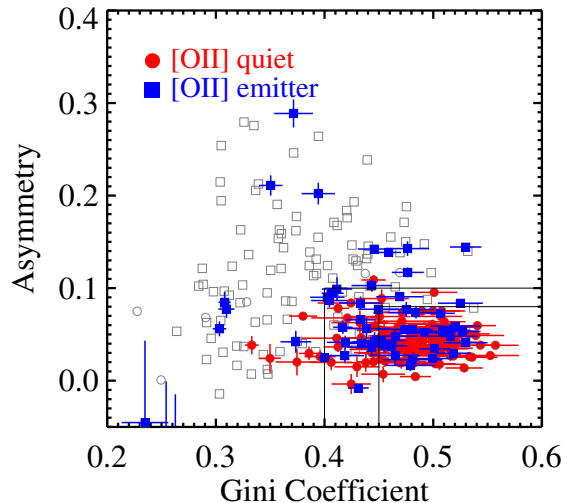


FIG. 6.— Spectroscopically confirmed galaxies' asymmetry and Gini coefficient distributions. Red circles indicate galaxies with an [O II] equivalent width greater than  $-5\text{\AA}$  (small or no emission). Blue squares indicate galaxies with strong [O II] emission with an equivalent width less than  $-5\text{\AA}$ . Colored filled symbols represent galaxies with  $i_{775} - z_{850} > 0.75$ , consistent with the red sequence, light grey open symbols represent galaxies bluer than the red sequence. The two boxes in the lower-right show the position of our *broader* and *narrower* morphology cuts. The horizontal and vertical lines extending from plotting symbols indicate  $1\sigma$  uncertainties.

hosts. We start by assuming that our sample of spectroscopically confirmed cluster members with quantitative morphology measurements consistent with elliptical galaxies (passing our broader morphology cuts) and colors loosely consistent with an old stellar population are each members of their own cluster's red sequence. By using a suitable  $K$ -correction and evolution correction, we can then project each galaxy's magnitude and color from their measured values at the galaxy's original redshift to a target redshift. To accomplish this we assume that the each sample galaxy's SED takes the form:

$$F_{\lambda} = \frac{M_{\text{gal}} \text{BC03}_{\lambda}(T(z), Z, z)}{M_{\odot} (D_L(z))^2} \quad (1)$$

where  $D_L(z)$  is the luminosity distance to redshift  $z$ ,  $\text{BC03}_{\lambda}(T(z), Z, z)$  indicates the luminosity density of the BC03 SSP template SED of age  $T(z)$  and metallicity  $Z$  with wavelength redshifted by  $(1+z)$ , and  $M_{\text{gal}}$  is the initial stellar mass of the BC03 template. We only have two band photometry for galaxies, so we can only constrain two parameters affecting the SED. One parameter needs to be the size of the galaxy ( $M_{\text{gal}}$ ), leaving the choice of either constraining the galaxy age or metallicity as the second parameter. Since these two parameters are largely degenerate, we simply fix the age  $T(z)$  such that galaxies all form at the same redshift  $z_{\text{form}}$  and fit for the metallicity  $Z$ . In a few cases, the range of colors produced by Equation 1 for the available BC03 metallicities was not red enough to cover the observed galaxy color. This could happen either because of a chance positive fluctuation of the galaxy color or because the particular galaxy happens to have formed earlier than our chosen  $z_{\text{form}}$ . Since we are not interested in the metallicity values themselves, but only in using them to project colors and magnitudes from one redshift to another, we allow this parameter

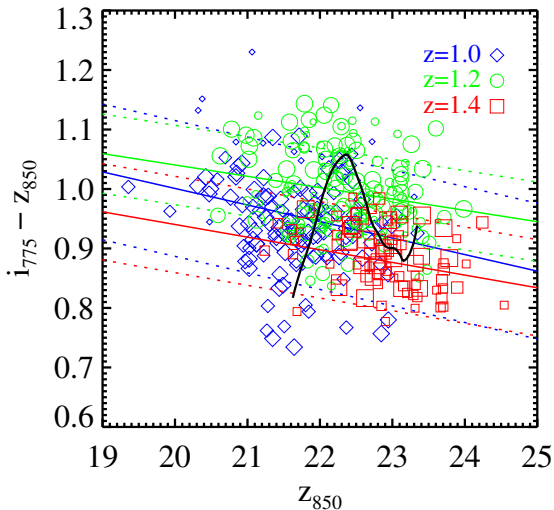


FIG. 7.— The composite red sequence at redshifts 1.0 (blue diamonds), 1.2 (green circles), and 1.4 (red squares), with linear fits. The size of the plotting symbol is proportional to the weight of the galaxy in the linear fit. The dashed lines indicate the measured residual scatter about the fits. The black line shows the predicted evolution from  $z = 0.9$  to  $z = 1.5$  of an  $L^*$  cluster member. The redward then blueward evolution of the red sequence with redshift is the result of the rest-frame 4000Å Balmer break crossing the gap between the  $i_{775}$  and  $z_{850}$  filters.

to be extrapolated outside of the BC03 range. In practice, we extrapolated metallicities for 27 out of 198 galaxies to a maximum of  $Z = 0.07$  (the range of BC03 metallicities is 0.0001 to 0.05) when choosing  $z_{\text{form}} = 3.0$ . To then project each galaxy to a target redshift, we evaluate the best-fit BC03 template at age  $T(z)$  given the target redshift  $z$ , which automatically captures luminosity evolution. We calculate  $i_{775}$  and  $z_{850}$  from this template. This procedure is imperfect, and in particular can introduce errors when  $K$ -correcting and evolution correcting over large differences in redshift. To mitigate this effect we de-weight galaxies with redshifts far from the target redshift. Specifically, we assign a Gaussian weight  $w \propto \exp(-(z - z_{\text{target}})^2 / (2 \cdot 0.15^2))$  to each galaxy. The characteristic size of the redshift window in this weighting, 0.15, is arbitrary but we have confirmed that our results do not significantly change with window sizes ranging from 0.10 to 0.25. The composite red sequences at redshifts 1.0, 1.2, and 1.4 are shown in Figure 7 for  $z_{\text{form}} = 3.0$ .

#### 4.3. Individual cluster red sequences

To determine the red sequences of individual clusters we assume a model in which galaxies are normally distributed with intrinsic scatter  $\sigma_{\text{int}}$  in color about the mean color-magnitude relation (characterized by slope  $m$  and intercept at  $z_{850} = 22$ ,  $b_{22}$ ) and have their magnitudes distributed like a Schechter (1976) function (described by parameters  $\phi^*$ ,  $L^*$  and  $\alpha$ ). Additionally, foreground and background galaxies will contaminate the color-magnitude diagram. We model the density of these galaxies in color-magnitude space as a plane characterized by its average value ( $B$ ) and derivatives with respect to magnitude and color ( $dB/dz_{850}$  and  $dB/d(i_{775} - z_{850})$ ). To break degeneracies between the red-sequence parameters and the foreground/background parameters, we simultaneously fit each cluster field with the GOODS fields which serve as a

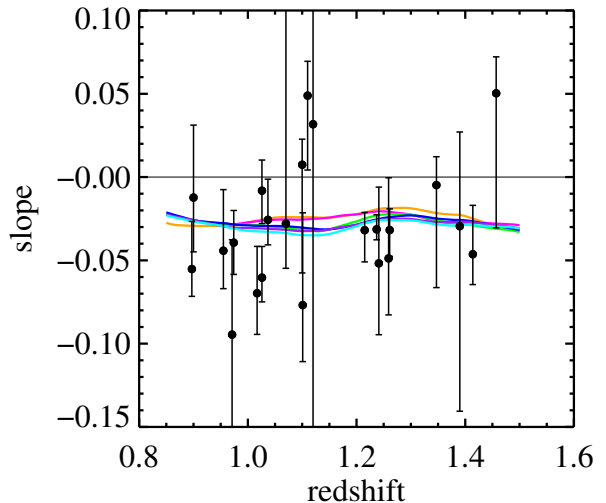


FIG. 8.— Comparison of the slopes of the composite red-sequence CMR fits to individual cluster CMR fits when allowing the slope to float. The multi-color curves are fits to the composite red sequence assuming different values of  $z_{\text{form}}$  in the range  $[2.5, 7.0]$ . The black points show the locations of maximum likelihood from the MCMC fits to 23 individual clusters. The errorbars are the smallest confidence intervals containing 68% of the marginal posterior probability.

control.

We consider only galaxies that pass our broader morphology cuts and fall within a redshift dependent color-magnitude rectangle for this analysis. The allowed color range is  $b_{22}^{\text{comp}} \pm 0.3$  mag where  $b_{22}^{\text{comp}}$  is the intercept of the composite red sequence. The allowed magnitude range is  $[M_{\text{model}}^* - 2.2, M_{\text{model}}^* + 1.0]$  where  $M_{\text{model}}^*$  is determined by passive evolution (Eqn. 1) of a red-sequence characteristic magnitude of  $z_{850} = 22.7$  at redshift  $z = 1.24$  (Blakeslee et al. 2003a). We construct a likelihood function for these galaxies and the GOODS fields control galaxies falling in the same color-magnitude rectangle as in Andreon et al. (2005) and use a Markov chain Monte Carlo algorithm to explore the nine-dimensional space ( $\sigma_{\text{int}}$ ,  $m$ ,  $b_{22}$ ,  $\phi^*$ ,  $L^*$ ,  $\alpha$ ,  $B$ ,  $dB/dz_{850}$  and  $dB/d(i_{775} - z_{850})$ ). The techniques presented in Dunkley et al. (2005) are used to determine the convergence of the Markov chains. The marginal distributions of fitting parameters can then be extracted directly from the Markov chains.

In Figure 8, we compare the slopes of individual cluster red-sequence CMRs to the slopes of the composite red-sequence CMRs generated assuming a variety of values of  $z_{\text{form}}$  between 2.5 and 7.0. The effects on the composite CMR slope of changing  $z_{\text{form}}$  are much smaller than the statistical uncertainties in individual CMR slope fits. In fact, the slopes of the individual cluster fits are statistically consistent with the narrow range of slopes of the composite red sequence regardless of  $z_{\text{form}}$  ( $\chi^2 = 19$  for 23 clusters assuming  $z_{\text{form}} = 3$  and changes negligibly for other values of  $z_{\text{form}}$ ). In order to consistently treat both field and cluster hosted SNe and also to avoid using physically perplexing positive slopes, we choose to fix the slope of each cluster to the value of the composite red sequence. We choose  $z_{\text{form}} = 3.0$  as a typical galaxy formation epoch and refit each cluster red-sequence CMR. The results of these fixed-slope fits are presented in Table 1.

TABLE 1  
COLOR-MAGNITUDE RELATION FITS

ID	Cluster Name	Redshift	Intercept	Slope	$\sigma(i_{775} - z_{850})$	$\sigma(U - V)_{z=0}$	$N_{\text{gal}}$
A	XMMXCS J2215.9-1738	1.457	0.923	-0.020	$0.051^{+0.034}_{-0.020}$	$0.101^{+0.068}_{-0.040}$	23.3
B	XMMU J2205.8-0159	1.12	1.028	-0.023	$0.040^{+0.186}_{-0.002}$	$0.079^{+0.372}_{-0.003}$	9.7
C	XMMU J1229.4+0151	0.974	0.906	-0.028	$0.066^{+0.003}_{-0.014}$	$0.131^{+0.007}_{-0.028}$	54.8
D	RCS J022144-0321.7	1.017	0.953	-0.026	$0.069^{+0.017}_{-0.017}$	$0.137^{+0.034}_{-0.035}$	32.1
E	WARPS J1415.1+3612	1.026	0.969	-0.025	$0.060^{+0.015}_{-0.013}$	$0.119^{+0.029}_{-0.026}$	27.0
F	ISCS J1432.4+3332	1.110	1.031	-0.023	$0.046^{+0.016}_{-0.016}$	$0.093^{+0.032}_{-0.031}$	18.8
G	ISCS J1429.3+3437	1.259	0.989	-0.019	$0.062^{+0.019}_{-0.034}$	$0.125^{+0.038}_{-0.068}$	23.3
H	ISCS J1434.4+3426	1.241	0.964	-0.018	$0.061^{+0.037}_{-0.013}$	$0.122^{+0.073}_{-0.026}$	22.5
I	ISCS J1432.6+3436	1.347	0.969	-0.023	$0.042^{+0.014}_{-0.025}$	$0.083^{+0.029}_{-0.050}$	14.8
J	ISCS J1434.7+3519	1.37	...	...	...	...	...
K	ISCS J1438.1+3414	1.414	0.944	-0.021	$0.008^{+0.011}_{-0.008}$	$0.016^{+0.023}_{-0.016}$	30.4
L	ISCS J1433.8+3325	1.37	...	...	...	...	...
M	CL J1604+4304	0.897	0.749	-0.026	$0.050^{+0.019}_{-0.006}$	$0.100^{+0.038}_{-0.012}$	27.1
N	RCS J022056-0333.4	1.026	0.982	-0.025	$0.043^{+0.014}_{-0.004}$	$0.086^{+0.027}_{-0.008}$	30.4
P	RCS J033750-2844.8	1.1 <sup>a</sup>	0.988	-0.023	$0.023^{+0.026}_{-0.010}$	$0.047^{+0.051}_{-0.020}$	15.6
Q	RCS J043934-2904.7	0.955	0.858	-0.027	$0.045^{+0.021}_{-0.010}$	$0.091^{+0.041}_{-0.019}$	24.8
R	XLSS J0223.0-0436	1.215	1.013	-0.019	$0.015^{+0.017}_{-0.015}$	$0.029^{+0.034}_{-0.029}$	20.6
S	RCS J215641-0448.1	1.07	1.022	-0.024	$0.005^{+0.084}_{-0.005}$	$0.010^{+0.168}_{-0.010}$	7.1
T	RCS2 J151104+0903.3	0.971	0.899	-0.028	$0.087^{+0.040}_{-0.023}$	$0.174^{+0.080}_{-0.045}$	15.7
U	RCS J234526-3632.6	1.037	0.957	-0.025	$0.047^{+0.015}_{-0.007}$	$0.093^{+0.030}_{-0.014}$	29.1
V	RCS J231953+0038.0	0.900	0.766	-0.026	$0.051^{+0.027}_{-0.007}$	$0.101^{+0.054}_{-0.015}$	30.3
W	RX J0848.9+4452	1.261	0.985	-0.019	$0.028^{+0.013}_{-0.005}$	$0.057^{+0.026}_{-0.009}$	20.1
X	RDCS J0910+5422	1.101	1.001	-0.023	$0.060^{+0.024}_{-0.012}$	$0.119^{+0.047}_{-0.024}$	18.4
Y	RDCS J1252.9-2927	1.237	0.965	-0.018	$0.029^{+0.003}_{-0.007}$	$0.058^{+0.007}_{-0.014}$	34.5
Z	XMMU J2235.3-2557	1.390	0.926	-0.022	$0.031^{+0.017}_{-0.016}$	$0.061^{+0.033}_{-0.032}$	17.4

NOTE. — Intercept indicates the CMR color at  $z_{850} = 22$ . The slope for each fit is fixed to the slope of the composite red sequence at the cluster redshift.  $\sigma(i_{775} - z_{850})$  ( $\sigma(U - V)_{z=0}$ ) is the observer-frame (rest-frame) intrinsic scatter of morphologically selected red-sequence members. The uncertainties reported indicate the smallest intervals containing 68% of the posterior probability for  $\sigma(i_{775} - z_{850})$  and  $\sigma(U - V)_{z=0}$ .  $N_{\text{gal}}$  is the effective number of red-sequence galaxies in the fitted magnitude range computed by integrating a Schechter function with the best fit values of  $\phi^*$ ,  $L^*$ , and  $\alpha$  over the magnitude range of the fit.

<sup>a</sup> Photometric cluster redshift.

## 5. SN HOST CLASSIFICATION

In this section, we describe how, for each SN host, we use the color–magnitude, quantitative morphology, and spectroscopic information to classify the host as either a passively evolving early-type galaxy, or a potentially star-forming late-type galaxy. We restrict our attention to redshifts greater than 0.9, which is the lowest cluster redshift in the *HST* Cluster SN Survey. Dawson et al. (2009) lists 17 SNe with  $z > 0.9$ . From this list we subtract SN SCP06C1, a spectroscopically confirmed SN Ia at  $z = 0.98$  with an uncertain host, but for completeness add SN SCP06E12 and SN SCP06X26 for consideration, which are likely  $z > 0.9$  SNe but lack conclusive spectroscopic redshifts. The host of SN SCP06E12 is faint but has photometry consistent with the red sequence of the cluster in the same field of view, and we assume here that its redshift is that of this cluster: 1.026. Spectroscopy of the host of SN SCP06X26 shows a possible emission line at 9100Å, which if [O II] indicates  $z = 1.44$ . There are 26  $z > 0.9$  SNe Ia discovered in surveys of the GOODS fields, 19 of which are spectroscopically confirmed as Type Ia (Gilliland et al. 1999; Blakeslee et al. 2003b; Riess et al. 2004, 2007).

We were unable to identify the host galaxy of one of these: HST04Gre. This SN is approximately 1.7'' from each of two potential hosts. Also, the host of SN1997ff has a tentative redshift much greater than that of any of the clusters considered here, preventing us from comparing its color and magnitude to the red sequence. We do not consider either of these SNe in the following analysis.

The principle criteria that our hosts must pass to be considered passively evolving early-types are: (A) they pass our broader morphology cuts and (B) they lie within  $2\sigma$  of the red sequence where  $\sigma = \sqrt{\sigma_{\text{int}}^2 + \sigma_{\text{col}}^2}$ , and  $\sigma_{\text{col}}$  is the color uncertainty. For (B) we use the cluster red sequence for cluster member hosts, and the composite red sequence with an assumed intrinsic scatter of 0.10 mag (greater than the measured intrinsic scatter of any of our clusters) for field hosts. Where spectroscopy is available, we also take note of possible star formation indicators.

In summary, from the *HST* Cluster SN Survey we classify six out of nine cluster SN hosts and four out of nine field SN hosts as early-type. One host galaxy, that of SN SCP06E12, we were unable to classify due to its faintness. The remaining

*HST* Cluster SN Survey hosts are classified as late-type. From the GOODS SN Survey, we classify seven out of 24 field SN hosts as early-type, and the remaining 17 hosts as late-type. Classifications are presented in Tables 2 and 3 and details are below.

### Early-type Hosts of SCP SNe

#### Cluster members

*SN SCP06H5*, *SN SCP06K18*, *SN SCP06R12*. The hosts of these three SNe Ia are spectroscopically consistent with early-type galaxies, have photometry placing them on their clusters' red sequences, and pass our narrower morphology cuts.

*SN SCP05D0*. The host of this SN has photometry placing it on its cluster's red sequence and passes our broader morphology cuts. The somewhat large asymmetry of this galaxy appears to result from a slightly skewed core light distribution, though not from any spiral structure or clumps of star formation. A small amount of [O II] emission is observed in its spectrum which might indicate star formation but is also not uncommon in passively evolving galaxies with LINERs in their cores.

*SN SCP06K0*. The host of this SN is spectroscopically consistent with an early-type galaxy, has photometry placing it on its cluster's red sequence, and passes our broader morphology cuts, though it has a somewhat small Gini coefficient. We note that the Gini coefficient is biased small for low signal-to-noise ratio images (Lotz et al. 2004) (such as the image of SN SCP06K0's host) and it is likely that with increased exposure time the Gini coefficient would increase.

*SN SCP06U4*. The host of this SN has photometry placing it on its cluster's red sequence and passes our narrower morphology cuts. Its spectrum exhibits moderate [O II] emission but otherwise is consistent with an early-type spectrum.

#### Field galaxies

*SN SCP06C0*, *SN SCP06D6*. The hosts of these SNe have photometry placing them on the composite red sequence and pass our narrower morphology cuts. Small amounts of [O II] emission are observed in their spectra.

*SN SCP06G4*. The host of this SN has photometry placing it on the composite red sequence and passes our narrower morphology cuts. Its spectrum shows relatively strong hydrogen Balmer absorption features consistent with an "E+A" spectrum (Dressler & Gunn 1983, 1992), which may indicate it is younger than the other early-type galaxies in our sample (though still likely older than the cutoff timescale for SNe CC).

*SN SCP06A4*. The host of this SN has photometry placing it on the composite red sequence and passes our narrower morphology cuts. A small amount of [O II] emission may be present in its spectrum and hydrogen Balmer absorption lines indicate an "E+A" classification.

### Late-type Hosts of SCP SNe

#### Cluster members

*SN SCP06B4*. The host of this SN fails our broader morphology cuts, is significantly bluer than its cluster's red sequence, and shows strong [O II] emission in its spectrum. It is likely that this galaxy is star-forming.

*SN SCP06F12*. Although the host of this SN only barely fails our broader Gini coefficient cut, its color is significantly bluer than its cluster's red sequence, and it shows strong [O II] emission in its spectrum.

#### Field galaxies

*SN SCP05P1*, *SN SCP06T1*. The hosts of these SNe fail both of our broader morphology cuts, are significantly bluer than the composite red sequence, and show strong [O II] emission in their spectra.

*SN SCP06N33*. Although the host of this SN passes our broader Gini coefficient cut, its color is significantly bluer than the composite red sequence and it shows strong [O II] emission in its spectrum.

*SN SCP06X26*. Although we do not detect strong [O II] emission from the host of this SN, it fails our broader Gini coefficient cut and its color is significantly blue.

*SN SCP06G3*. Although the host of this SN passes our narrow Gini coefficient cut, passes (barely) our broader asymmetry cut and is only moderately bluer than the composite red sequence, its spectrum shows very strong [O II] emission. We also note that the axis-ratio of the  $z_{850}$  GALFIT model for this galaxy ( $b/a = 0.25$ ) is  $3.5\sigma$  smaller than the model axis-ratios of the galaxies classified as early-types above; it is likely an edge-on disk galaxy.

### Unclassified Hosts of SCP SNe

*SN SCP06E12*. We do not have a redshift for the host of this SN. Its color is consistent with the red sequence of the cluster in the same field of view. Its Gini coefficient is small but this galaxy, like SN SCP06K0, has a low signal-to-noise ratio image and its Gini coefficient is likely biased low. We do not have enough information to classify this galaxy, and do not include it in any subsequent analysis in this paper.

### Host Galaxies of GOODS SNe

From the GOODS SN Survey, we analyze the morphology and photometry (but not spectroscopy) of 24 of the 26  $z > 0.9$  SN hosts mentioned in Riess et al. (2007). The hosts of seven SNe pass our morphological and photometric cuts: SN2003az, SN2003XX, SN2003es, HST04Sas, HST04Tha, HST05Lan and SN2002hp. Riess et al. (2007) classifies the hosts of all of these but SN2003az as elliptical. The remaining 17 GOODS SN Ia hosts analyzed here are classified as late-type.

## 6. SN TYPING BY HOST GALAXY

The classification of the supernovae discovered in the *HST* Cluster SN Survey uses several approaches simultaneously (see Barbary et al. (2010) for a discussion of the photometric and light curve constraints). Here we discuss the typing constraints that come from just the host galaxy information. These constraints are already quite strong.

As described in §2.1, classifying a SN as Type Ia when hosted by an early-type galaxy is a robust alternative to spectroscopic typing. However, it is natural to wonder if misclassification of the host galaxy and subsequently the SN is more frequent at high redshift, where morphological classification is more difficult and star formation more prevalent. To investigate this potential shortcoming, we estimate the *a priori* relative rates of detecting SNe Ia and SNe CC in the host

TABLE 2  
EARLY-TYPE  $z > 0.9$  SN HOSTS

Name	$z_{\text{host}}$	$z_{\text{cluster}}$	[O II] EW (Å)	Confidence Interval	Gini Coefficient	Asymmetry	$i_{775} - z_{850}$	CMR residual	Notes
<i>SCP Cluster SN Hosts</i>									
SN SCP05D0	1.014	1.017	-1.7	[-2.6, -0.6]	$0.525 \pm 0.021$	$0.084 \pm 0.003$	$0.939 \pm 0.021$	$-0.016 \pm 0.072$	s,h,x,c
SN SCP06H5	1.231	1.241	-0.4	[-1.5, -0.0]	$0.541 \pm 0.017$	$0.059 \pm 0.003$	$1.075 \pm 0.022$	$+0.106 \pm 0.065$	L,h
SN SCP06K0	1.416	1.414	-0.4	[-2.4, -0.0]	$0.419 \pm 0.018$	$0.027 \pm 0.008$	$0.951 \pm 0.066$	$+0.020 \pm 0.066$	L,h,x,c
SN SCP06K18	1.412	1.414	-0.1	[-0.7, -0.0]	$0.456 \pm 0.015$	$0.021 \pm 0.006$	$0.986 \pm 0.037$	$+0.038 \pm 0.038$	
SN SCP06R12	1.212	1.215	-0.2	[-1.1, -0.0]	$0.455 \pm 0.025$	$0.054 \pm 0.011$	$0.956 \pm 0.050$	$-0.019 \pm 0.052$	L,h
SN SCP06U4	1.050	1.037	-9.6	[-10.9, -8.1]	$0.481 \pm 0.018$	$0.055 \pm 0.004$	$0.926 \pm 0.017$	$-0.053 \pm 0.050$	s,c
<i>SCP Field SN Hosts</i>									
SN SCP06A4	1.193	1.457	-1.6	[-3.6, -0.0]	$0.468 \pm 0.021$	$0.020 \pm 0.006$	$0.976 \pm 0.044$	$-0.013 \pm 0.109$	L,h,x,c
SN SCP06C0	1.092	0.974	-3.6	[-5.6, -1.7]	$0.476 \pm 0.021$	$0.027 \pm 0.003$	$1.072 \pm 0.017$	$+0.014 \pm 0.101$	L,h,x,c
SN SCP05D6	1.314	1.017	-3.2	[-4.2, -2.2]	$0.516 \pm 0.017$	$0.043 \pm 0.005$	$0.960 \pm 0.027$	$+0.044 \pm 0.103$	L,h,x,c
SN SCP06G4	1.350	1.259	-0.3	[-1.5, -0.0]	$0.492 \pm 0.022$	$0.000 \pm 0.006$	$1.004 \pm 0.040$	$+0.103 \pm 0.108$	s,h,x,c
<i>GOODS SN Hosts</i>									
SN2002hp	1.305	...	...	...	$0.501 \pm 0.025$	$0.032 \pm 0.005$	$0.919 \pm 0.019$	$+0.015 \pm 0.102$	h,x,c
SN2003az	1.270	...	...	...	$0.435 \pm 0.023$	$0.054 \pm 0.008$	$0.927 \pm 0.048$	$+0.018 \pm 0.111$	s,h,x,c
SN2003es	0.954	...	...	...	$0.497 \pm 0.018$	$0.047 \pm 0.001$	$0.942 \pm 0.006$	$+0.039 \pm 0.100$	s,x,c
SN2003XX	0.935	...	...	...	$0.504 \pm 0.028$	$0.025 \pm 0.001$	$0.789 \pm 0.005$	$-0.081 \pm 0.100$	s,h,x,c
HST04Sas	1.390	...	...	...	$0.431 \pm 0.023$	$0.071 \pm 0.007$	$0.792 \pm 0.032$	$-0.081 \pm 0.105$	s,h,x,c
HST04Tha	0.954	...	...	...	$0.432 \pm 0.031$	$0.058 \pm 0.001$	$0.886 \pm 0.008$	$+0.027 \pm 0.100$	s,x,c
HST05Lan	1.235	...	...	...	$0.492 \pm 0.022$	$0.078 \pm 0.004$	$0.997 \pm 0.016$	$+0.050 \pm 0.101$	s,h,x,c

NOTE. — The [O II] EW reported is the median of the posterior probability of the true EW given the observed EW, the spectroscopic uncertainties, and a prior that the EW be positive. The reported confidence interval is the smallest interval containing 90% of the posterior probability. The CMR residual is computed using the fixed-slope fits to individual clusters for cluster member hosts and the composite red sequence fits for field hosts. The CMR residual uncertainties reported are  $\sqrt{\sigma_{\text{int}}^2 + \sigma_{\text{col}}^2}$  where  $\sigma_{\text{int}}$  is the measured intrinsic scatter of the parent cluster for cluster member hosts and a conservative 0.10 mag for field hosts.

<sup>s</sup> SN is classified as Type Ia from spectrum (Blakeslee et al. 2003a; Riess et al. 2004, 2007; Barbary et al. 2010)

<sup>L</sup> SN is classified as Type Ia from light curve (Riess et al. 2004, 2007; Barbary et al. 2010)

<sup>h</sup> SN passes Union2.1 cuts and has reliable Hubble residual measurement (Suzuki et al. 2011)

<sup>x</sup> SN has SALT2 X1 uncertainty less than 1.0 (Suzuki et al. 2011)

<sup>c</sup> SN has SALT2 color uncertainty less than 0.1 (Suzuki et al. 2011)

galaxies from the *HST* Cluster SN Survey which are classified as early-type in §5 (we also include the host of SN SCP06E12 for analysis in this section, as it is plausibly early-type, although we leave it as unclassified in §5).

A rough estimate of the *intrinsic* rate of SNe Ia in an individual galaxy can be made using the popular A+B SN Ia rate parameterization in which the rate is the sum of a term proportional to the ongoing star-formation rate and a term proportional to the stellar mass:

$$R_{SN_{Ia}} = AM + B\dot{M} \quad (2)$$

Several choices of  $A$  and  $B$  are available in the literature. We choose the values derived from photometric estimates of SN host masses and star formation rates in the SNLS:  $A = 5.3 \times 10^{-14} \text{yr}^{-1} M_{\odot}^{-1}$ ,  $B = 3.9 \times 10^{-4} M_{\odot}^{-1}$  (Sullivan et al. 2006). The values for  $A$  and  $B$  depend on which initial mass function (IMF) is assumed. The values above are derived assuming a Kroupa (2001) IMF, which is very similar to the Chabrier IMF with which the BC03 SSPs we have been using are generated.

The cosmic SN CC rate has been shown to be proportional to the cosmic star formation rate. By dividing the cosmic SN CC rate found in Bazin et al. (2009) at  $z = 0.3$  ( $R_{SN_{CC}} = 1.63 \times 10^{-4} (h_{70}^{-1} \text{Mpc})^{-3}$ ) by the cosmic star formation rate at  $z = 0.3$  found in Hopkins & Beacom (2006) of  $0.03 M_{\odot} \text{yr}^{-1} \text{Mpc}^{-3}$  (and converting from the modified Salpeter IMF used there to a Kroupa IMF) we can obtain a similar formula for SNe CC:

$$R_{SN_{CC}} = C\dot{M} \quad (3)$$

with  $C = 6.52 \times 10^{-3} M_{\odot}^{-1}$ .

To estimate the star formation rate in these galaxies we rely on the the spectroscopic [O II] luminosity. As mentioned ear-

lier, while [O II] may indicate star formation, it may also indicate LINER activity in an otherwise passive galaxy. The [O II]-inferred star formation rate should thus be viewed as an upper limit to the true star formation rate, which may be much less or even zero. We investigate the [O II]-inferred star formation rate parameterization of Kennicutt (1998) scaled to a Kroupa IMF:

$$\text{SFR}_{[\text{O II}]} (M_{\odot} \text{yr}^{-1}) = 2.65 \times 10^{-41} L_{[\text{O II}]} (\text{erg s}^{-1}) \quad (4)$$

The [O II]-inferred star formation rate is sensitive to galactic metallicity and dust. These are in turn correlated with the galaxy's stellar mass. Gilbank et al. (2010) have investigated the correlation of the nominal [O II]-inferred star formation rate with other more robust star formation rate indicators in different mass bins and derived an empirical correction as a function of galaxy stellar mass that accounts for trends in galaxy metallicity and dust:

$$\text{SFR}_{\text{corr}} = \frac{\text{SFR}_{\text{nom}}}{a \tanh[(x - b)/c] + d} \quad (5)$$

where  $\text{SFR}_{\text{corr}}$  is the corrected star formation rate,  $\text{SFR}_{\text{nom}}$  is the nominal star formation rate from Equation 4,  $x = \log(M_{*}/M_{\odot})$ ,  $a = -1.424$ ,  $b = 9.827$ ,  $c = 0.572$ , and  $d = 1.700$ . Since the cluster early-type SN hosts are quite massive, this correction is significant. We carry out our analysis both with and without this mass correction.

No [O II] is detected in the spectroscopy of many of the host galaxies in the *HST* Cluster SN Survey. Rather than infer that the star formation is simply zero for these galaxies, we use Bayes' theorem to derive the probability distribution of the true [O II] luminosity given the observed value, taking into account the observational uncertainties, and enforcing a prior that the [O II] luminosity must be positive (i.e. we perform

TABLE 3  
LATE-TYPE AND UNCLASSIFIED  $z > 0.9$  SN HOSTS

Name	$z_{\text{host}}$	$z_{\text{cluster}}$	[O II] EW ( $\text{\AA}$ )	Confidence Interval	Gini Coefficient	Asymmetry	$i_{775} - z_{850}$	CMR residual	Notes
<i>SCP Cluster SN Hosts</i>									
SN SCP06B4	1.116	1.12	-48.2	[-60.0, -36.0]	$0.362 \pm 0.010$	$0.144 \pm 0.011$	$0.281 \pm 0.045$	$-0.722 \pm 0.060$	
SN SCP06E12 <sup>a</sup>	1.026 <sup>b</sup>	1.026	-26.4	[-47.4, -0.0]	$0.358 \pm 0.017$	$0.056 \pm 0.017$	$0.985 \pm 0.143$	$+0.077 \pm 0.154$	L
SN SCP06F12	1.110	1.110	-80.0	[-103.8, -59.2]	$0.392 \pm 0.022$	$0.031 \pm 0.014$	$0.424 \pm 0.052$	$-0.549 \pm 0.070$	L,h
<i>SCP Field SN Hosts</i>									
SN SCP06G3	0.962	1.259	-69.1	[-75.6, -62.4]	$0.473 \pm 0.018$	$0.087 \pm 0.004$	$0.689 \pm 0.024$	$-0.200 \pm 0.103$	L
SN SCP06N33	1.188	1.026	-45.5	[-47.5, -43.6]	$0.426 \pm 0.013$	$0.131 \pm 0.007$	$0.606 \pm 0.033$	$-0.402 \pm 0.105$	L,h,x
SN SCP05P1	0.926	1.1 <sup>d</sup>	-49.8	[-53.0, -46.3]	$0.327 \pm 0.006$	$0.200 \pm 0.010$	$0.239 \pm 0.035$	$-0.612 \pm 0.106$	L,x
SN SCP06T1	1.112	0.971	-38.1	[-84.8, -0.0]	$0.333 \pm 0.021$	$0.119 \pm 0.042$	$0.167 \pm 0.262$	$-0.824 \pm 0.280$	
SN SCP06X26	1.44	1.101	-4.0	[-13.5, -0.0]	$0.367 \pm 0.020$	$0.024 \pm 0.020$	$0.448 \pm 0.079$	$-0.417 \pm 0.128$	L
<i>GOODS SN Hosts</i>									
SN2002dd	0.950	...	...	...	$0.345 \pm 0.016$	$0.114 \pm 0.018$	$0.187 \pm 0.037$	$-0.589 \pm 0.106$	s,h,x,c
SN2002fw	1.300	...	...	...	$0.365 \pm 0.012$	$0.113 \pm 0.007$	$0.647 \pm 0.043$	$-0.215 \pm 0.109$	s,h,x,c
SN2002fx	1.400	...	...	...	$0.304 \pm 0.018$	$0.024 \pm 0.025$	$0.278 \pm 0.107$	$-0.550 \pm 0.147$	L,h
SN2002ki	1.141	...	...	...	$0.376 \pm 0.009$	$0.091 \pm 0.006$	$0.522 \pm 0.039$	$-0.513 \pm 0.107$	s,h,x
SN2003eb	0.900	...	...	...	$0.396 \pm 0.011$	$0.150 \pm 0.004$	$0.267 \pm 0.019$	$-0.523 \pm 0.102$	s,x,c
SN2003aj	1.307	...	...	...	$0.419 \pm 0.021$	$0.143 \pm 0.007$	$0.589 \pm 0.031$	$-0.294 \pm 0.105$	L,h,x,c
SN2003ak	1.551	...	...	...	$0.469 \pm 0.026$	$0.104 \pm 0.004$	$0.333 \pm 0.026$	$-0.684 \pm 0.103$	L,c
SN2003dy	1.340	...	...	...	$0.405 \pm 0.012$	$0.279 \pm 0.004$	$0.492 \pm 0.014$	$-0.417 \pm 0.101$	s,h,x,c
HST04Eag	1.019	...	...	...	$0.389 \pm 0.008$	$0.200 \pm 0.003$	$0.370 \pm 0.013$	$-0.585 \pm 0.101$	s,h,x,c
HST04Mcg	1.357	...	...	...	$0.324 \pm 0.007$	$0.243 \pm 0.009$	$0.773 \pm 0.042$	$-0.124 \pm 0.108$	s,h,x,c
HST04Pat	0.970	...	...	...	$0.358 \pm 0.007$	$0.140 \pm 0.007$	$0.584 \pm 0.025$	$-0.330 \pm 0.103$	s,h,c
HST04Omb	0.975	...	...	...	$0.423 \pm 0.016$	$0.287 \pm 0.002$	$0.191 \pm 0.008$	$-0.704 \pm 0.100$	s,h,x,c
HST05Fer	1.020	...	...	...	$0.477 \pm 0.030$	$0.049 \pm 0.008$	$0.496 \pm 0.028$	$-0.410 \pm 0.104$	s,h,x,c
HST05Gab	1.120	...	...	...	$0.252 \pm 0.019$	$-0.088 \pm 0.048$	$0.618 \pm 0.187$	$-0.356 \pm 0.212$	s,h,x,c
HST05Koe	1.230	...	...	...	$0.284 \pm 0.007$	$0.119 \pm 0.011$	$0.625 \pm 0.117$	$-0.318 \pm 0.154$	s,x,c
HST05Red	1.189	...	...	...	$0.404 \pm 0.029$	$0.079 \pm 0.004$	$0.247 \pm 0.014$	$-0.730 \pm 0.101$	L,h,x,c
HST05Str	1.027	...	...	...	$0.336 \pm 0.006$	$0.121 \pm 0.007$	$0.496 \pm 0.038$	$-0.457 \pm 0.107$	s,h,c

NOTE. — The [O II] EW reported is the median of the posterior probability of the true EW given the observed EW, the spectroscopic uncertainties, and a prior that the EW be positive. The reported confidence interval is the smallest interval containing 90% of the posterior probability. The CMR residual is computed using the fixed-slope fits to individual clusters for cluster member hosts and the composite red sequence fits for field hosts. The CMR residual uncertainties reported are  $\sqrt{\sigma_{\text{int}}^2 + \sigma_{\text{col}}^2}$  where  $\sigma_{\text{int}}$  is the measured intrinsic scatter of the parent cluster for cluster member hosts and a conservative 0.10 mag for field hosts.

<sup>a</sup> Unclassified galaxy.

<sup>b</sup> Redshift undetermined; assumed to be a cluster member at  $z = 1.026$

<sup>d</sup> Photometric cluster redshift.

<sup>s</sup> SN is classified as Type Ia from spectrum (Blakeslee et al. 2003a; Riess et al. 2004, 2007; Barbary et al. 2010)

<sup>L</sup> SN is classified as Type Ia from light curve (Riess et al. 2004, 2007; Barbary et al. 2010)

<sup>h</sup> SN light curve passes Union2.1 cuts (Suzuki et al. 2011)

<sup>x</sup> SN has SALT2 X1 uncertainty less than 1.0 (Suzuki et al. 2011)

<sup>c</sup> SN has SALT2 color uncertainty less than 0.1 (Suzuki et al. 2011)

a likelihood analysis). The median star formation rates (both nominal and mass-corrected) from the posterior distributions are reported in Table 4.

To estimate the host galaxy stellar mass, we fit BC03 SSP templates as in Equation 1 to the observed  $i_{775}$  and  $z_{850}$  magnitudes, assuming  $z_{\text{form}} = 3.0$ . The best fitting value of  $M_{\text{gal}}$  is then the *initial* stellar mass of the template, but the *current* stellar mass, factoring in the rapid deaths of massive stars, is also supplied by BC03. With only two photometric bands available, we only attempt this mass measurement for galaxies which are classified as early-types in §5. The more complicated SEDs of late-type galaxies will generally require information from more photometric bands and a more sophisticated approach to mass measurements. The statistical uncertainty of this mass measurement is limited by the uncertainty in our photometric measurements, both in  $z_{850}$  magnitude and in  $i_{775} - z_{850}$  color. To this uncertainty, we also add a systematic uncertainty (in quadrature) to capture our ignorance of the precise star-formation histories and metallicities of these galaxies. By fitting BC03 composite stellar spectra of a variety of exponential and delayed exponential star-formation histories and various metallicities to the  $i_{775}$  and  $z_{850}$  photometry, we estimate that this systematic uncertainty in mass is around 25% or 0.1 dex. The host galaxy masses are re-

ported in Table 4.

With the masses and star formation rates derived above, we apply Eqns. 2 and 3 to estimate the *intrinsic* rates of SNe Ia and SNe CC in each host galaxy. One interesting consequence of Eqn. 2 is that the expected increase in the SN Ia rate due to recent star-formation (the B component) is only  $\sim 1\%$  -  $5\%$  for all of our early-type hosts except that of SN SCP06U4 for which the increase is  $\sim 30\%$ . The true enhancement may, in fact, be smaller if the observed [O II] luminosity contains LINER emission. This implies that our early-type hosted SNe Ia probably have old progenitors and hence are not associated with dust from recent star formation.

The intrinsic rates are a start, however, since we know *a priori* that the particular galaxies we are analyzing each hosted a *detectable* SN, it is more informative to estimate the *apparent* SN rates. For example, the apparent rate of a SN of type  $X$  given its intrinsic rate can be written:

$$R_{SN_X}^{\text{apparent}} = R_{SN_X}^{\text{intrinsic}} f_{SN_X}^{\text{detectable}} \quad (6)$$

where  $f_{SN_X}^{\text{detectable}}$  is the fraction of detectable SNe of type  $X$  for a particular galaxy. The  $z_{850}$  detection threshold for a point source in a single epoch of the *HST* Cluster SN Survey is about 25.3 (Barbary et al. 2010). However, since the SNe in question have passed quality cuts requiring detection in mul-



multiple epochs and multiple bands we adopt an effective  $z_{850}$  detection threshold for SN peak brightness of  $\sim 24.7$ . For each host galaxy, we estimate the fraction of SNe Ia and SNe CC with peak  $z_{850}$  magnitude brighter than this detection threshold using the rest frame  $R$ -band luminosity functions derived from the Lick Observatory Supernova Search (LOSS) Li et al. (2011). Using the maximum light spectral templates of Hsiao et al. (2007) for normal SNe Ia and Nugent et al. (2002) for SN1991bg-like and SN1991T-like SNe Ia, SNe Ibc, SNe II-N, SNe II-P, and SNe II-L we  $K$ -correct our  $z_{850}$  detection threshold to the rest frame  $R$ -band for each SN subtype. We estimate the fractions of detectable SNe Ia and SNe CC as the fractions of LOSS SNe Ia and SNe CC that exceed these  $K$ -corrected thresholds:

$$f_{SN_X}^{\text{detectable}} = N_{SN_X}^> / N_{SN_X} \quad (7)$$

where  $N_{SN_X}^>$  and  $N_{SN_X}$  are the number of SNe of type  $X$  brighter than their respective  $R$ -band threshold and the total number of SNe of type  $X$ , respectively. We find that even at  $z = 0.9$ , none of the 25 SNe Ibc and only four (three SNe II-N and one SN II-L) out of 80 SNe II from LOSS would have been detected in our survey. On the other hand, our survey would have discovered 55 out of 74 LOSS SNe Ia, or 53 out of 59 if sub-luminous SN1991bg-like and SN2002cx-like SNe Ia are excluded. We again employ Bayes' theorem to derive the probability distribution of the expected value of  $N_{SN_X}^>$  (and hence the probability distribution of  $f_{SN_X}^{\text{detectable}}$ ) assuming the observed number is Poisson distributed and a positive flat prior.

With probability distribution functions for the masses (assumed to be log-normally distributed), [O II] luminosities, and detectable fractions of SNe Ia and SNe CC for each galaxy, we can use a Monte Carlo simulation to sample from these distributions and derive a probability distribution function of the apparent rates of SNe Ia and SNe CC. Given the apparent rates, the probability that a SN is a SN CC is:

$$P(CC) = \frac{R_{SN_{CC}}^{\text{apparent}}}{R_{SN_{CC}}^{\text{apparent}} + R_{SN_{Ia}}^{\text{apparent}}} \quad (8)$$

The results of this analysis are shown in Table 4. Even under the assumption that [O II] traces star formation and not LINER activity, five of eleven SNe have  $P(CC) \leq 0.02$ , and four others have  $P(CC) \leq 0.15$ . One of the two remaining SNe, SN SCP06U4, is a spectroscopically confirmed Type Ia. The final remaining SN, SN SCP06E12, was already considered uncertain due to its lack of spectroscopic redshift, though its light curve is consistent with a Type Ia at the redshift of the cluster in the same field of view. In fact, for almost all of the early-type hosted SCP SNe, the already strong type constraints derived here from just the host galaxy information can be supplemented with additional constraints by considering the full SN light curve shapes, colors and magnitudes. Ten out of the eleven early-type hosted SCP SNe analyzed in this section have evidence independent of their hosts or spectra indicating that they are SNe Ia (for details, see paper II of this series: Barbary et al. 2010). (These SNe are indicated with a ‘‘L’’ in the Notes column of Table 4). The one remaining SN, SN SCP06K18, does not have sufficient early time coverage to constrain its type through its light curve. However, as indicated in Table 4, its massive early-type host and lack of [O II] emission strongly suggest it is a Type Ia.

## 7. EARLY-TYPE HOST DUST CONSTRAINTS

In this section we use measurements of the red sequence scatter to place constraints on the scatter of reddening affecting these galaxies. Under the assumption that at least some red-sequence galaxies have very low dust content, this scatter constraint also sets an absolute scale for dust.

### 7.1. Red-sequence scatter

Color-magnitude diagrams of each of our clusters are presented in Figure 15 in Appendix A. For most clusters, the red sequence is clearly visible as an overdensity of morphologically early-type galaxies with  $i_{775} - z_{850} \approx 1$ . For 23 of the 25 clusters, the marginal likelihood distributions for the cluster CMR intrinsic scatters show clear maxima between 0.0 and 0.1 magnitudes. The intrinsic scatter marginal likelihood distributions for clusters ICS J1434.7+3519 and ICS J1433.8+3325 are essentially flat from 0.0 up to 0.3 magnitudes (the largest scatter for which we sampled the posterior likelihood) because the clusters contain too few red early-type galaxies to constrain the fit. Using the CMR fits as a baseline with which to combine clusters, we find that the intrinsic scatter of the stacked ‘‘color-magnitude’’ diagram is 0.046 mag (Figure 9). Turning to individual clusters, we find that the best-fit intrinsic scatters of three clusters are consistent with zero. The best-fit intrinsic scatters of the remaining clusters range from 0.023 mag to 0.087 mag (see Table 1 for the best-fit values and uncertainties of each cluster’s intrinsic scatter).

To compare these observer-frame CMR scatter measurements to published scatter measurements at other redshifts, we first convert to the rest-frame  $\sigma(U - V)_{z=0}$  scatter. Using BC03 SSPs, we construct a library of mock galaxy spectra with a variety of formation redshifts, exponentially declining star-formation timescales, and metallicities. For each cluster redshift, we determine the relation between observer-frame  $i_{775} - z_{850}$  color and rest-frame  $U - V$  color through synthetic photometry of these library spectra. The slope of this relation evaluated at the observed CMR color ranges from  $\sim 1.9$  to  $\sim 3.2$  depending on the redshift; this is the desired multiplicative conversion factor from  $\sigma(i_{775} - z_{850})$  to  $\sigma(U - V)_{z=0}$ . Our rest-frame  $\sigma(U - V)_{z=0}$  estimates lie in the range  $\sim 0.02 - 0.19$  mag with a typical value of  $\sim 0.10$  mag and are listed in Table 1. This range and typical value are consistent with the compilation of rest-frame cluster scatters presented in Jaff e et al. (2011), which span the redshift range  $0.0 < z < 1.46$ . In the rest of this section we use the properties of cluster red sequences to constrain the amounts of dust present in cluster galaxies.

A precision upper limit on dust along the line of sight to each SN Ia seen in the early-type hosts analyzed here is not possible with this particular data set (this rest-frame color, in particular, is not as sensitive to dust as a broader color baseline would be); nonetheless, it is useful to outline a rough analysis to see that dust limits on these  $z > 1$  cluster-hosted SNe are consistent with the low dust values expected for red and dead hosts as outlined in §2.2.

We can estimate such limits using the expectation that dust will both redden the intercept of the CMR and broaden the scatter of CMR residuals. While it is conceivable that one could construct dust distributions such that blue star-forming galaxies are reddened to *precisely* fall on the CMR (and subsequently decrease the CMR scatter), we take this to be an unlikely scenario requiring fine tuning. In fact, since the effects

TABLE 4  
A PRIORI RATE ESTIMATES FOR EARLY-TYPE SCP SN HOST GALAXIES

Name	log(Mass)	median SFR $M_{\odot}\text{yr}^{-1}$	median $R_{SN,CC}^a$ $10^{-3}\text{yr}^{-1}$	median $R_{SN,Ia}^a$ $10^{-3}\text{yr}^{-1}$	$P(CC)$	Notes
<i>Nominal Star Formation Rates</i>						
SN SCP05D0	10.9	0.53	0.13 ( 3.43)	2.73 ( 3.95)	0.04	s,L
SN SCP05D6	11.4	2.56	0.23 ( 16.44)	7.82 (14.71)	0.03	L
SN SCP06A4	10.7	0.29	0.04 ( 1.85)	1.58 ( 2.53)	0.02	L
SN SCP06C0	11.2	2.20	0.42 ( 14.18)	6.60 ( 9.85)	0.06	L
SN SCP06E12 <sup>b</sup>	9.9	0.50	0.11 ( 3.19)	0.42 ( 0.63)	0.21	L
SN SCP06G4	11.2	0.12	<0.01 ( 0.75)	4.66 ( 9.02)	<0.01	s,L
SN SCP06H5	11.6	0.32	0.04 ( 2.06)	12.11 (20.77)	<0.01	L
SN SCP06K0	11.4	0.32	0.02 ( 2.09)	4.84 (14.08)	<0.01	L
SN SCP06K18	11.8	0.17	0.01 ( 1.08)	11.00 (32.12)	<0.01	L
SN SCP06R12	10.4	0.02	<0.01 ( 0.12)	0.78 ( 1.33)	<0.01	L
SN SCP06U4	11.1	7.45	1.90 ( 47.95)	6.82 (10.22)	0.22	s,L
<i>Mass-Corrected Star Formation Rates</i>						
SN SCP05D0	10.9	1.93	0.47 ( 12.44)	3.11 ( 4.51)	0.13	s,L
SN SCP05D6	11.4	9.26	0.84 ( 59.57)	9.20 (17.35)	0.08	L
SN SCP06A4	10.7	1.04	0.13 ( 6.70)	1.79 ( 2.87)	0.06	L
SN SCP06C0	11.2	7.99	1.51 ( 51.37)	8.13 (12.13)	0.15	L
SN SCP06E12 <sup>b</sup>	9.9	1.80	0.41 ( 11.55)	0.77 ( 1.18)	0.35	L
SN SCP06G4	11.2	0.42	0.03 ( 2.71)	4.78 ( 9.27)	<0.01	s,L
SN SCP06H5	11.6	1.16	0.15 ( 7.46)	12.42 (21.32)	0.01	L
SN SCP06K0	11.4	1.18	0.09 ( 7.57)	5.09 (14.86)	0.02	L
SN SCP06K18	11.8	0.61	0.05 ( 3.92)	11.14 (32.58)	<0.01	L
SN SCP06R12	10.4	0.07	<0.01 ( 0.44)	0.81 ( 1.38)	0.01	L
SN SCP06U4	11.1	27.01	6.87 (173.73)	11.94 (17.90)	0.36	s,L

<sup>a</sup> Rates in parentheses are *intrinsic* quantities. Rates not in parentheses are *apparent* and factor in SN detectability.

<sup>b</sup> Redshift undetermined; assumed to be a cluster member at  $z = 1.026$ . This galaxy is left unclassified in §6.2.

<sup>s</sup> Spectroscopically confirmed SN Ia.

<sup>L</sup> Light curve shape, color and magnitude consistent with Type Ia (Barbary et al. 2010).

of dust and age show different redshift evolution (see Figure 10), the amount of dust required in such a scenario would need to be fine-tuned to the specific cluster redshift. Furthermore, the typical timescale for dust destruction,  $\sim 10^7 - 10^8$  yr (Jones et al. 1996; Temi et al. 2007; Clemens et al. 2010), is significantly shorter than the typical ages of even the youngest  $z \sim 1.2$  red-sequence ellipticals ( $\sim 10^9$  yr) (Rettura et al. 2010), so we do not expect a difference in dust between blue and red extremes of the red sequence to play a role in the CMR residual scatter. Finally, a dust distribution in which each galaxy is reddened the same amount is a similarly unlikely fine-tuning scenario, and is inconsistent with findings in nearby ellipticals, in which infrared-inferred dust masses vary by several orders of magnitude (Tran et al. 2001; Temi et al. 2004, 2007).

## 7.2. Dust scatter

We begin by considering the dust constraints obtainable from the CMR scatter and then return below to the constraints from the CMR intercept. Although both age and metallicity affect the unextinguished colors of galaxies, following the literature (Bower et al. 1992; van Dokkum et al. 1998; Blakeslee et al. 2003a; Mei et al. 2009; Jaffé et al. 2011), we assume that age is the dominant variable affecting the unextinguished CMR residual scatter (and that metallicity is primarily responsible for the CMR slope). We therefore assume a constant metallicity model in which differences in age and differences in dust reddening create the observed CMR scatter.

As mentioned above, the observer-frame CMR scatter  $\sigma(i_{775} - z_{850})$  attributable to differences in galaxy ages evolves with redshift (Figure 10) due to the shifting overlap of filters with spectral features. In particular, above  $z \sim 1.2$ , the  $i_{775}$  and  $z_{850}$  filters no longer bracket the redshifted age-sensitive  $4000\text{\AA}$  Balmer break and the predicted scatter for a

given age distribution consequently sharply decreases. On the other hand, because the Cardelli et al. (1989) reddening law is smooth over the relevant wavelengths, the scatter attributable to a given distribution of dust is nearly constant with redshift. This complementary behavior permits us to simultaneously fit both the average cluster star-formation history and average cluster dust distribution using the scatter – redshift data gathered in §4.3.

We investigate the age-scatter model first described by van Dokkum et al. (1998) in which early-type galaxies are formed in delta function starbursts at times uniformly distributed in the interval  $(t(z_0), t_z - t_{\text{delay}})$ . Here  $t(z_0)$  indicates the epoch when cluster galaxies first form at redshift  $z_0$ ,  $t_z$  indicates the epoch at which the cluster is observed, and  $t_{\text{delay}}$  corrects for *progenitor bias* (van Dokkum & Franx 2001) by allowing time for galaxies which recently ceased star formation to become red and evolve morphologically so that they will be identified as red-sequence early-types. At any redshift, the scatter due to age variation can be computed from a population of synthetic BC03 galaxies generated with ages drawn from the distribution defined by  $z_0$  and  $t_{\text{delay}}$ . The amplitude of the effects of age variation may in general depend on the assumed metallicity. To test this dependency, we have carried out the present analysis for both  $Z = 0.02$  and  $Z = 0.05$ , which are appropriate for the masses of early-type galaxies studied here (Trager et al. 2000). The final results are essentially the same with either choice of metallicity. To additionally account for the effects of dust, we use the parameter  $\sigma(E(B - V)_{z=0})$ , the rest-frame scatter of  $B - V$  reddening. This is related to  $\sigma(E(i_{775} - z_{850}))$  by a redshift dependent multiplier, which we compute through synthetic photometry of typical early-type galaxy SEDs with and without dust, similar to the analysis above in which we compare our scatter measurements to the literature. The measured cluster scatters

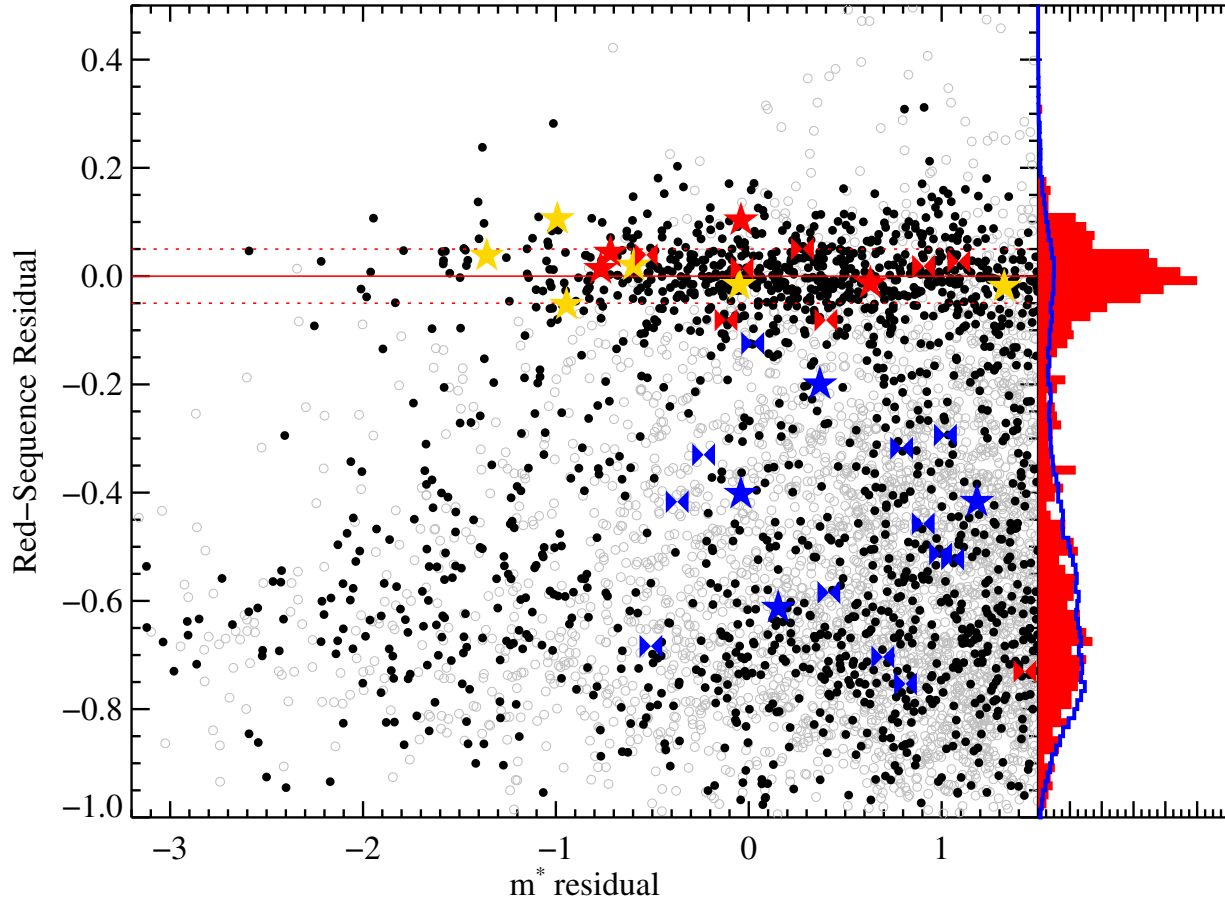


FIG. 9.— Stacked “Color-Magnitude” Diagram. The x-axis is galaxy  $z_{850} - m^*$  (where the characteristic magnitude,  $m^*$ , is modeled to passively evolve with redshift as described in the text) while the y-axis is galaxy color-magnitude relation residual:  $(i_{775} - z_{850}) - \text{CMR}$ . Open grey circles indicate galaxies which do not pass our broader morphological cuts; solid black circles do. The solid red line indicates zero CMR residual. The dashed red lines indicate the  $1\sigma$  intrinsic scatter of the stacked red sequence CMR. The red histogram on the right is the projection of CMR residuals for the stacked cluster galaxies. The blue histogram is the projection of CMR residuals for the GOODS control fields. The  $z > 0.9$  SN Ia hosts brighter than  $m^* + 1.5$  are overplotted as stars (HST Cluster SN Survey) or bowties (GOODS field SN surveys). Red (gold) stars and bowties indicate field (cluster) SN Ia hosts that meet our morphological and spectroscopic early-type criteria as described in §5. Blue stars and bowties indicate field or cluster SN Ia hosts that do not meet these criteria. Both the cluster and field early-type SN Ia hosts are consistent with the red sequence and may have similar properties such as low dust content and old stellar populations.

are fit with three parameters –  $z_0$ ,  $t_{\text{delay}}$ , and  $\sigma(E(B-V)_{z=0})$  – using a Markov Chain Monte Carlo. We find that the value of  $z_0$  has little effect on the model likelihood within the range  $4.0 < z_0 < 10.0$ . The most likely value for  $t_{\text{delay}}$  is 2.0 Gyr, which corresponds nicely to youngest spectroscopically measured red-sequence galaxy age in cluster RDCS J1252-2927 of  $1.9 \pm 0.5$  Gyr (Rettura et al. 2010). The maximum likelihood value for  $\sigma(E(B-V)_{z=0})$  is 0.031 mag, with 68% and 95% upper limits of 0.035 mag and 0.042 mag, respectively.

If clusters with higher intrinsic CMR residual scatter at a given redshift (such as ISCS J1434.4+3426 which hosts SN SCP06H5) in fact contain dustier galaxies, then their CMR intercepts should also be redder. We have further investigated this possibility by searching for a correlation between  $\Delta\sigma(i_{775} - z_{850})$  and  $\Delta b_{22}$  using pairs of clusters with  $|\Delta z| < 0.02$ . We find that the pair members with higher scatter are as likely to have bluer intercepts as redder intercepts. Thus the difference between the measured intrinsic scatter and the age-attributed intrinsic scatter should be interpreted only

as an upper limit to the dust content of a cluster, and not as a dust detection.

### 7.3. Absolute scale for dust

So far we have estimated approximately how much CMR residual scatter is attributable to dust. However, for SN measurements we are principally interested in the corresponding amount of reddening or extinction. To convert from residual scatter to reddening, we consider a toy model for dust. In a mid-infrared study of the cluster RXJ1716.4+6708, Koyama et al. (2008) found that only  $\sim 10\%$  of red cluster galaxies showed emission at  $15\mu\text{m}$  from dust (compared to  $\sim 50\%$  of blue cluster galaxies). As discussed in §2.2, studies of nearby early-type galaxies also suggest that at least some have very small levels of extinction. We therefore assume that most cluster early-type galaxies are unaffected by dust and that the distribution of dust in the remaining galaxies follows a half-Gaussian (we have also considered exponential, tophat and Dirac delta function distributions for the remaining galax-

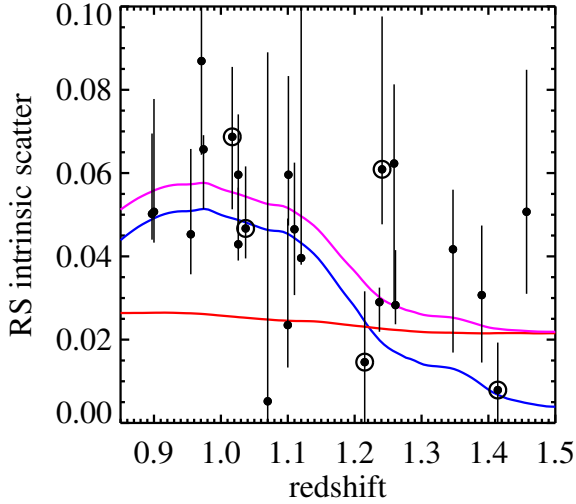


FIG. 10.— Measured early-type red-sequence scatter and fit assuming that CMR scatter is produced by scatter in galaxy ages and dust. The data points and error bars are our measurements and confidence intervals for the 23 clusters with scatter constraints. The blue line indicates the scatter attributable to age differences in our model, the red line indicates the scatter attributable to dust, and the magenta line indicates the combined scatter that is fit to the data. Clusters which hosted SNe Ia in early-type galaxies are circled. The steep evolution of the age-related scatter at  $z \sim 1.15$  is due to the shifting of the 4000Å Balmer break through the  $z_{850}$  filter. The SEDs of passive galaxies of different ages have smaller  $i_{775} - z_{850}$  color differences above this redshift because the filters no longer bracket the break. In contrast, the smooth dust extinction law produces scatter roughly independent of redshift.

ies; the differences are small). This highly simplified model captures the main features we wish to study here: a fraction of dusty galaxies (and hence a remaining fraction of nearly dust-free galaxies) and a characteristic scale for the amount of dust. The full probability distribution function for our toy dust model is:

$$f(X; f_d, \mu_d) = (1 - f_d) \delta(X) + f_d \frac{2\Theta(X)}{\pi\mu_d} \exp\left(\frac{-X^2}{\pi\mu_d^2}\right) \quad (9)$$

where the parameters  $f_d$  and  $\mu_d$  specify the fraction of dusty galaxies and the mean dust content of the subset of dusty galaxies, respectively;  $\delta(\cdot)$  is the Dirac delta function, which represents the dust-free galaxies (this term ensures that the integral over the full distribution is one),  $\Theta(\cdot)$  is the Heaviside step function, and  $X = E(B - V)_{z=0}$  quantifies the rest-frame galaxy reddening due to dust.

The scatter of our toy model, which can be calculated analytically, is  $\sigma(X) = \mu_d \sqrt{(\frac{\pi}{2} - f_d)f_d}$  (Figure 11). Thus, for  $\sigma(X) = 0.035$  (the 68% upper limit) we obtain constraints of  $f_d \lesssim 15\%$  if  $\mu_d$  is large ( $> 0.08$ ) or  $\mu_d \lesssim 0.06$  if  $f_d$  is large ( $> 0.3$ ). The implication for SNe hosted by red-sequence galaxies is that either the probability of being affected by dust at all is small or alternatively that the amount of dust affecting the SN is small. Turning our attention to individual SN host clusters, we see that the scatters of clusters RCS J234526-3632.6 (hosts SN SCP06U4), XLSS J0223.0-0436 (hosts SN SCP06R12), and ISCS J1438.1+3414 (hosts SCP06K0 and SCP06K18) at redshifts 1.037, 1.215, and 1.414 respectively, are below or just above the age-related scatter curve in Figure 10. Cluster RCS J022144-0321.7 (host of SCP06D0) at redshift 1.017 has more scatter than the three

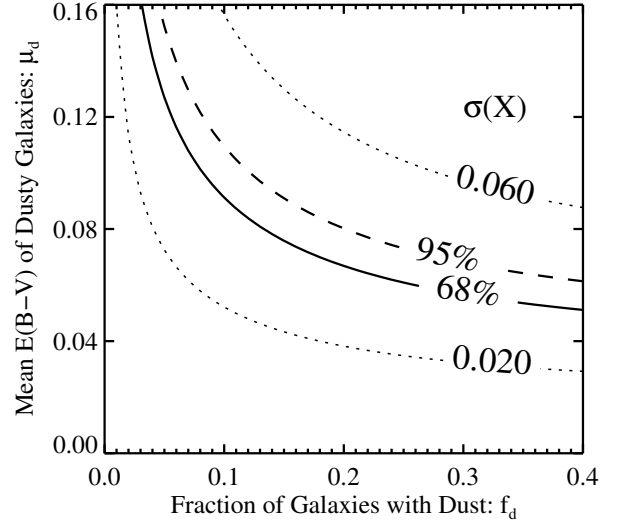


FIG. 11.— Contours of constant CMR residual scatter attributable to dust,  $\sigma(X)$ , in our toy model, in magnitudes. The model parameters  $f_d$  and  $\mu_d$  specify the fraction of dusty galaxies and the mean dust extinction of the subset of dusty galaxies, respectively. The solid and dashed contours indicate the  $1\sigma$  and  $2\sigma$  upper limits on  $\sigma(X)$  respectively. The  $\mu_d - f_d$  parameter space above these curves is excluded at the indicated level, implying that either the amount of dust in an individual cluster member is low ( $\mu_d$  is small), or that the probability that an individual cluster member is dusty is small ( $f_d$  is small).

other clusters within  $|\Delta z| < 0.02$ , but has the bluest intercept. Similarly, cluster ISCS J1434.4+3426 (host of SCP06H5) at redshift 1.241 has large intrinsic scatter but no more red an intercept than cluster RDCS J1252.9-2927 at redshift 1.237, which has only half as much scatter.

The dust constraints derived to this point apply to cluster early-type galaxies. However, Figure 9 demonstrates that the field early-type SN hosts have similar red-sequence residuals as cluster early-type SN hosts. The weighted mean residual of cluster early-type SN hosts is  $0.03 \pm 0.03$  whereas the weighted mean residual of field early-type SN hosts is  $-0.01 \pm 0.02$ . Thus, the field early-types are actually slightly bluer than cluster early-types and unlikely to have significant reddening.

## 8. SN IA CORRELATIONS WITH HOST GALAXIES

In this section we look at correlations between the properties of SN Ia light curves and the properties of SN Ia host galaxies at high redshift.

### 8.1. Stretch and color

One easily observed distance independent property of SNe Ia is the rate at which their light curves rise and fall. This property has been parameterized several ways in the literature: as the stretch,  $s$ , which linearly stretches the time axis of a template light curve to match the observed (rest-frame) light curve (Perlmutter et al. 1997),  $\Delta m_{15}(B)$ , which is the decline in  $B$ -band magnitudes from peak to 15 rest-frame days later (Phillips 1993), or  $x_1$ , which is roughly the coefficient of the first component in a principle component analysis of SN Ia spectral time series (Guy et al. 2007). The light curve shape has been shown to correlate with SN Ia host type at lower redshifts with the light curves of SNe Ia hosted by early-type

galaxies rising and falling more quickly than the light curves of SNe Ia hosted by late-type galaxies (i.e. early-type galaxies host SNe Ia with smaller stretch) (Hamuy et al. 1996; Gallagher et al. 2005; Sullivan et al. 2006). Here we compare SN stretch as a function of host type for our  $z > 0.9$  SN Ia dataset.

In Suzuki et al. (2011) we use SALT2 to fit light curves of  $z > 0.9$  SNe Ia from the *HST* Cluster SN Survey and the GOODS SN Surveys in the ACS  $i_{775}$ ,  $z_{850}$  filters and also the F110W and F160W filters of NICMOS. To convert the SALT2 light curve shape parameter  $x_1$  to stretch, we use the cubic relation from Guy et al. (2007). The distributions of stretch (and  $x_1$ ) for SN Ia subsets split by host type are shown in Figure 12. To prevent poorly measured SNe Ia from influencing our results, we have only included SNe Ia with  $x_1$  uncertainty less than 1.0, which is roughly the size of the histogram bins. The SNe Ia whose hosts we classify as passively evolving early-type galaxies show smaller stretch than the SNe Ia whose hosts we classify as late-type galaxies, consistent with lower redshift results. A Kolmogorov-Smirnov (K-S) test reveals that the probability that the stretch values from the two host subsets are drawn from the same distribution is  $< 0.01$ .

We have also compared the light curve shape distributions of these  $z > 0.9$  SNe Ia to that of the first year of SNLS SNe Ia at  $0.2 \lesssim z \lesssim 0.8$  presented in Sullivan et al. (2006, Figure 12). We assume that the individual values of stretch in the histogram plotted there are uniformly distributed within their bins. We find that the K-S probability that the  $s$  values of the early-type hosted SNe Ia analyzed in this paper and the  $s$  values of the passively hosted first year SNLS SNe Ia are drawn from the same distribution is quite high at 0.91. The K-S probability comparing the  $s$  distribution in  $z > 0.9$  late-type galaxies to that from the star-forming galaxies of first year SNLS SNe is also suggestive of similar distributions at 0.63. Finding similar demographics across such a wide redshift baseline instills confidence that SNe Ia are truly standardizable candles over this range.

Likewise, we can compare the distribution of the color parameter in both host subsets. In Figure 13 we compare the distribution of color for SN subsets of different host types. The K-S test reveals that the probability that the  $c$  values from the two host subsets are drawn from the same distribution is 0.75, also consistent with findings at lower redshift (Lampeitl et al. 2010). One possible explanation for this result is that the dominant source of color for these SNe Ia is intrinsic or circumstellar and that host galaxy extinction plays a smaller role.

### 8.2. SN Ia Hubble residual vs. host mass

Recent analyses of SN Ia hosts have indicated that after corrections for stretch and color have been applied, SNe Ia are brighter in galaxies with more stellar mass (Kelly et al. 2010; Sullivan et al. 2010; Lampeitl et al. 2010). Kelly et al. have parameterized this effect both as a step function at  $\log \frac{M}{M_\odot} = 10.8$  and as a linear function. In §6 we argued that the relatively simple SEDs of early-type galaxies (as opposed to the generally more complicated SEDs of late-type galaxies) allow us to measure stellar masses of early-type hosts using just the  $i_{775}$  and  $z_{850}$  photometry collected here. Thirteen of our  $z > 0.9$  SNe have both host mass measurements and Hubble residuals (uncorrected for host mass) from Suzuki et al. (2011). To extend this sample, we have also used the masses of  $z > 0.9$  GOODS SN hosts from Thomson & Chary (2011),

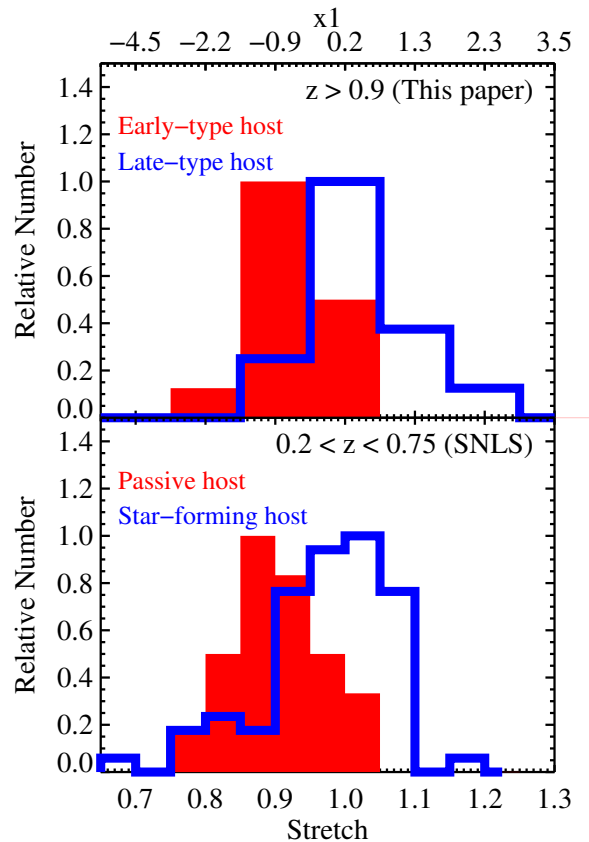


FIG. 12.— Distribution of SN light curve shape parameters stretch (bottom axis) and  $x_1$  (top axis). The  $x_1$  axis labels are computed using the cubic polynomial conversion from stretch given in Guy et al. (2007). Both axes apply to both panels. **Top:** Light curve shape distribution for the *HST*-observed  $z > 0.9$  SNe Ia discussed in the current paper. The red (blue) histogram corresponds to SNe Ia with hosts classified as early (late) type. **Bottom:** Light curve shape distribution for SNe drawn from the first year of SNLS as given in Sullivan et al. (2006). The red (blue) histogram corresponds to SNe Ia with hosts classified as passively-evolving (star-forming).

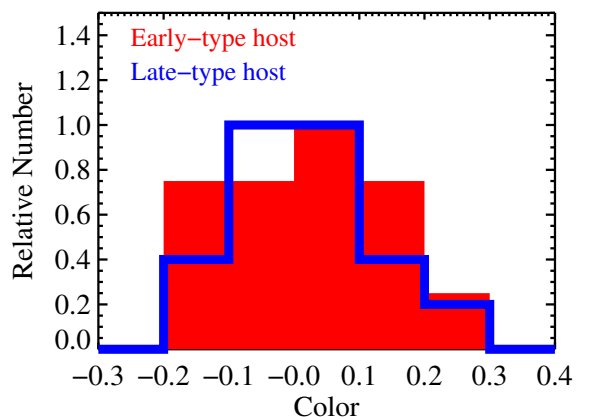


FIG. 13.— Distribution of  $z > 0.9$  SN Ia color for SNe with hosts classified as either early-type (red) or late-type (blue).

which are derived from SED fits to ACS optical, IRAC near infrared and MIPS  $24 \mu\text{m}$  photometry. The Hubble residuals

for these SNe are also available from [Suzuki et al. \(2011\)](#), increasing the sample from 13 to 23. Five galaxies with mass estimates are in common between the [Thomson & Chary \(2011\)](#) dataset and the early-type hosts analyzed here. For four of these galaxies, the difference in mass is less than  $1\sigma$ , and it is less than  $2\sigma$  for the fifth. In Figure 14, we plot Hubble residuals against host stellar masses, using our own mass estimates for the galaxies with two mass estimates. A suggestion of the trend of negative residuals for higher mass hosts is apparent. A linear fit to these data results in a slope measurement of  $-0.098 \pm 0.085 \text{ mag dex}^{-1}$ , (i.e. a  $1.1\sigma$  detection significance). The next generation of SN Ia studies (such as the SNe Ia discovered and followed with Wide Field Camera 3 as part of the *HST* Multi-Cycle Treasury Programs) may have sufficiently better data to confirm this trend at high redshift.

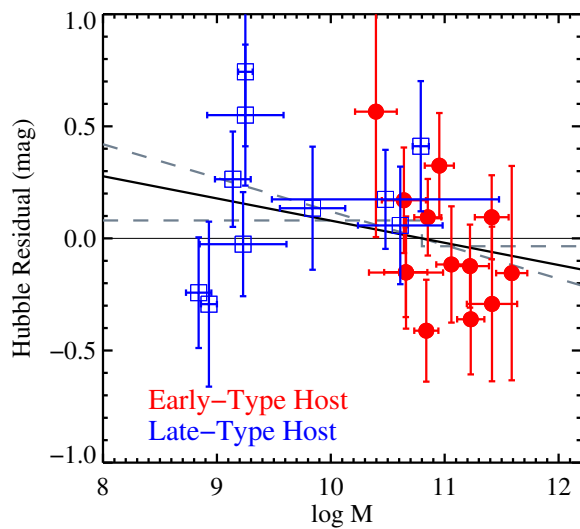


FIG. 14.— Hubble residual as a function of host galaxy stellar mass. Open blue squares are late-type galaxies with masses from [Thomson & Chary \(2011\)](#). Filled red circles are early-type galaxies with masses derived from SED fits to  $i_{775}$  and  $z_{850}$  as described in §8. The solid line is the best-fit linear relationship with slope  $-0.098 \pm 0.085 \text{ mag dex}^{-1}$ . The dashed line and step function are the relations plotted in [Kelly et al. \(2010\)](#) when using the SALT2 light curve fitter.

## 9. DISCUSSION AND CONCLUSIONS

In this paper, we have studied the relation between SNe Ia and their host galaxies at high redshift ( $z > 0.9$ ). In total, we study 16 SNe Ia (seven in clusters, eight in the field, and one with uncertain cluster membership) from the ACS cluster fields and 24 SNe Ia from the GOODS fields ([Dawson et al. 2009](#); [Gilliland et al. 1999](#); [Blakeslee et al. 2003b](#); [Riess et al. 2004, 2007](#)). Using color-magnitude diagrams constructed from  $i_{775}$  and  $z_{850}$  photometry and measurements of quantitative morphology, we have developed a technique to segregate high-redshift, early-type galaxies from high-redshift, late-type galaxies in these fields. Additional measurements of the [O II] emission line strength in the spectra of SN host galaxies were used to estimate galaxy star formation rates and the rate of core collapse SNe. This classification scheme was applied to the hosts of the 40 SNe, first in conjunction with the [O II] emission line strengths to determine the likelihood of early-type hosted SNe being Type Ia, then to identify trends in

the supernova properties with host galaxy type. Of the SNe Ia studied here, 17 have host galaxies classified as early-type, 22 have host galaxies classified as late-type, and one galaxy has a host which we have left unclassified.

From our analysis of these data, our principle results are:

**(i) SN Classification** A review of the literature ([Hakobyan et al. 2008](#)) shows that the confidence level is quite high for the classification of a SN Ia based on the identification of its host galaxy as early-type. We here confirm, on the basis of host morphology and spectroscopic limits on star formation, that SNe hosted by early-type galaxies in our current sample are likely Type Ia. Using the A+B SN Ia rate parameterization from [Sullivan et al. \(2006\)](#) (Eqn. 2), and by deriving a similar formula for SNe CC (Eqn. 3), we estimate the intrinsic rate of SNe Ia and SNe CC in individual early-type galaxies. By multiplying the intrinsic rates by the detectable fractions (derived from the detection threshold of the survey and the luminosity functions of different types of SNe) we calculate the rate of *detectable* SNe Ia and SNe CC for each early-type SN host. For most of the early-type hosted SNe in our survey, the probability of misclassification is very small, even if relying on only the host galaxy information. The three examples where the purely host galaxy classification is weakest ( $P(Ia) \lesssim 90\%$ ) can be traced back to observations of [O II] emission. If some or all of early-type galaxy [O II] emission is due to LINER activity instead of star formation, then these misclassification probabilities may be significantly overestimated. Fortunately, in this particular case two of these three SNe have been spectroscopically confirmed as a Type Ia. Of course, our combined classification for cosmological analysis includes the full light curve data and thus the classifications become much stronger ([Barbary et al. 2010](#); [Suzuki et al. 2011](#)). In the *HST* Cluster SN Survey, ten  $z > 0.9$  SNe in all can be typed by their early-type hosts, six more than a comparable blank field search would have found since this many were found in the clusters themselves.

**(ii) Contamination from Dust** The narrow color scatter about cluster red sequences directly constrains the amount of dust extinction affecting SNe in red-sequence hosts. We measure a typical intrinsic scatter in the observed  $i_{775} - z_{850}$  color of morphologically selected early-type galaxies of  $\sim 0.045$  magnitudes. While other authors have modeled this scatter as a distribution of galaxy ages (e.g. [Jaffé et al. 2011](#)), we have investigated extinction due to dust as an additional parameter. By simultaneously fitting the average cluster galaxy formation history and dust content, we conclude that the rest-frame  $B - V$  scatter of red sequence residuals attributable to dust is likely  $\lesssim 0.04$  magnitudes. By modeling this distribution as the sum of a dust-free galaxy population (with fraction  $1 - f_d$ ) and a dusty galaxy population (with fraction  $f_d$  and mean rest-frame  $E(B - V)$  reddening  $\mu_d$ ), we show that either the probability that any particular red-sequence member is reddened by dust is small ( $f_d \lesssim 15\%$ ) or alternatively that the amount of reddening is small ( $\mu_d \lesssim 0.06$ ). These limits are comparable to early-type galaxy reddening limits set at low redshift obtained by exploiting the correlation of the  $Mg_2$  absorption line and intrinsic  $B - V$  colors of early-type galaxies ([Ferguson 1993](#); [Schlegel et al. 1998](#)). We also find that the clusters with higher scatter have the same CMR intercepts as clusters with low scatter, contrary to expectation if dust were the primary factor in producing the color scatter.

**(iii) SN Light Curve Properties** The light curves of  $z > 0.9$  SNe Ia rise and fade more quickly (have smaller stretch) in early-type hosts than in late-type hosts. The distribution of

SN colors is similar in both host subsets, suggesting that SN Ia color is largely intrinsic or due to circumstellar dust and not dominated by host galaxy extinction. These trends are well known at lower redshifts (Hamuy et al. 1996; Gallagher et al. 2005; Sullivan et al. 2006; Lampeitl et al. 2010), but have not been demonstrated before at  $z > 0.9$ .

**(iv) Galaxy Mass and Hubble Residuals** We have obtained mass estimates of the early-type classified SN host subset by fitting passively-evolving SEDs to their  $i_{775}$  and  $z_{850}$  photometry. Together with infrared-derived mass estimates of a subset of the late-type classified SN hosts from Thomson & Chary (2011), we have found a suggestion of a correlation between SN Ia host mass and stretch-and-color-corrected Hubble residual ( $1.1\sigma$ ). This effect has been seen with more significance in three datasets at lower redshifts (Kelly et al. 2010; Sullivan et al. 2010; Lampeitl et al. 2010) and may be related to the metallicity or age of SN progenitors or to extinction by dust, all of which correlate with galaxy mass.

While the analysis in this paper focuses on the astrophysical properties of SNe Ia and their host galaxies, the results clearly have implications for the cosmological interpretation of SN observations. The evolution of host demographics with survey strategy or with redshift can lead to biases in cosmological parameter fits if not accounted for. In particular, many low redshift surveys explicitly target massive galaxies to improve their discovery rates. The cluster galaxies targeted by the *HST* Cluster SN Survey are also more massive on average than those in an untargeted survey and may produce SNe Ia which lead to biases in cosmological interpretation. A detailed analysis of the cosmological impact of host dependent properties is discussed in Suzuki et al. (2011). In that work, we present several other trends in SN Ia parameters as a function of host type, including the values of color-magnitude relation coefficient  $\beta = \Delta M_B / \Delta c$  in star-forming galaxies and in passive galaxies, and the residual scatter about the Hubble diagram for SNe Ia hosted by star-forming galaxies and by early-type galaxies. These studies are compared to similar studies at lower redshift (Sullivan et al. 2003; Jha et al. 2007; Sullivan et al. 2010; Lampeitl et al. 2010).

The ability to identify early-type galaxies, and their overdensity in clusters, provides many advantages in SN cosmology studies at  $z > 0.9$ . SNe hosted by early-type galaxies

are essentially all Type Ia, reducing the need for potentially expensive confirmation spectroscopy that must be obtained during the narrow time window that the SN is active. Cluster early-type galaxies are minimally contaminated with dust (either less than 15% are dusty or the reddening is less than 0.06 mag), and can be directly checked for dust via the cluster red-sequence scatter. The cluster galaxies provide additional potential SN Ia progenitors and hence yield a higher rate of SNe Ia than a comparable blank field search, especially of early-type hosted SNe Ia. Finally, the relatively simple SEDs expected for early-type galaxies permit SN host mass measurements with fewer photometric bands than for late-type hosts. Targeting clusters is therefore not only the most efficient method to discover and type SNe Ia at  $z > 0.9$ , but is likely the most efficient way to collect the host galaxy information necessary for the next generation of  $z > 0.9$  SN Ia studies.

We would like to thank a very helpful referee for suggestions that improved the quality of this paper. We would also like to thank Pasquale Temi for comments on the infrared dust properties of nearby early-type galaxies. Financial support for this work was provided by NASA through program GO-10496 from the Space Telescope Science Institute, which is operated by AURA, Inc., under NASA contract NAS 5-26555. This work was also supported in part by the Director, Office of Science, Office of High Energy and Nuclear Physics, of the U.S. Department of Energy under Contract No. AC02-05CH11231, as well as a JSPS core-to-core program ‘‘International Research Network for Dark Energy’’ and by a JSPS research grant (20040003). The authors wish to recognize and acknowledge the very significant cultural role and reverence that the summit of Mauna Kea has always had within the indigenous Hawaiian community. We are most fortunate to have the opportunity to conduct observations from this mountain. Finally, this work would not have been possible without the dedicated efforts of the daytime and nighttime support staff at the Cerro Paranal Observatory.

*Facilities:* HST (ACS), Subaru (FOCAS), Keck:II (DEIMOS), VLT:Kueyen (FORs1), VLT:Antu (FORs2)

## REFERENCES

- Abraham, R. G., et al. 2007, ApJ, 669, 184  
 Abraham, R. G., et al. 1996, ApJS, 107, 1  
 Abraham, R. G., van den Bergh, S., & Nair, P. 2003, ApJ, 588, 218  
 Agol, E., et al. 2011, submitted  
 Amanullah, R., et al. 2010, ApJ, 716, 712  
 Andreon, S., et al. 2008, MNRAS, 385, 979  
 Andreon, S., Punzi, G., & Grado, A. 2005, MNRAS, 360, 727  
 Appenzeller, I., et al. 1998, The Messenger, 94, 1  
 Astier, P., et al. 2006, A&A, 447, 31  
 Athey, A., et al. 2002, ApJ, 571, 272  
 Barbary, K., et al. 2010, arXiv:1010.5786  
 Barbary, K., et al. 2009, ApJ, 690, 1358  
 Barbary, K. et al. 2011, in prep  
 Bazin, G., et al. 2009, A&A, 499, 653  
 Bertin, E. & Arnouts, S. 1996, A&AS, 117, 393  
 Blakeslee, J. P., et al. 2003a, ApJ, 596, L143  
 Blakeslee, J. P., et al. 2003b, ApJ, 589, 693  
 Bower, R. G., Lucey, J. R., & Ellis, R. S. 1992, MNRAS, 254, 601  
 Bremer, M. N., et al. 2006, MNRAS, 371, 1427  
 Brodwin, M., et al. 2006, ApJ, 651, 791  
 Brodwin, M., et al. 2011, ApJ, 732, 33  
 Bruzual, G. & Charlot, S. 2003, MNRAS, 344, 1000  
 Caon, N., Macchetto, D., & Pastoriza, M. 2000, ApJS, 127, 39  
 Cardelli, J. A., Clayton, G. C., & Mathis, J. S. 1989, ApJ, 345, 245  
 Chabrier, G. 2003, PASP, 115, 763  
 Clemens, M. S., et al. 2010, A&A, 518, L50+
- Conley, A., et al. 2007, ApJ, 664, L13  
 Conley, A., et al. 2008, ApJ, 681, 482  
 Davies, J. I., et al. 2011, ArXiv e-prints  
 Dawson, K. S., et al. 2009, AJ, 138, 1271  
 Demarco, R., et al. 2007, ApJ, 663, 164  
 Donas, J., et al. 2007, ApJS, 173, 597  
 Dressler, A. & Gunn, J. E. 1983, ApJ, 270, 7  
 —. 1992, ApJS, 78, 1  
 Dunkley, J., et al. 2005, MNRAS, 356, 925  
 Dunkley, J., et al. 2009, ApJS, 180, 306  
 Eisenhardt, P. R. M., et al. 2008, ApJ, 684, 905  
 Eisenstein, D. J., et al. 2005, ApJ, 633, 560  
 Ellis, R. S., et al. 1997, ApJ, 483, 582  
 Faber, S. M., et al. 2003, in Society of Photo-Optical Instrumentation Engineers (SPIE) Conference Series, Vol. 4841, Society of Photo-Optical Instrumentation Engineers (SPIE) Conference Series, ed. M. Iye & A. F. M. Moorwood, 1657–1669  
 Faber, S. M., et al. 1989, ApJS, 69, 763  
 Ferguson, H. C. 1993, MNRAS, 263, 343  
 Ferrarese, L., et al. 2006, ApJS, 164, 334  
 Fioc, M. & Rocca-Volmerange, B. 1997, A&A, 326, 950  
 —. 1999, ArXiv Astrophysics e-prints  
 Förster, F. & Schawinski, K. 2008, MNRAS, 388, L74  
 Fruchter, A. S. & Hook, R. N. 2002, PASP, 114, 144  
 Gallagher, J. S., et al. 2005, ApJ, 634, 210  
 Gallazzi, A., et al. 2006, MNRAS, 370, 1106

- Giavalisco, M., et al. 2004, *ApJ*, 600, L93  
 Gilbank, D. G., et al. 2010, *MNRAS*, 405, 2594  
 Gilliland, R. L., Nugent, P. E., & Phillips, M. M. 1999, *ApJ*, 521, 30  
 Gladders, M. D., et al. 1998, *ApJ*, 501, 571  
 Gladders, M. D. & Yee, H. K. C. 2000, *AJ*, 120, 2148  
 Goudfrooij, P. & de Jong, T. 1995, *A&A*, 298, 784  
 Goudfrooij, P., et al. 1994, *A&AS*, 105, 341  
 Guy, J., et al. 2007, *A&A*, 466, 11  
 Hakobyan, A. A., et al. 2008, *A&A*, 488, 523  
 Hamuy, M., et al. 1996, *AJ*, 112, 2391  
 Häussler, B., et al. 2007, *ApJS*, 172, 615  
 Hicken, M., et al. 2009, *ApJ*, 700, 1097  
 Hilton, M., et al. 2007, *ApJ*, 670, 1000  
 Hilton, M., et al. 2009, *ApJ*, 697, 436  
 Hopkins, A. M. & Beacom, J. F. 2006, *ApJ*, 651, 142  
 Hsiao, E. Y., et al. 2007, *ApJ*, 663, 1187  
 Hsiao, E. Y., et al. 2011, in *The 2010 HST Calibration Workshop*, ed. S. Deustua, C. Oliveira  
 Huang, X., et al. 2009, *ApJ*, 707, L12  
 Jaffé, Y. L., et al. 2011, *MNRAS*, 410, 280  
 Jee, M. J., et al. 2011, *arXiv:1105.3186*  
 Jee, M. J., et al. 2009, *ApJ*, 704, 672  
 Jha, S., Riess, A. G., & Kirshner, R. P. 2007, *ApJ*, 659, 122  
 Jones, A. P., Tielens, A. G. G. M., & Hollenbach, D. J. 1996, *ApJ*, 469, 740  
 Kaneda, H., et al. 2007, *PASJ*, 59, 107  
 Kashikawa, N., et al. 2002, *PASJ*, 54, 819  
 Kauffmann, G. & Charlot, S. 1998, *MNRAS*, 294, 705  
 Kaviraj, S., et al. 2008, *MNRAS*, 388, 67  
 Kaviraj, S., et al. 2007, *ApJS*, 173, 619  
 Kaviraj, S., et al. 2011, *ArXiv e-prints*  
 Kawabata, K. S., et al. 2010, *Nature*, 465, 326  
 Kelly, P. L., et al. 2010, *ApJ*, 715, 743  
 Kennicutt, Jr., R. C. 1998, *ARA&A*, 36, 189  
 Knapp, G. R., et al. 1989, *ApJS*, 70, 329  
 Kodama, T. 1997, PhD thesis, Institute of Astronomy, Univ. Tokyo, (1997)  
 Kodama, T. & Arimoto, N. 1997, *A&A*, 320, 41  
 Koekemoer, A. M., et al. 2002, in *The 2002 HST Calibration Workshop : Hubble after the Installation of the ACS and the NICMOS Cooling System*, ed. S. Arribas, A. Koekemoer, & B. Whitmore, 337  
 Komatsu, E., et al. 2011, *ApJS*, 192, 18  
 Kowalski, M., et al. 2008, *ApJ*, 686, 749  
 Koyama, Y., et al. 2008, *MNRAS*, 391, 1758  
 Kroupa, P. 2001, *MNRAS*, 322, 231  
 Kuntschner, H., et al. 2006, *MNRAS*, 369, 497  
 Lampeitl, H., et al. 2010, *ApJ*, 722, 566  
 Lauer, T. R., et al. 2005, *AJ*, 129, 2138  
 Lemaux, B. C., et al. 2010, *ApJ*, 716, 970  
 Leonard, D. C. 2010, *The Astronomer's Telegram*, 2750, 1  
 Li, W., et al. 2011, *MNRAS*, 412, 1441  
 Lidman, C., et al. 2008, *A&A*, 489, 981  
 Lotz, J. M., Primack, J., & Madau, P. 2004, *AJ*, 128, 163  
 Mannucci, F., et al. 2005, *A&A*, 433, 807  
 Mathews, W. G. & Brighenti, F. 2003, *ApJ*, 599, 992  
 Mei, S., et al. 2006a, *ApJ*, 639, 81  
 Mei, S., et al. 2009, *ApJ*, 690, 42  
 Mei, S., et al. 2006b, *ApJ*, 644, 759  
 Melbourne, J., et al. 2007, *AJ*, 133, 2709  
 Morokuma, T., et al. 2010, *PASJ*, 62, 19  
 Nobili, S. & Goobar, A. 2008, *A&A*, 487, 19  
 Nugent, P., Kim, A., & Perlmutter, S. 2002, *PASP*, 114, 803  
 Peng, C. Y., et al. 2010, *AJ*, 139, 2097  
 Percival, W. J., et al. 2010, *MNRAS*, 401, 2148  
 Perets, H. B., et al. 2010, *Nature*, 465, 322  
 Perlmutter, S., et al. 1999, *ApJ*, 517, 565  
 Perlmutter, S., et al. 1997, *ApJ*, 483, 565  
 Phillips, M. M. 1993, *ApJ*, 413, L105  
 Postman, M., et al. 2005, *ApJ*, 623, 721  
 Postman, M., Lubin, L. M., & Oke, J. B. 1998, *AJ*, 116, 560  
 —. 2001, *AJ*, 122, 1125  
 Rest, A., et al. 2001, *AJ*, 121, 2431  
 Rettura, A., et al. 2010, *ApJ*, 709, 512  
 Riess, A. G., et al. 1998, *AJ*, 116, 1009  
 Riess, A. G., et al. 2007, *ApJ*, 659, 98  
 Riess, A. G., et al. 2004, *ApJ*, 607, 665  
 Riposte, P. et al. 2011, in prep  
 Rix, H.-W., et al. 2004, *ApJS*, 152, 163  
 Rosati, P., et al. 1999, *AJ*, 118, 76  
 Rosati, P., et al. 2009, *A&A*, 508, 583  
 Santos, J. S., et al. 2009, *A&A*, 501, 49  
 Sarzi, M., et al. 2006, *MNRAS*, 366, 1151  
 Schawinski, K., et al. 2007, *ApJS*, 173, 512  
 Schechter, P. 1976, *ApJ*, 203, 297  
 Schlegel, D. J., Finkbeiner, D. P., & Davis, M. 1998, *ApJ*, 500, 525  
 Sirianni, M., et al. 2005, *PASP*, 117, 1049  
 Stanford, S. A., et al. 2005, *ApJ*, 634, L129  
 Stanford, S. A., Eisenhardt, P. R., & Dickinson, M. 1998, *ApJ*, 492, 461  
 Stanford, S. A., et al. 2002, *AJ*, 123, 619  
 Strazzullo, V., et al. 2010, *A&A*, 524, A17+  
 Suh, H., et al. 2011, *ApJ*, 730, 110  
 Sullivan, M., et al. 2010, *MNRAS*, 406, 782  
 Sullivan, M., et al. 2003, *MNRAS*, 340, 1057  
 Sullivan, M., et al. 2006, *ApJ*, 648, 868  
 Suzuki, N., et al. 2011, *ArXiv:1105.3470*  
 Sérsic, J. L. 1968, *Atlas de galaxies australes*, ed. Sérsic, J. L.  
 Temi, P., Brighenti, F., & Mathews, W. G. 2007, *ApJ*, 660, 1215  
 —. 2009a, *ApJ*, 695, 1  
 —. 2009b, *ApJ*, 707, 890  
 Temi, P., et al. 2004, *ApJS*, 151, 237  
 Thomson, M. G. & Chary, R. R. 2011, *ApJ*, 731, 72  
 Tomita, A., et al. 2000, *AJ*, 120, 123  
 Trager, S. C., et al. 2000, *AJ*, 120, 165  
 Tran, H. D., et al. 2001, *AJ*, 121, 2928  
 Tripp, R. 1998, *A&A*, 331, 815  
 van Dokkum, P. G. & Franx, M. 1995, *AJ*, 110, 2027  
 —. 2001, *ApJ*, 553, 90  
 van Dokkum, P. G., et al. 1998, *ApJ*, 500, 714  
 Wood-Vasey, W. M., et al. 2007, *ApJ*, 666, 694  
 Yan, R., et al. 2006, *ApJ*, 648, 281  
 Yi, S. K., et al. 2005, *ApJ*, 619, L111

## APPENDIX

Here we present the color-magnitude diagrams for the 25 clusters in the *HST* Cluster SN Survey.



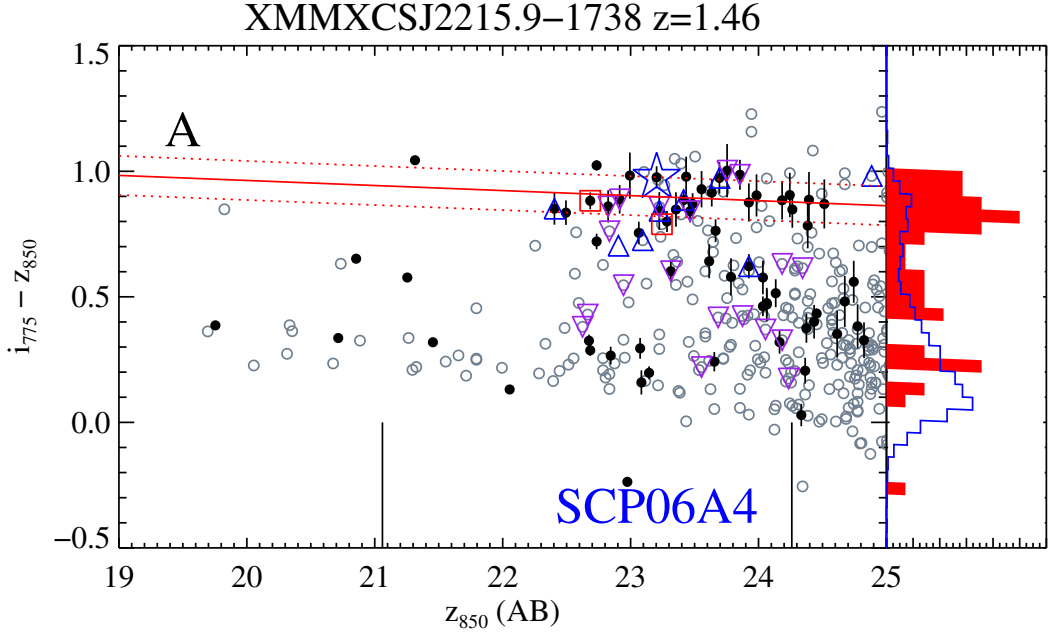


FIG. 15.— Cluster color-magnitude diagrams. Small circles indicate galaxies located within 0.65Mpc of the cluster center. Dark solid circles pass our broader quantitative morphology cuts, light open circles do not. The slightly larger squares and triangles indicate galaxies spectroscopically confirmed to be cluster members, including those that lie outside of the 0.65Mpc aperture. Red squares indicate spectroscopically confirmed members lacking significant [O II] emission ( $EW > -5\text{\AA}$ ). Blue upward pointing triangles indicate spectroscopically confirmed members with significant [O II] emission. Purple downward pointing triangles indicate spectroscopically confirmed members found in the literature but with unpublished [O II] EWs. Stars indicate SN hosts. Blue stars are foreground SN hosts, gold stars are cluster members SN hosts, and red stars are background SN hosts. The solid red line is the best-fit linear color-magnitude relation, and the dashed lines indicate the measured scatter (including contributions from both measurement uncertainties and the intrinsic scatter). The red histogram indicates CMR residuals of cluster galaxies passing our broader morphology cuts falling in the magnitude range  $M^* - 2.2 < z_{850} < M^* + 1.0$ , which is indicated by the long tick marks on the x-axis. The blue histogram is the solid-angle-scaled analog for the GOODS control fields.

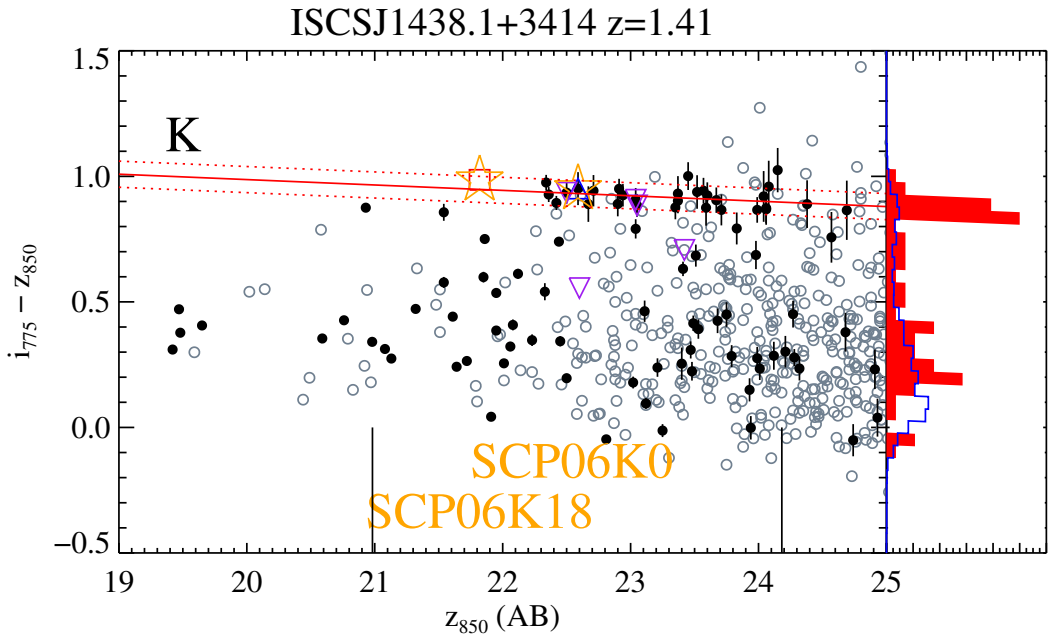


FIG. 15.— Color magnitude diagrams (continued).

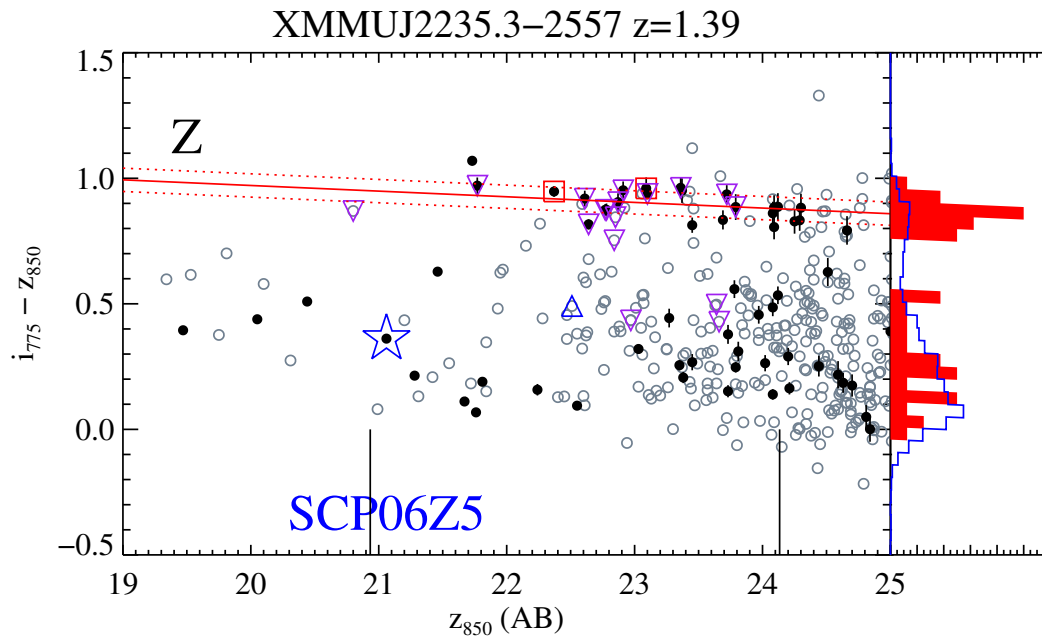


FIG. 15.— Color magnitude diagrams (continued).

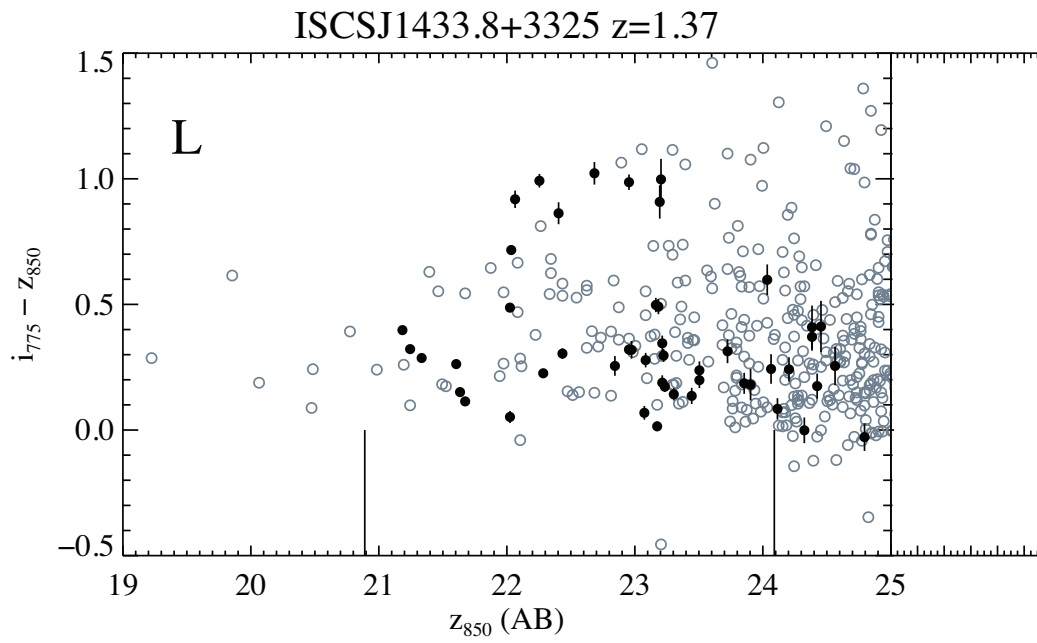


FIG. 15.— Color magnitude diagrams (continued).

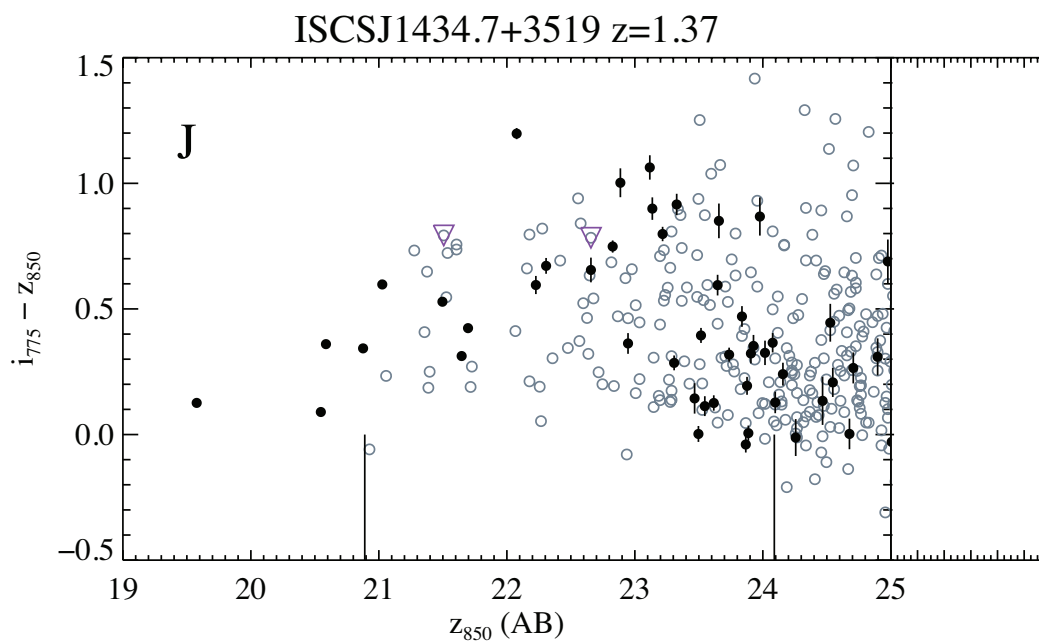


FIG. 15.— Color magnitude diagrams (continued).

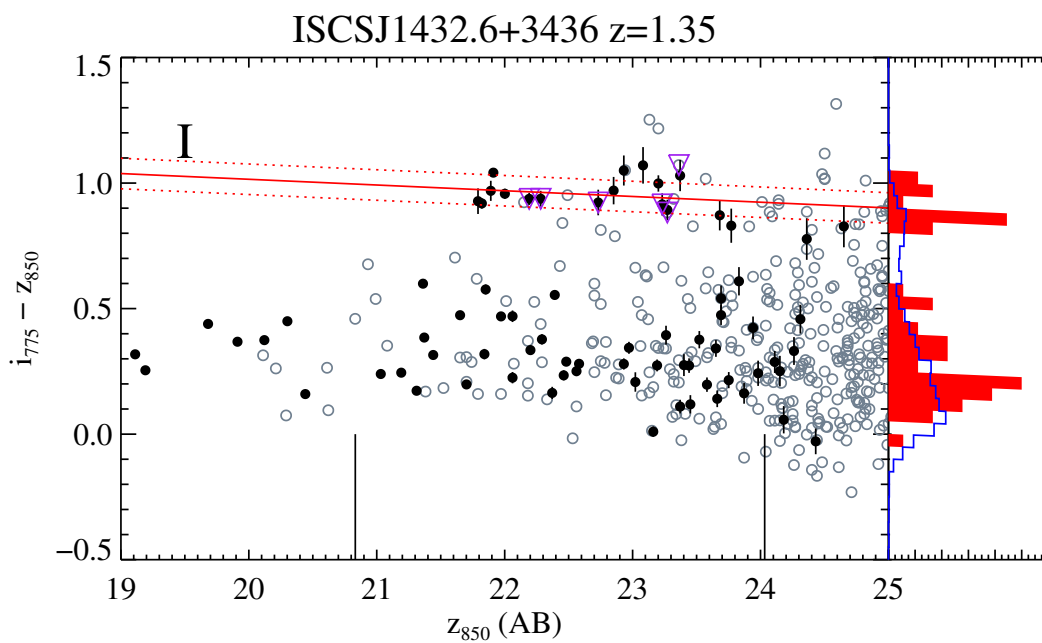


FIG. 15.— Color magnitude diagrams (continued).

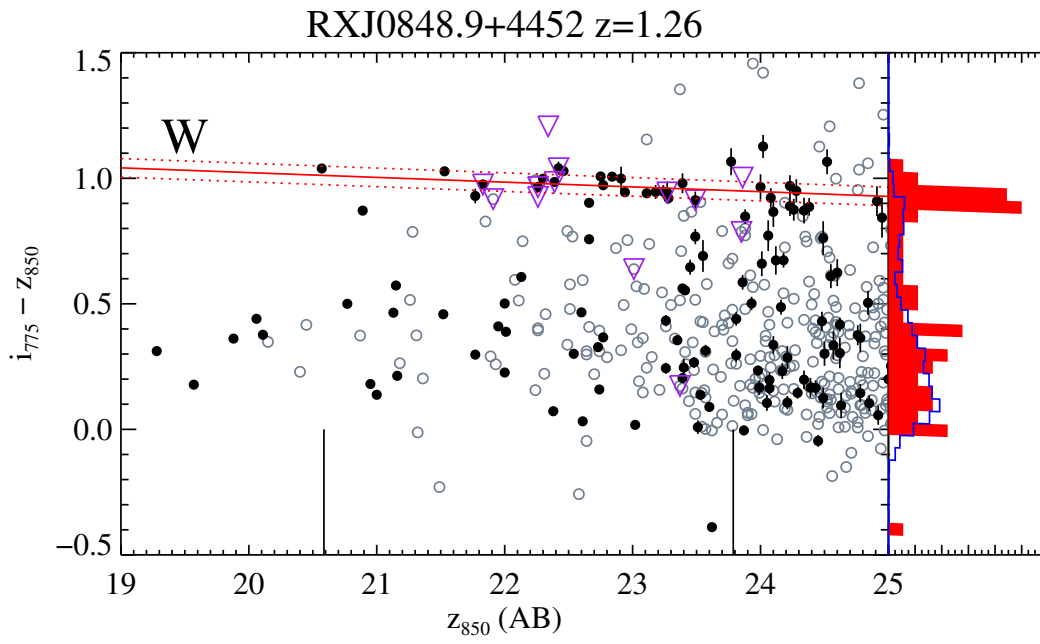


FIG. 15.— Color magnitude diagrams (continued).

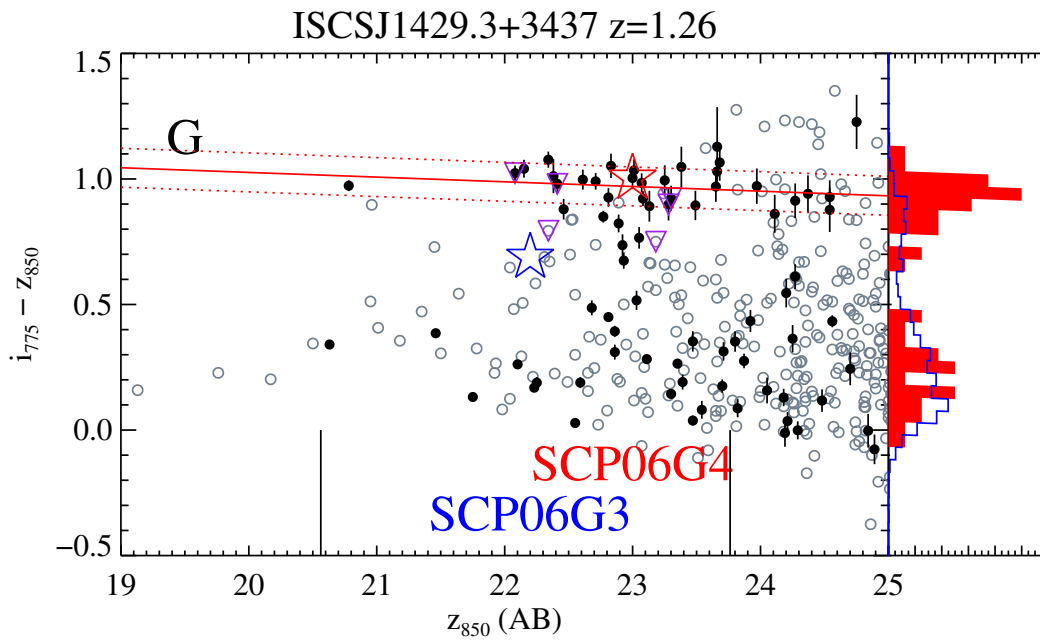


FIG. 15.— Color magnitude diagrams (continued).

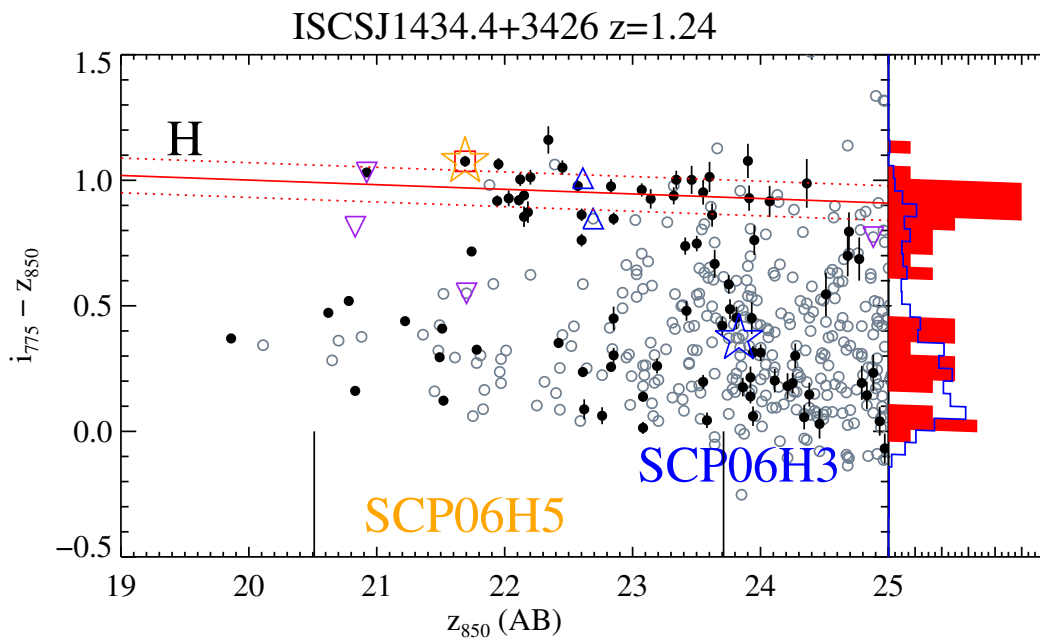


FIG. 15.— Color magnitude diagrams (continued).

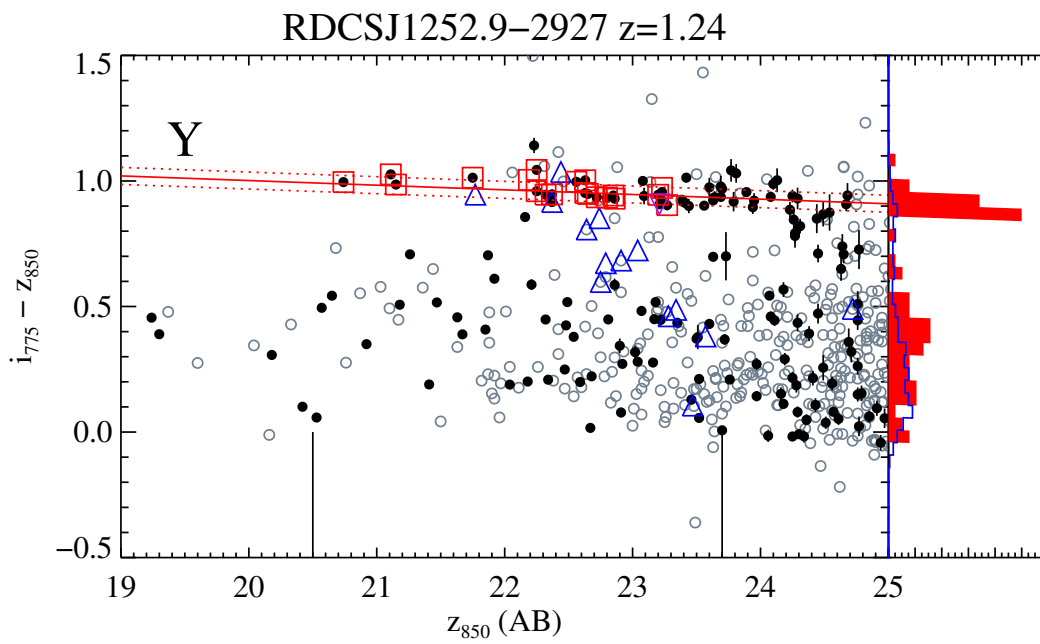


FIG. 15.— Color magnitude diagrams (continued).

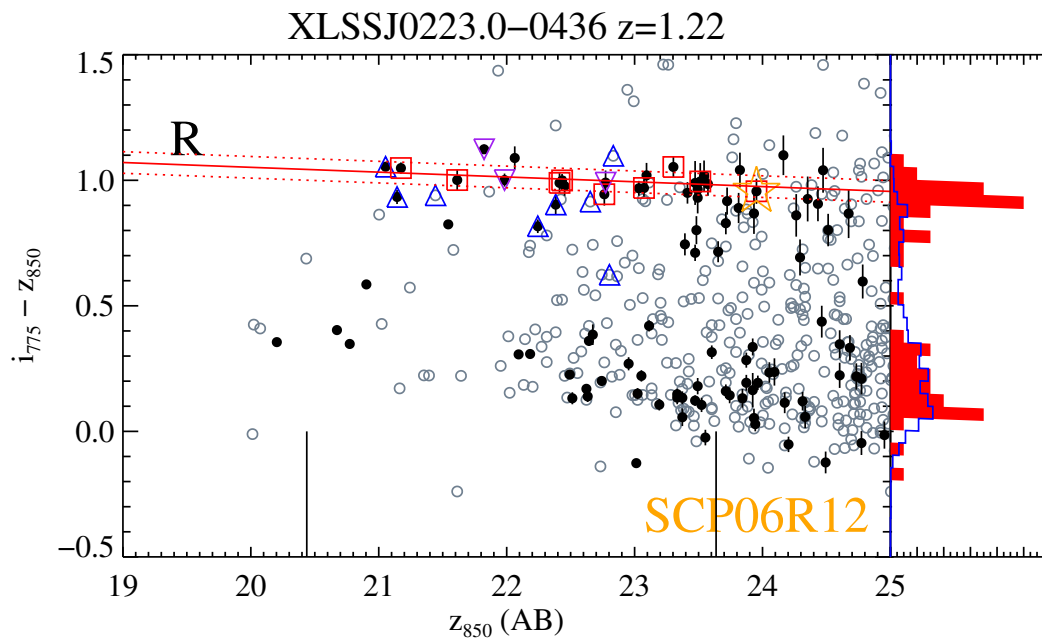


FIG. 15.— Color magnitude diagrams (continued).

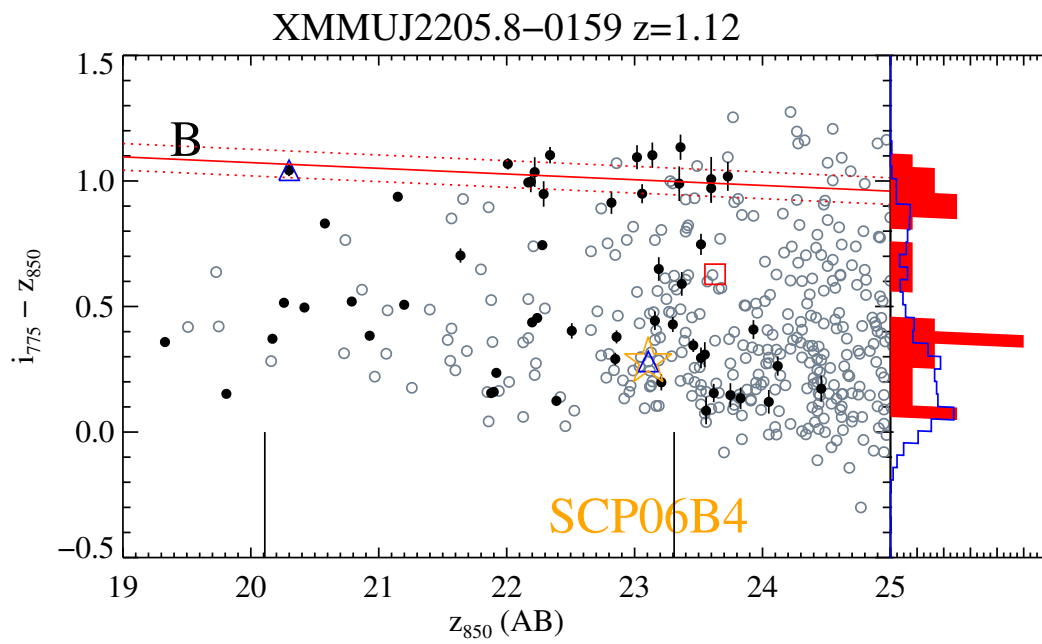


FIG. 15.— Color magnitude diagrams (continued).

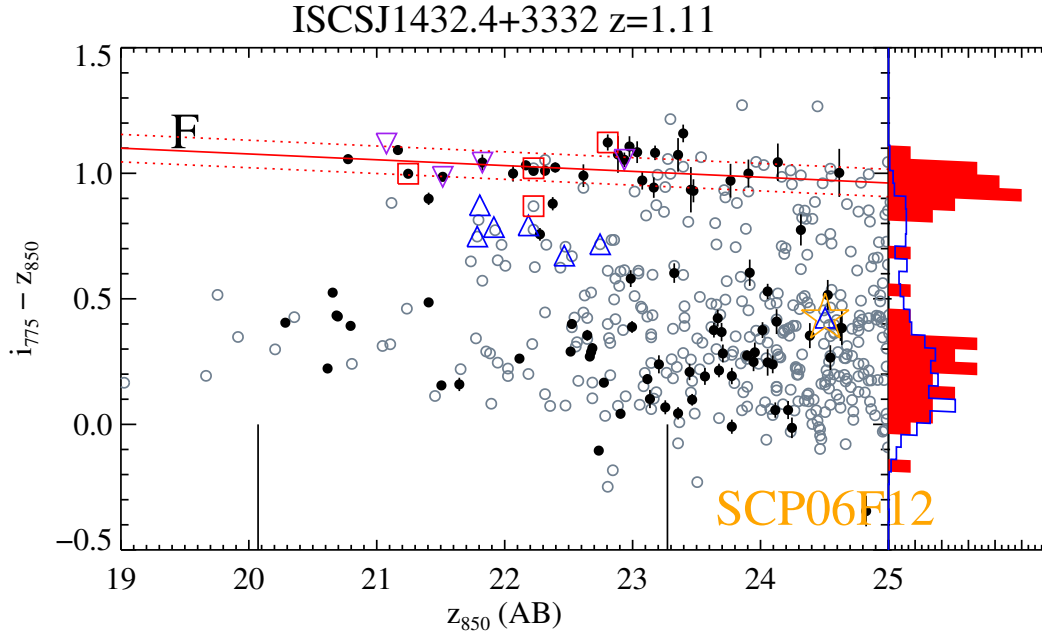


FIG. 15.— Color magnitude diagrams (continued).

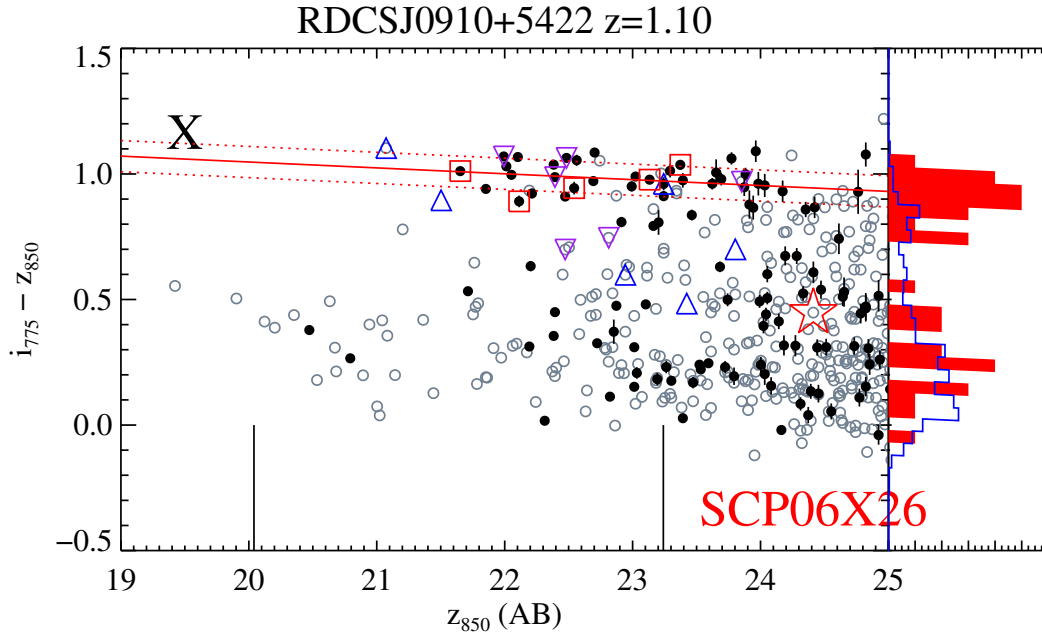


FIG. 15.— Color magnitude diagrams (continued).

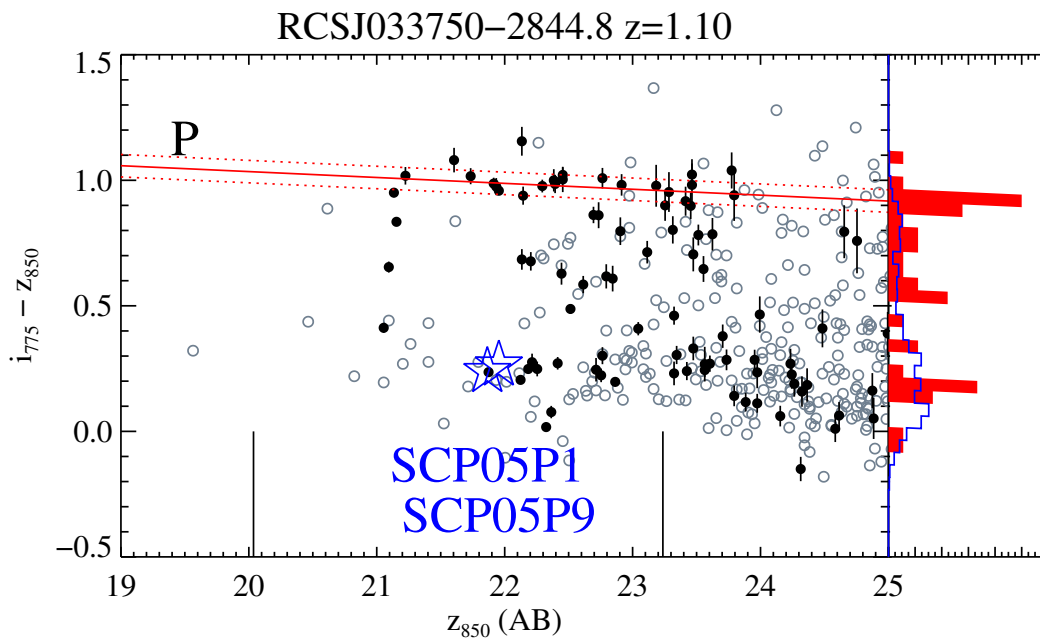


FIG. 15.— Color magnitude diagrams (continued).

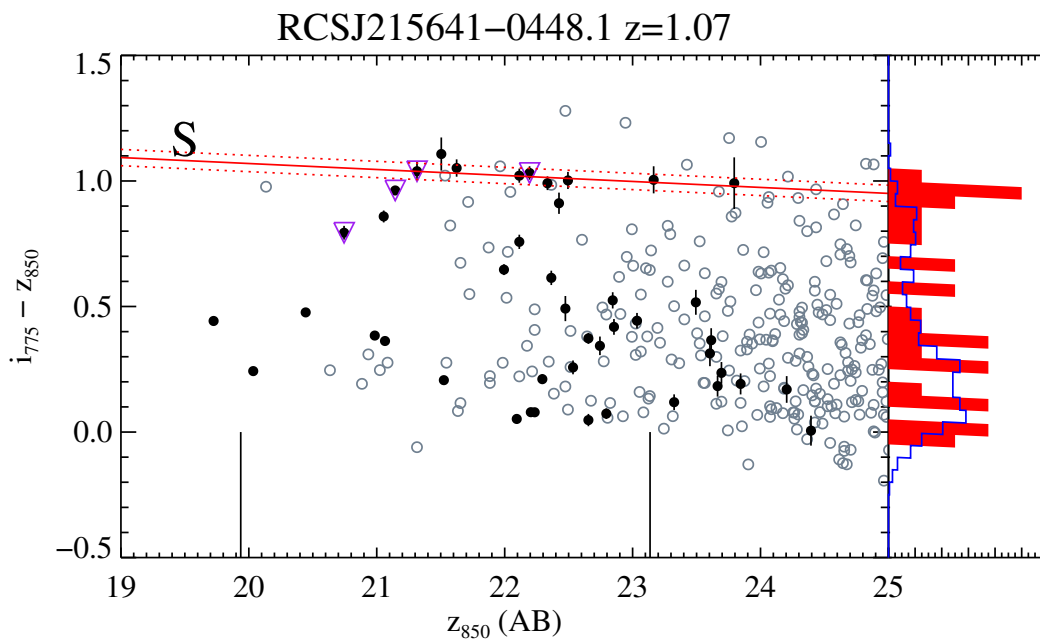


FIG. 15.— Color magnitude diagrams (continued).



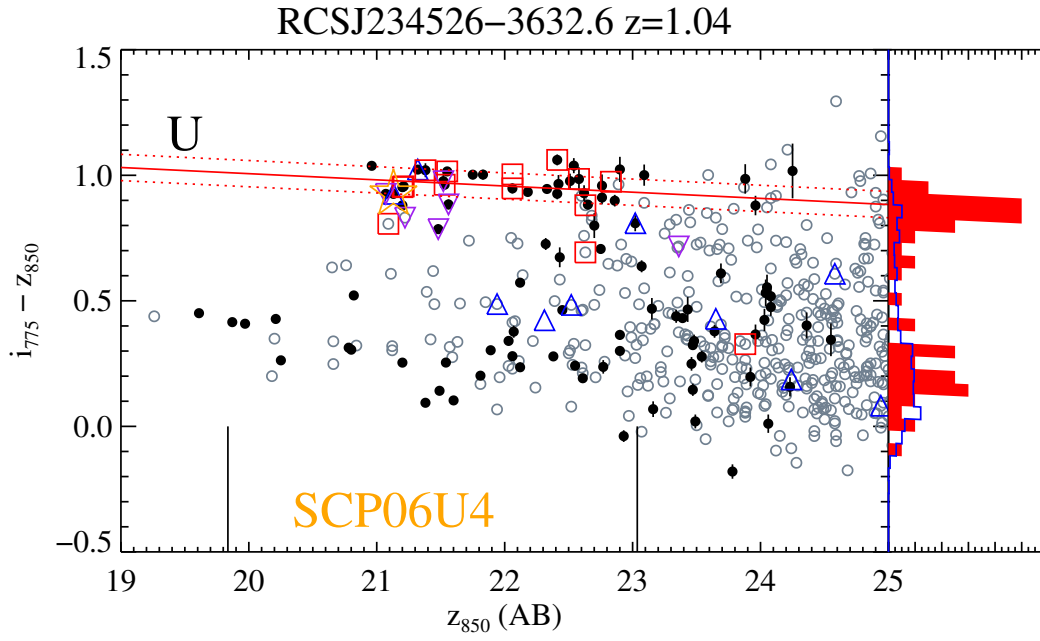


FIG. 15.— Color magnitude diagrams (continued).

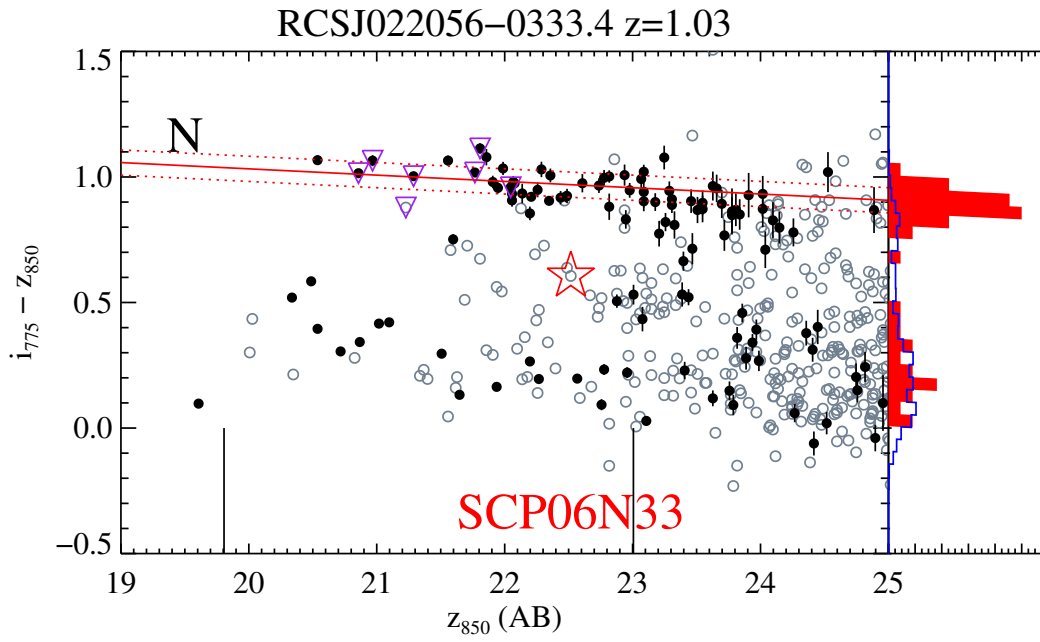


FIG. 15.— Color magnitude diagrams (continued).

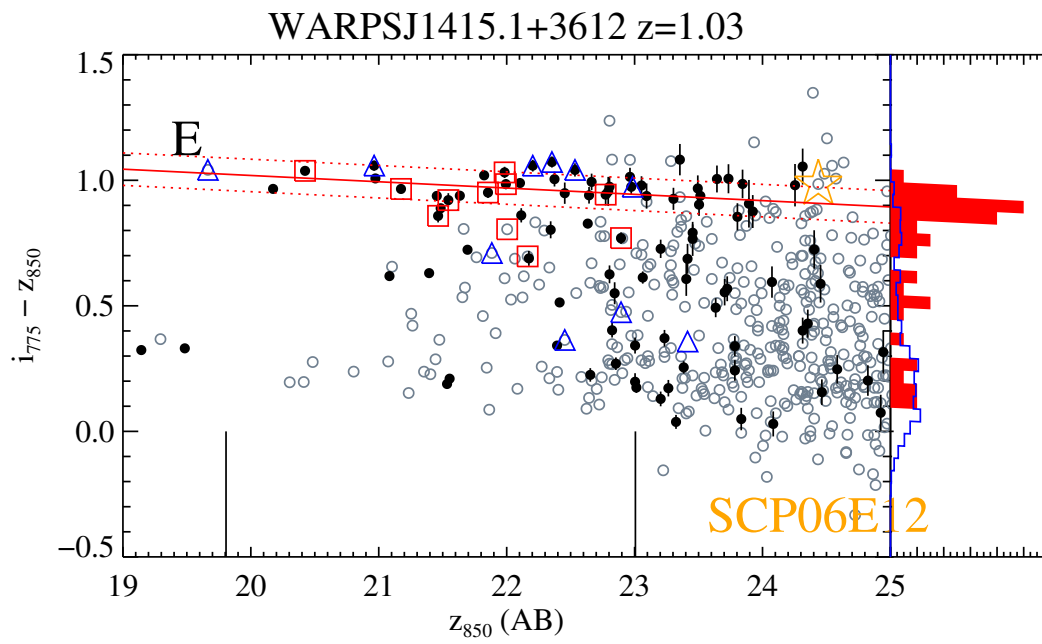


FIG. 15.— Color magnitude diagrams (continued).

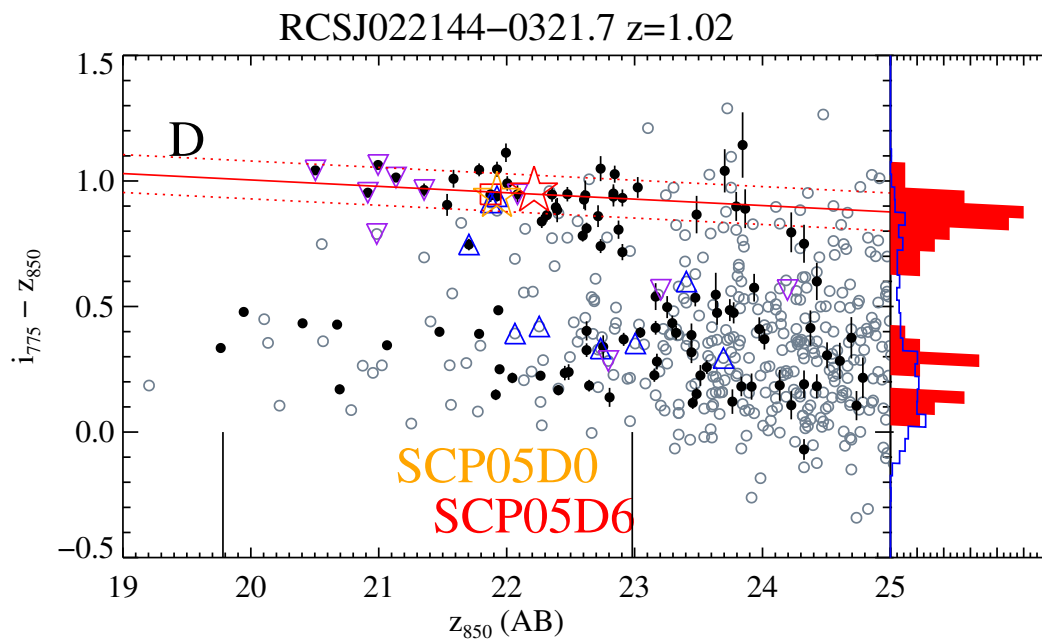


FIG. 15.— Color magnitude diagrams (continued).

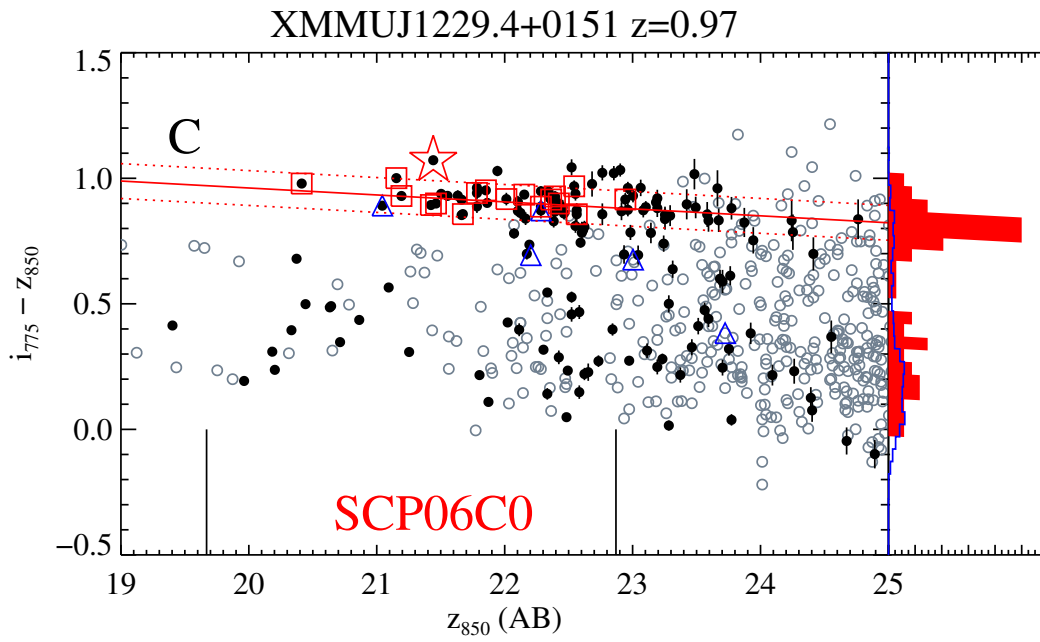


FIG. 15.— Color magnitude diagrams (continued).

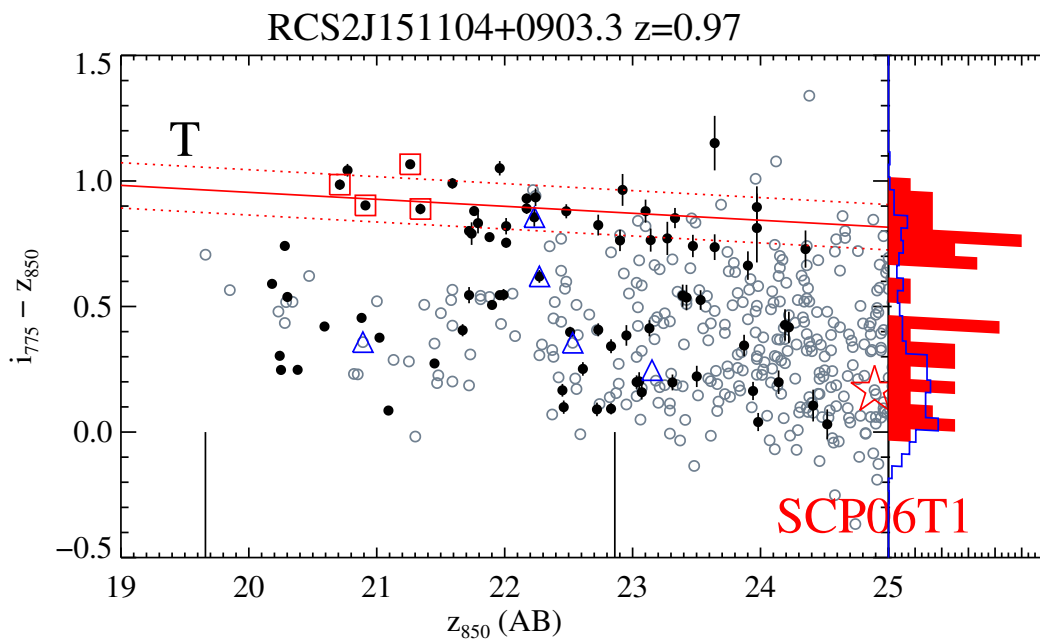


FIG. 15.— Color magnitude diagrams (continued).

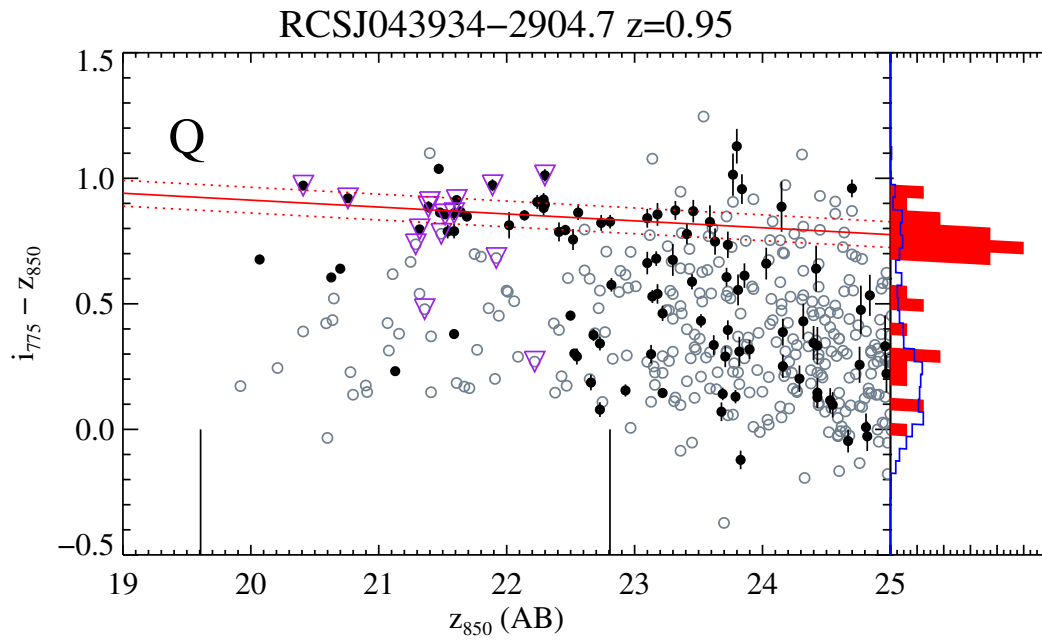


FIG. 15.— Color magnitude diagrams (continued).

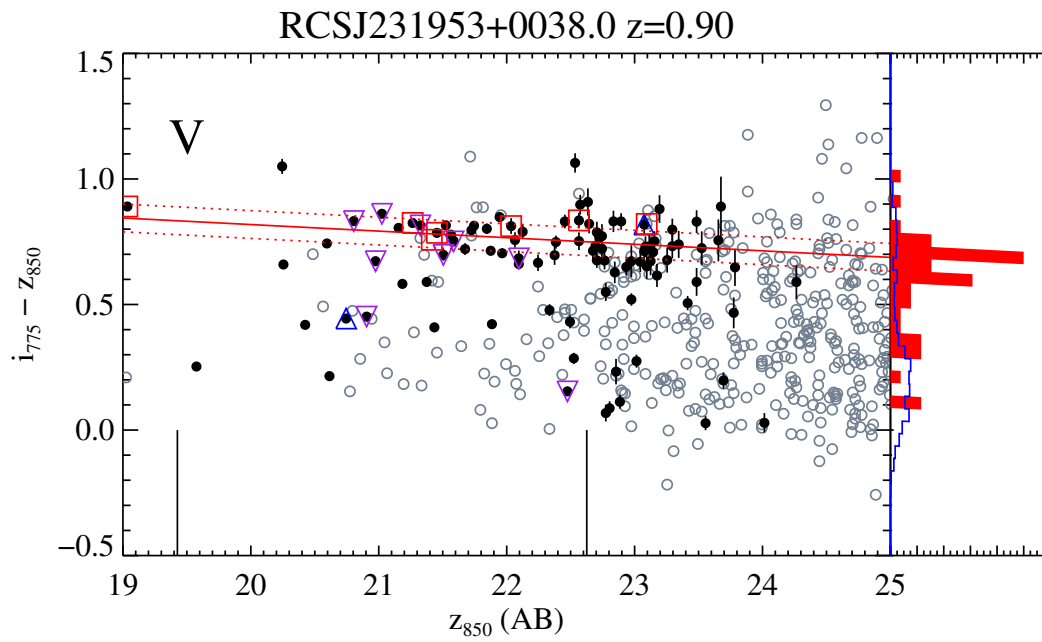


FIG. 15.— Color magnitude diagrams (continued).

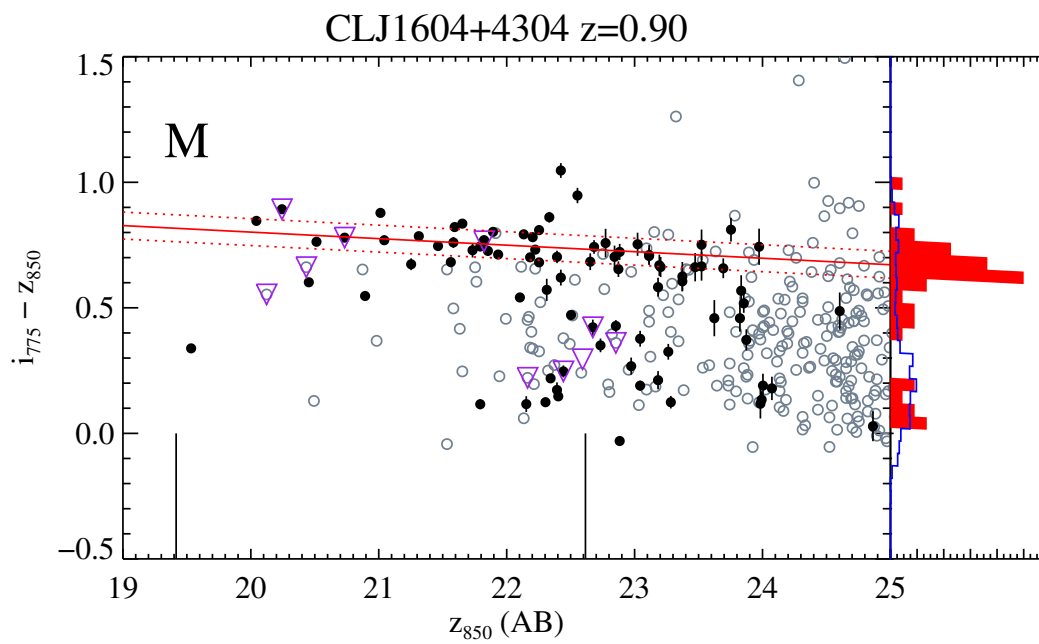


FIG. 15.— Color magnitude diagrams (continued).